

DAR TABLE OF CONTENTS

VOLUME 1 - NON-PROPRIETARY

Chapter 1 GENERAL INFORMATION

- 1.1 Purpose and Organization of Report
- 1.2 History of Problem
- 1.3 SSES Containment Program
- 1.4 Plant Description

Chapter 2 SUMMARY

- 2.1 Load Definition Summary
- 2.2 Design Assessment Summary

Chapter 3 SRV DISCHARGE AND LOCA TRANSIENT DESCRIPTION

- 3.1 Description of Safety Relief Valve (SRV) Discharge
- 3.2 Description of Loss-of-Coolant Accident (LOCA)

Chapter 4 LOAD DEFINITION

- 4.1 Safety Relief Valve (SRV) Discharge Load Definition
- 4.2 Loss-of-Coolant Accident (LOCA) Load Definition
- 4.3 Annulus Pressurization

Chapter 5 LOAD COMBINATIONS FOR STRUCTURES, PIPING, AND EQUIPMENT

- 5.1 Concrete Containment and Reactor Building Load Combinations
- 5.2 Structural Steel Load Combinations
- 5.3 Liner Plate Load Combinations
- 5.4 Downcomer Load Combinations
- 5.5 Piping, Quencher, and Quencher Support Load Combinations
- 5.6 NSSS Load Combinations
- 5.7 Balance of Plant (BOP) Equipment Load Combinations
- 5.8 Electrical Raceway System Load Combinations
- 5.9 HVAC Duct System Load Combinations

Chapter 6 DESIGN CAPABILITY ASSESSMENT

- 6.1 Concrete Containment and Reactor Building Capability Assessment Criteria
- 6.2 Structural Steel Capability Assessment Criteria
- 6.3 Liner Plate Capability Assessment Criteria

Docket # 50-387  
Control # 8507190306  
Date 7/21/85 of Document  
REGULATORY DOCKET FILE

TABLE OF CONTENTS (Continued)

- 6.4 Downcomer Capability Assessment Criteria
- 6.5 Piping, Quencher, and Quencher Support Capability Assessment Criteria
- 6.6 NSSS Capability Assessment Criteria
- 6.7 BOP Equipment Capability Assessment Criteria
- 6.8 Electrical Raceway System Capability Assessment Criteria
- 6.9 HVAC Duct System Capability Assessment Criteria

Chapter 7      DESIGN ASSESSMENT

- 7.1 Assessment Methodology
- 7.2 Design Capability Margins

Chapter 8      SSES QUENCHER VERIFICATION TEST (PROPRIETARY)

- 8.1 Introduction
- 8.2 Test Facility and Instrumentation
- 8.3 Test Parameters and Matrix
- 8.4 Test Results
- 8.5 Data Analysis and Verification of Load Specification

Chapter 9      GKM IIM STEAM BLOWDOWN TESTS

- 9.1 Introduction
- 9.2 Test Facility and Instrumentation
- 9.3 Test Parameters and Matrix
- 9.4 Test Results
- 9.5 Data Analysis and Load Specification
- 9.6 Verification of the Design Specification

Chapter 10     RESPONSES TO NRC QUESTIONS

- 10.1      NRC Questions
- 10.2      Responses

Chapter 11     REFERENCES

VOLUME 2 - NON-PROPRIETARY

Appendix A     CONTAINMENT DESIGN ASSESSMENT

- A.1 Containment Structural Design Assessment
- A.2 Submerged Structures Design Assessment

Appendix B     CONTAINMENT RESPONSE SPECTRA DUE TO SRV AND LOCA LOADS

- B.1 Containment Mode Shapes
- B.2 Containment Response Spectra

TABLE OF CONTENTS (Continued)

Appendix C REACTOR/CONTROL BUILDING RESPONSE SPECTRA  
DUE TO LOCA AND SRV LOADS

Appendix D PROGRAM VERIFICATION

D.1 Poolswell Model Verification  
D.2 Velpot Computer Code Description and Verification

Appendix E REACTOR AND CONTROL BUILDING DESIGN  
ASSESSMENT

Appendix F BOP AND NSSS PIPING DESIGN ASSESSMENT

Appendix G NSSS DESIGN ASSESSMENT (DELETED)

Appendix H EQUIPMENT DESIGN ASSESSMENT (DELETED)

Appendix I SUPPRESSION POOL TEMPERATURE RESPONSE TO SRV  
DISCHARGE

Appendix J VERIFICATION OF SRV SUBMERGED STRUCTURE  
DRAG LOAD (PROPRIETARY)

Appendix K DRYWELL FLOOR VACCUM BREAKER (VB) CYCLING DURING  
CHUGGING

Appendix L SUPPLEMENTAL DESIGN ASSESSMENT

L.1 Assessment Methodology  
L.2 Assessment Results

VOLUME 3 - PROPRIETARY

Chapter 4 PROPRIETARY LOAD DEFINITION

Chapter 8 PROPRIETARY SSES QUENCHER VERIFICATION TEST

Appendix D PROGRAM VERIFICATION

APPENDIX J VERIFICATION OF SRV SUBMERGED STRUCTURE LOAD

VOLUME 4 - PROPRIETARY

Chapter 9 SSES LOCA STEAM CONDENSATION VERIFICATION TEST

PROPRIETARY

- 9-171 Comparison of the Amplitudes of Pressure Time Histories No. 3 and 5 with the Mean Values During the Full MSL Test Nos. 3...10
- 9-172 Comparison of the Amplitudes of Pressure Time History No. 6 with the Mean Values During the 1/3 MSL Test Nos. 11 and 12
- 9-173 Comparison of the Amplitudes of Pressure Time History No. 9 with the Mean Values During the 1/6 MSL Test Nos. 13...20
- 9-174 Oscillatory Frequencies of Pressure Time Histories No. 3 and 5 and Pressure Events During Full MSL Test Nos. 3...10
- 9-175 Oscillatory Frequencies of Pressure Time History No. 6 and Pressure Events During 1/3 MSL Test No. 11
- 9-176 Oscillatory Frequencies of Pressure Time History No. 9 and Pressure Events During 1/6 MSL Test Nos. 13 and 19
- 9-177a Finally Selected CO Time Segment - Pressure Time History No. 14
- 9-177b Finally Selected CO Time Segment - Pressure Time History No. 14
- 9-177c PSD of the specified CO Time Segment
- 9-178 Oscillatory Frequencies of Pressure Time History No. 14 and Pressure Events During RCL Test Nos. 1 and 33
- 9-178a Comparison of the Envelope of the PSD's of the Selected PTH Nos. 3, 5, 6 and 9 and the Envelope of the Test/Repeat Mean PSD's
- 9-178b Normalized PSD of PTH No. 3
- 9-178c Normalized PSD of PTH No. 5
- 9-178d Normalized PSD of PTH No. 6
- 9-178e Normalized PSD of PTH No. 9
- 9-178f Envelope of Normalized PSD's of PTH Nos. 3, 5, 6 and 9
- 9-178g Mean Values of Pressure Events and Time Spans from which PSD's are produced - Full MSL Break
- 9-178h Mean Values of Pressure Events and Time Spans From Which PSD's are Produced - 1/3 MSL Break

PROPRIETARY

- 9-178i Mean PSD's of Test/Repeat Test No. 3/4 for Corresponding Time Segments
- 9-178j Mean PSD's of Test/Repeat Test No. 3/4 for Corresponding Time Segments
- 9-178k Mean PSD's of Test/Repeat Test No. 9/10 for Corresponding Time Segments
- 9-178m Mean PSD's of Test/Repeat Test No. 9/10 for Corresponding Time Segments
- 9-178n Mean PSD's of Test/Repeat Test No. 11/12 for Corresponding Time Segments
- 9-178p Mean PSD's of Test/Repeat Test No. 11/12 for Corresponding Time Segments
- 9-178q Mean PSD's of Test/Repeat Test No. 11/12 for Corresponding Time Segments
- 9-178r Envelope of the Mean PSD's of the Time Segments from Test Nos. 3/4, 9/10, 11/12, 13/14 and 19/20
- 9-179 Pressure Amplitudes Normalized to the Sliding Mean Values - Bandpass 0.5-13 Hz - Test No. 5
- 9-180 Pressure Amplitudes Normalized to the Sliding Mean Values - Bandpass 0.5-13 Hz - Test No. 15
- 9-181 Probability Densities of the Normalized Pressure Amplitudes with Mean Values > 0.5 bar - Full MSL Tests
- 9-182 Probability Densities of the Normalized Pressure Amplitudes with Mean Values > 0.5 Bar - 1/3 MSL Tests
- 9-183 Probability Densities of the Normalized Pressure Amplitudes with Mean Values > 0.5 Bar - 1/6 MSL Tests
- 9-184 Derivation of the Maximum Overturning Moment
- 9-185 Multi-Single-Cell Model of the SSES Pool
- 9-186 Spatial Pressure Profile in the Circumferential Direction
- 9-187 Results of the Monte Carlo Calculations
- 9-188 Load Exceedance Criteria for Bandpass 0.5 - 13 Hz and Zero Phase
- 9-189 Load Exceedance Criteria for Bandpass 10-100 Hz and Zero Phase

PROPRIETARY

- 9-190 Effect of Desynchronized Time Window on Bottom Pressure Amplitude - Harmonic Time Histories with Identical Amplitudes in All Cells
- 9-191 Load Exceedance Criteria for Bandpass 0.5-13 Hz and Desynchronized Time Window
- 9-192 Load Exceedance Criteria for Bandpass 10 - 100 Hz and Desynchronized Time Window
- 9-193 KWU Source 303 Time History
- 9-194 KWU Source 305 Time History
- 9-195 KWU Source 306 Time History
- 9-196 KWU Source 309 Time History
- 9-197 KWU Source 314 Time History
- 9-198 Comparison of PTH No. 3 (P 6.8) and the Pressure Output From IWECS
- 9-199 Comparison of the PSD of PTH No. 3 (P 6.8) and the PSD of the Pressure From IWECS
- 9-200 Comparison of PTH No. 5 (P 6.8) and the Pressure Output From IWECS
- 9-201 Comparison of the PSD of PTH No. 5 (P 6.8) and the PSD of the Pressure Output from IWECS
- 9-202 Comparison of PTH No. 6 (P 6.8) and the Pressure Output From IWECS
- 9-203 Comparison of the PSD of PTH No. 6 (P 6.8) and the PSD of the Pressure Output From IWECS
- 9-204 Comparison of PTH No. 9 (P 6.8) and the Pressure Output From IWECS
- 9-205 Comparison of the PSD of PTH No. 9 (P 6.8) and the PSD of the Pressure Output From IWECS
- 9-206 Comparison of PTH No. 14 (P 6.8) and the Pressure Output From IWECS
- 9-207 Comparison of the PSD of PTH No. 14 (P 6.8) and the PSD of the Pressure Output From IWECS
- 9-208 IWECS/MARS Coordinate System
- 9-209 Comparison of Horizontal Acceleration Response Spectra thru  
9-218 Due to LOCA (DFFR) vs. LOCA (KWU)

PROPRIETARY

- 9-219 Comparison of Vertical Acceleration Response Spectra  
thru Due to LOCA (DFFR) vs. LOCA (KWU)  
9-227
- 9-228 Comparison of Horizontal Acceleration Response Spectra  
thru for the combination SSE + SRV + LOCA (DFFR) vs.  
9-237 SSE + SRV + LOCA (KWU)
- 9-238 Comparison of Vertical Acceleration Response Spectra  
thru for the Combination SSE + SRV + LOCA (DFFR) vs.  
9-246 SSE + SRV + LOCA (KWU)
- 9-247 Schematic View of Finite Element Model
- 9-248 Schematic View of Structural Model
- 9-249 Schematic View of Fluid Elements
- 9-250 Amplitudes of the Resultant Force at the Bracing  
- Frequency Range: 0.5...200Hz - Test No. 3 & 4
- 9-251 Amplitudes of the Resultant Force at the Bracing  
- Frequency Range: 0.5...200Hz - Test No. 5 & 6
- 9-252 Amplitudes of the Resultant Force at the Bracing  
- Frequency Range: 0.5...200Hz - Test No. 7 & 8
- 9-253 Amplitudes of the Resultant Force at the Bracing  
- Frequency Range: 0.5...200 HZ - Test No. 9 & 10
- 9-254 Amplitudes of the Resultant Force at the Bracing  
- Frequency Range: 0.5...200Hz - Test No. 11 & 12
- 9-255 Amplitudes of the Resultant Force at the Bracing  
- Frequency Range: 0.5...200Hz - Test No. 13 & 14
- 9-256 Amplitudes of the Resultant Force at the Bracing  
- Frequency Range: 0.5...200Hz - Test No. 15 & 16
- 9-257 Amplitudes of the Resultant Force at the Bracing  
- Frequency Range: 0.5...200Hz - Test No. 17 & 18
- 9-258 Amplitudes of the Resultant Force at the Bracing  
- Frequency Range: 0.5...200Hz - Test No. 19 & 20
- 9-259 Frequency Distribution of the Resultant Bracing Forces  
- Test No. 3..10
- 9-260 Frequency Distribution of the Resultant Bracing Forces  
- Test No. 11 & 12
- 9-261 Frequency Distribution of the Resultant Bracing Forces  
- Test No. 13...18

PROPRIETARY

SECTIONS 9.4, 9.5 AND 9.6  
GKM-II-M STEAM BLOWDOWN TEST

TABLE OF CONTENTS

9.4 TEST RESULTS

9.4.1	Description of Break Transient
9.4.1.1	MSL Break - Steam Mass Flow Transient
9.4.1.1.1	RCL Break - Steam Mass Flow Transient
9.4.1.2	MSL Break - Air Content Transient
9.4.1.2.1	RCL Break - Air Content Transient
9.4.1.3	MSL Break - Drywell and Suppression Chamber Pressure Transient
9.4.1.3.1	RCL Break - Drywell and Suppression Chamber Pressure Transient
9.4.1.4	MSL Break - Temperature Variations in the Suppression Pool
9.4.1.4.1	RCL Break - Temperature Variations in the Suppression Pool
9.4.2	Dynamic Pressure Loads at the Pool Boundary
9.4.2.1	General Observations
9.4.2.1.1	Frequency (of Oscillations) Analyses
9.4.2.1.1.1	Oscillation Frequencies
9.4.2.1.1.2	Event Frequencies
9.4.2.1.2.	Statistical Evaluation
9.4.2.1.2.1	Amplitude Components of the Low-Frequency and High-Frequency Bands
9.4.2.1.2.2	Frequency (of Occurrence) Distributions
9.4.2.1.2.3	Statistical Characteristics
9.4.2.1.3	Parameter Influences
9.4.2.1.3.1	Influence of the Break Cross-Sectional Area
9.4.2.1.3.2	Influence of the Initial Pool Temperature
9.4.2.1.3.3	Influence of the Initial Air Content in the Drywell
9.4.2.1.4	Correlation of Film and Pressure Recordings
9.4.2.1.5	Repeat Tests and Reproducibility of the Results
9.4.3	Loads on the Vent-Pipe Bracing, Dummy Quencher and I-Beam
9.4.3.1	Statistical Evaluation
9.4.3.1.1	Frequency Distribution of the Resultant Vent-Pipe Bracing Forces
9.4.3.1.2	Distributions of Direction of the Resultant Vent-Pipe Bracing Forces
9.4.3.1.3	Frequency Distributions of the Resultant Bending Moments at the Dummy Quencher
9.4.3.1.4	Direction Distribution of the Resultant Bending Moments at the Dummy Quencher
9.4.3.1.5	Frequency Distributions of the Forces on the I-Beam
9.4.3.1.6	Statistical Characteristics
9.4.3.2	Parameter Influences

PROPRIETARY

9.4.3.2.1	Influence of the Break Cross-Sectional Area
9.4.3.2.2	Influence of the Initial Pool Temperature
9.4.3.2.3	Influence of the Initial Air Content in the Drywell
9.4.3.3	Frequency (of Oscillation) Analyses
9.4.4	Summary
9.5	Data Analysis and Load Specification
9.5.1	Introduction
9.5.2	Data Analysis
9.5.2.1	Dynamic Pressures in the Pool and Their Physical Interpretation
9.5.2.2	Evaluation of the Chugging Frequency at GKM II-M
9.5.2.3	Evaluation of the Pressure Oscillation Frequencies in the Pool
9.5.3	SSES LOCA Load Definition
9.5.3.1	Selection of the GKM II-M Time Segments to Be Sourced
9.5.3.1.1	Description of the Evaluation Procedure
9.5.3.1.2	Selection of the Chugging Pressure Time Histories
9.5.3.1.2.1	Selection of the CO Pressure Time History
9.5.3.1.3	Verification of the Selected Time Segments
9.5.3.1.3.1	Chugging Pressure Time Histories
9.5.3.1.3.2	CO Pressure Time History
9.5.3.1.3.2.1	CO Evaluation
9.5.3.1.3.2.1.1	Comparison of the CO Amplitudes at GKM-M
9.5.3.1.3.2.1.2	PSD Comparison
9.5.3.2	Determination of the Amplitude Factors
9.5.3.2.1	Generation of the GKM II-M Probability Density Distributions
9.5.3.2.2	Calculation of the Symmetric and Asymmetric Amplitude Factors
9.5.3.3	Determination of the SSES-Unique Chugging/CO Sources
9.5.3.4	Application Procedure for Calculating the Susquehanna SES Boundary Loads
9.5.3.4.1	Symmetric Load Case
9.5.3.4.2	Asymmetric Load Case
9.5.3.5	Verification of the SSES LOCA Load Definition
9.5.3.5.1	JAERI Comparison
9.5.3.5.1.1	Introduction
9.5.3.5.1.2	Description of Comparison Method
9.5.3.5.1.2.1	The JAERI Test Data
9.5.3.5.1.2.2	Chug Sources
9.5.3.5.1.2.3	The JAERI Acoustic Model
9.5.3.5.1.2.4	Comparison Basis
9.5.3.5.1.3	Results and Discussion
9.5.3.5.2	Verification of the 50 msec Time Window
9.5.3.5.3	Response to the NRC Concerns Regarding the SSES Chugging Load Specification
9.5.3.5.3.1	Contribution of the Asymmetric Chugging Load Specification to the Plant Structural Response
9.5.3.5.3.1.1	Comments on the Asymmetric Chugging Load Case
9.5.3.5.3.1.2	Generic and SSES Position WNP-2 Submittal
9.5.3.5.3.2	Comparison of Minimum Variance Trials Using the SSES/GKM II-M Sources with the JAERI Data

PROPRIETARY

- 9.5.3.5.3.2.2 Comparison Procedure
- 9.5.3.5.3.2.3 Results and Discussion
- 9.5.3.5.3.2.3.1 PSD Comparison
- 9.5.3.5.3.2.3.2 Pressure Response Spectra (PRS) Comparison
- 9.6 Verification of the Design Specification
- 9.6.1 Evaluation of the DFFR CO and Chugging Load Specification
- 9.6.1.1 Containment Acceleration Response Spectra Comparison
- 9.6.1.1.1 LOCA (DFFR) vs. LOCA (KWU) Acceleration Response Spectra Comparison
- 9.6.1.1.2 SSE + SRV (ADS) + LOCA (DFFR) vs. SSE + SRV (ADS) + LOCA (KWU) Acceleration Response Spectra comparison
- 9.6.1.2 Evaluation of the Containment Response Spectra Comparison
- 9.6.1.2.1 Load Reduction Assessment
- 9.6.1.2.1.1 Reduction of Load Amplitude Factor
- 9.6.1.2.1.2 Re-Selection of Pressure Time Histories
- 9.6.1.2.1.3 Adoption of Mark II Owner's Group Load Methodology
- 9.6.1.2.1.4 Development of a New Chugging Load Methodology
- 9.6.1.2.2 Plant Reassessment
- 9.6.1.3 Summary
- 9.6.2 Verification of the Mark II Single Vent Dynamic Lateral Load Specification
- 9.6.2.1 Theoretical Determination of the Bracing Force at GKM II-M
- 9.6.2.1.1 Finite Element Model
- 9.6.2.1.2 Model Assumptions
- 9.6.2.1.3 Fluid Representation
- 9.6.2.1.4 Structural Model
- 9.6.2.1.5 Loading
- 9.6.2.1.6 Analysis Results
- 9.6.2.2 Bracing Force Data at GKM II-M
- 9.6.2.2.1 Measurement of the Bracing Forces
- 9.6.2.2.2 Resultant Bracing Forces
- 9.6.2.3 Comparison of the Theoretical and Measured Maximum Resultant Bracing Force
- 9.6.3 Statistical Evaluation of the GKM II-M Resultant Bracing Force Data
- 9.6.3.1 Introduction
- 9.6.3.2 Derivation of a Probability Density Function from the measured Resultant Bracing Forces from the 1/6 MSL Tests
- 9.6.3.2.1 General Considerations
- 9.6.3.2.2 Application to the 1/6 MSL Tests
- 9.6.3.3 Determination of the Extrapolated Mark II Impulse

PROPRIETARY

SECTIONS 9.4, 9.5 AND 9.6

FIGURES

<u>Number</u>	<u>Title</u>
9-15	Steam Mass Flux vs. Time - 1/6, 1/3 and Full MSL Breaks - Test No. 5, 11, and 15
9-15a	Comparison of the Measured Steam Mass Flux with the Theoretically Calculated Transient - Full MSL Break
9-16	Steam Mass Flux vs. Time - RCL Break - Test No. 1 and 2
9-16a	Comparison of the Measured Steam Mass Flux with the Theoretically Calculated Transient - RCL Break
9-17	Steam Air Content vs. Time - Full, 1/3 and 1/6 MSL Breaks - Test No. 5, 11 and 15
9-18	Steam Air Content vs. Time - 85% and 100% Initial Drywell Air Volume - Test No. 5, 7 and 8
9-19	Steam Air Content vs. Time - RCL Break - Test No. 1 and 2
9-19a	Steam Air Content vs. Steam Mass Flux for Various Break Sizes
9-20	Drywell and Wetwell Pressure Transients - Full MSL Break - Test No. 5
9-20a	Drywell and Wetwell Pressure Transients - 1/3 MSL Break - Test No. 11
9-20b	Drywell and Wetwell Pressure Transients - 1/6 MSL Break - Test No. 15
9-21	Drywell and Wetwell Pressure Transients - Full, 1/3 and 1/6 MSL Breaks - Test No. 5, 7 and 8
9-22	Drywell and Wetwell Pressure Transients - RCL Break - Test No. 1
9-22a	Drywell and Wetwell Pressure Transients - RCL Break - Test No. 2
9-23	Pool Temperature Variations vs. Time - Full, 1/3 and 1/6 MSL Breaks - Test No. 5, 11 and 15
9-24	Pool Temperature Variations - Full MSL Break - Test No. 3, 5 and 9

PROPRIETARY

- 9-25 Pool Temperature Variations - 1/6 MSL Break - Test No. 14, 15 and 20
- 9-26 Pool Temperature Variations - RCL Break - Test No. 1 and 2
- 9-27 Pool Temperature Variations - RCL Break - Test No. 1 and 33
- 9-27a Pool Temperature vs. Steam Mass Flux for Various Break Sizes - Transducer T 6.3
- 9-28 Compressed Pressure Time Histories - Full MSL Break - Test No. 3
- 9-29 Compressed Pressure Time Histories - Full MSL Break - Test No. 5
- 9-30 Compressed Pressure Time Histories - Full MSL Break - Test No. 9
- 9-31 Compressed Pressure Time Histories - 1/3 MSL Break - Test No. 11
- 9-32 Compressed Pressure Time Histories - 1/3 MSL Break - Test No. 14
- 9-33 Compressed Pressure Time Histories - 1/6 MSL Break - Test No. 15
- 9-34 Compressed Pressure Time Histories - 1/6 MSL Break - Test No. 20
- 9-35 Compressed Pressure Time Histories - RCL Break - Test No. 1
- 9-36 Compressed Pressure Time Histories - RCL Break - Test No. 33
- 9-36a Identification Sheet For Figures 9-37 thru 9-54
- 9-37 Visicorder No. I Traces - Test No. 3
- 9-38 Visicorder No. I Traces - Test No. 3
- 9-39 Visicorder No. I Traces - Test No. 5
- 9-40 Visicorder No. I Traces - Test No. 5
- 9-41 Visicorder No. I Traces - Test No. 9
- 9-42 Visicorder No. I Traces - Test No. 9
- 9-43 Visicorder No. I Traces - Test No. 11

PROPRIETARY

- 9-44 Visicorder No. I Traces - Test No. 11
- 9-45 Visicorder No. I Traces - Test No. 14
- 9-46 Visicorder No. I Traces - Test No. 14
- 9-47 Visicorder No. I Traces - Test No. 15
- 9-48 Visicorder No. I Traces - Test No. 15
- 9-49 Visicorder No. I Traces - Test No. 20
- 9-50 Visicorder No. I Traces - Test No. 20
- 9-51 Visicorder No. I Traces - Test No. 1
- 9-52 Visicorder No. I Traces - Test No. 1
- 9-53 Visicorder No. I Traces - Test No. 33
- 9-54 Visicorder No. I Traces - Test No. 33
- 9-55 Power Spectral Density (PSD) and Cross Power Spectral Density (CPSD) Equations
- 9-56 Power Spectral Densities - Sensor: P6.7 - Test No. 5, 11 and 15
- 9-57 Power Spectral Densities - Sensor: P6.7 - Test No. 3, 5 and 9
- 9-58 Power Spectral Densities - Sensor: P6.7 - Test No. 14, 15, and 20
- 9-59 Power Spectral Densities - Sensor: P6.7 - Test No. 1
- 9-60 Power Spectral Densities - Sensor P6.7 - Test No. 33
- 9-61 Compressed Time Histories - T5.6, LP5.1...LP5.5, P5.4 and P6.4 - Test No. 5
- 9-61a Identification Sheet For Figures 9-62 Thru 9-79
- 9-62 Visicorder No. III Traces - Test No. 3
- 9-63 Visicorder No. III Traces - Test No. 3
- 9-64 Visicorder No. III Traces - Test No. 5
- 9-65 Visicorder No. III Traces - Test No. 5
- 9-66 Visicorder No. III Traces - Test No. 9

PROPRIETARY

- 9-67 Visicorder No. III Traces - Test No. 9
- 9-68 Visicorder No. III Traces - Test No. 11
- 9-69 Visicorder No. III Traces - Test No. 11
- 9-70 Visicorder No. III Traces - Test No. 14
- 9-71 Visicorder No. III Traces - Test No. 14
- 9-72 Visicorder No. III Traces - Test No. 15
- 9-73 Visicorder No. III Traces - Test No. 15
- 9-74 Visicorder No. III Traces - Test No. 20
- 9-75 Visicorder No. III Traces - Test No. 20
- 9-76 Visicorder No. III Traces - Test No. 1
- 9-77 Visicorder No. III Traces - Test No. 1
- 9-78 Visicorder No. III Traces - Test No. 33
- 9-79 Visicorder No. III Traces - Test No. 33
- 9-80 Time between Chug Events - Mean Values vs. Break Size
- 9-81 Amplitudes and Mean Values of Pressure Events - Test No. 5 and 6
- 9-82 Amplitudes and Mean Values of Pressure Events - Test No. 11 and 12
- 9-83 Amplitudes and Mean Values of Pressure Events - Test No. 15 and 16
- 9-84 Amplitudes and Mean Values of Pressure Events - Test No. 1 and 2
- 9-85 Mean Values of Pressure Events - Test No. 3...10
- 9-86 Mean Values of Pressure Events - Test No. 11...20
- 9-87 Mean Values of Pressure Events - Test No. 1, 2, 33 and 34
- 9-88 Amplitudes and Mean Values of Pressure Events - Frequency Range: 10...100, 12...100 and 15...100 Hz - Test No. 13
- 9-89 This figure has been intentionally left blank

PROPRIETARY

- 9-90 This figure has been intentionally left blank
- 9-91 Positive Pressure Amplitude Histograms - Sensor: P6.4 - Frequency Range: 0.5...13 Hz - Full, 1/3, and 1/6 MSL Breaks
- 9-92 Negative Pressure Amplitude Histograms - Sensor: P6.4 - Frequency Range: 0.5...13 Hz - Full, 1/3, and 1/6 MSL Breaks
- 9-93 Positive Pressure Amplitude Histograms - Sensor: P6.7 - Frequency Range: 0.5...13 Hz - Full, 1/3 and 1/6 MSL Breaks
- 9-94 Negative Pressure Amplitude Histograms - Sensor: P6.7 - Frequency Range: 0.5...13 Hz - Full, 1/3 and 1/6 MSL Breaks
- 9-95 Positive Pressure Amplitude Histograms - Sensor: P6.8 - Frequency Range: 0.5...13 Hz - Full, 1/3, and 1/6 MSL Breaks
- 9-96 Negative Pressure Amplitude Histograms - Sensor: P6.8 - Frequency Range: 0.5...13 Hz - Full, 1/3 and 1/6 MSL Breaks
- 9-97 Positive and Negative Pressure Amplitude Histograms - Sensor: P6.4 - Frequency Range: 0.1...13 Hz - RCL Break
- 9-98 Positive and Negative Pressure Amplitude Histograms - Sensor: P6.7 - Frequency Range: 0.1...13 Hz - RCL Break
- 9-99 Positive and Negative Pressure Amplitude Histograms - Sensor: P6.8 - Frequency Range: 0.1...13 Hz - RCL Break
- 9-100 Positive Pressure Amplitudes vs. Break Size - Sensor: P6.7 - Frequency Range: 0.5...13 Hz - Full, 1/3 and 1/6 MSL Breaks
- 9-101 Negative Pressure Amplitudes vs. Break Size - Sensor: P6.7 - Frequency Range: 0.5...13 Hz - Full, 1/3 and 1/6 MSL Breaks
- 9-102 Positive Pressure Amplitudes vs. Initial Pool Temperature - Sensor: P6.7 - Frequency Range: 0.5...13 Hz - Full MSL Break
- 9-103 Negative Pressure Amplitudes vs. Initial Pool Temperature - Sensor: P6.7 - Frequency Range 0.5...13 Hz - Full MSL Break

PROPRIETARY

- 9-104 Positive Pressure Amplitudes vs. Initial Pool  
Temperature - Sensor: P6.7 - Frequency Range: 0.5...13  
Hz - 1/6 MSL Break
- 9-105 Negative Pressure Amplitudes vs. Initial Pool  
Temperature - Sensor: P6.7 - Frequency Range: 0.5...13  
Hz - 1/6 MSL Break
- 9-106 Positive Pressure Amplitudes vs. Initial Pool  
Temperature - Sensor: P6.7 - Frequency Range: 0.1...13  
Hz - RCL Break
- 9-107 Negative Pressure Amplitudes vs. Initial Pool.  
Temperature - Sensor: P6.7 - Frequency Range: 0.1...13  
Hz - RCL Break
- 9-108 Correlation of Pictures and Pressure Traces P6.4 and  
P6.7, 269 sec After Test Start - Test No. 15
- 9-109 Correlation of Pictures and Pressure Traces P6.4 and  
P6.7, 269 sec After Test Start - Test No. 15
- 9-110 Correlation of Pictures and Pressure Traces P6.4 and  
P6.7, 269 sec After Test Start - Test No. 15
- 9-111 Correlation of Pictures and Pressure Traces P6.4 and  
P6.7, 269 sec After Test Start - Test No. 15
- 9-112 Correlation of Pictures and Pressure Traces P6.4 and  
P6.7, 269 sec After Test Start - Test No. 15
- 9-113 Pictures of Vent Clearing Process - Test No. 3 and 18
- 9-114 Amplitudes of the Resultant Forces at the Bracing -  
Frequency Range: 0.5...200 Hz - Test No. 5 and 6
- 9-115 Amplitudes of the Resultant Forces at the Bracing -  
Frequency Range: 0.5...200 Hz - Test No. 11 and 12
- 9-116 Amplitudes of the Resultant Forces at the Bracing -  
Frequency Range: 0.5...200 Hz - Test No. 15 and 16
- 9-117 Amplitudes of the Resultant Forces at the Bracing -  
Frequency Range: 0.5...200 Hz - Test No. 1 and 2
- 9-118 Histogram of the Resultant Forces at the Bracing -  
Frequency Range: 0.5...200 Hz - Test No. 5
- 9-119 Histogram of the Resultant Forces at the Bracing -  
Frequency Range: 0.5...200 Hz - Test No. 11
- 9-120 Histogram of the Resultant Forces at the Bracing -  
Frequency Range: 0.5...200 Hz - Test No. 15

PROPRIETARY

- 9-121 Histogram of the Resultant Forces at the Bracing -  
Frequency Range: 0.5...200 Hz - Test No. 1
- 9-122 Direction Distribution of the Resultant Forces at the  
Bracing - Frequency Range: 0.5...200 Hz - Test No. 5
- 9-123 Direction Distribution of the Resultant Forces at the  
Bracing - Frequency Range: 0.5...200 Hz - Test No. 11
- 9-124 Resultant Forces at the Bracing - Frequency Range:  
0.5...200 Hz - Test No. 15
- 9-125 Resultant Forces at the Bracing - Frequency Range:  
0.5...200 Hz - Test No. 1
- 9-126 Direction Distribution of the Resulting Force on the  
Vent-Pipe Bracing - Frequency Range: 0.5...200 Hz - Test  
No. 3...20
- 9-127 Amplitudes of the Resultant Bending Moments at the  
Dummy Quencher - Frequency Range: 0.5...200 Hz - Test  
No. 5 and 6
- 9-128 Amplitudes of the Resultant Bending Moments at the  
Dummy Quencher - Frequency Range: 0.5...200 Hz - Test  
No. 11 and 12
- 9-129 Amplitudes of the Resultant Bending Moments at the  
Dummy Quencher - Frequency Range: 0.5...200 Hz - Test -  
No. 15 and 16
- 9-130 Amplitudes of the Resultant Bending Moments at the  
Dummy Quencher - Frequency Range: 0.5...200 Hz - Test  
No. 1 and 2
- 9-131 Histogram of the Resultant Bending Moments at the Dummy  
Quencher - Frequency Range: 0.5...200 Hz - Test No. 5
- 9-132 Histogram of the Resultant Bending Moments at the Dummy  
Quencher - Frequency Range: 0.5...200 Hz - Test No. 11
- 9-133 Histogram of the Resultant Bending Moments at the Dummy  
Quencher - Frequency Range: 0.5...200 Hz - Test No. 15
- 9-134 Histogram of the Resultant Bending Moments at the Dummy  
Quencher - Frequency Range: 0.5...200 Hz - Test No. 1
- 9-135 Direction Distribution of the Resultant Bending Moments  
at the Dummy Quencher - Frequency Range: 0.5...200 Hz -  
Test No. 5

PROPRIETARY

- 9-136 Direction Distribution of the Resultant Bending Moments at the Dummy Quencher - Frequency Range: 0.5...200 Hz - Test No. 11
- 9-137 Direction Distribution of the Resultant Bending Moments at the Dummy Quencher - Frequency Range: 0.5...200 Hz - Test No. 15
- 9-138 Direction Distribution of the Resultant Bending Moments at the Dummy Quencher - Frequency Range: 0.5...200 Hz - Test No. 1
- 9-139 Amplitudes of the Forces on the I-Beam - Frequency Range: 0.5...200 Hz - Test No. 5 and 6
- 9-140 Amplitudes of the Forces on the I-Beam - Frequency Range: 0.5...200 Hz - Test No. 11 and 12
- 9-141 Amplitudes of the Forces on the I-Beam - Frequency Range: 0.5...200 Hz - Test No. 15 and 16
- 9-142 Amplitudes of the Forces on the I-Beam - Frequency Range: 0.5...200 Hz - Test No. 1
- 9-143 Histograms of the Positive and Negative Force at the I-Beam - Frequency Range: 0.5...200 Hz - Test No. 5
- 9-144 Histograms of the Positive and Negative Force at the I-Beam - Frequency Range: 0.5...200 Hz - Test No. 11
- 9-145 Histograms of the Positive and Negative Force at the I-Beam - Frequency Range: 0.5...200 Hz - Test No. 15
- 9-146 Histograms of the Positive and Negative Force at the I-Beam - Frequency Range: 0.5...200 Hz - Test No. 1
- 9-147 Resultant Forces Measured at the Bracing vs. Break Size and Initial Pool Temperature - Frequency Range: 0.5...200 Hz - MSL Break
- 9-148 Resultant Bending Moments at the Dummy Quencher vs. Break Size and Initial Pool Temperature - Frequency Range: 0.5...200 Hz - MSL Break
- 9-149 Absolute Forces Measured at the I-Beam vs. Break Size and Initial Pool Temperature - Frequency Range: 0.5...200 Hz - MSL Break
- 9-150 Power and Cross Power Spectral Densities of the Bracing Loads - Test No. 13
- 9-151 Power and Cross Power Spectral Densities of the Dummy Quencher Loads - Test No. 1

PROPRIETARY

- 9-152 Pressure Time Histories at the Pool Wall and Vent - Test X1
- 9-153 Pressure Time Histories at the Pool Wall and Vent - Test X1
- 9-154 Pressure Time Histories at the Pool Wall and Vent - Test X1
- 9-155 Observed Oscillation Frequencies in the Pool vs. Time - Test X1
- 9-156 Velocity of Sound vs. Pool Air Content
- 9-157 Air Content in the Water Derived From the Pool Frequencies - Test X1
- 9-158 Pressure Time Histories at Pool Wall and in Vent - Test No. 33
- 9-159 Chugging Frequencies - Test Nos. 4 and 10
- 9-160 Chugging Frequencies - Test No. 11
- 9-161 Chugging Frequencies - Test Nos. 13 and 20
- 9-162 Oscillatory Frequencies of Pressure Events - Test Nos. 1 and 33
- 9-163 Oscillatory Frequencies of Pressure Events - Test Nos. 3...10
- 9-164 Oscillatory Frequencies of Pressure Events - Test No. 11
- 9-165 Oscillatory Frequencies of Pressure Events - Test Nos. 13 and 19
- 9-166 Evaluation of the Traces
- 9-167 Finally Selected Chugging Time Segment - Pressure Time History No. 3
- 9-168 Finally Selected Chugging Time Segment - Pressure Time History No. 5
- 9-169 Finally Selected Chugging Time Segment - Pressure Time History No. 6
- 9-170 Finally Selected Chugging Time Segment - Pressure Time History No. 9
- 9-170a PSD's of the Specified Chug Time Segments

PROPRIETARY

- 9-262a&b CO Pressure Traces From Various Test Break Sizes
- 9-263 Dependence of Largest Mean CO Amplitude on Steam Mass Flux
- 9-264 Comparison of the Envelope of the PSD's of PTH No. 14 with the Mean of the PSD Envelope of Test No. 1 & 2
- 9-265 PSD's of PTH No. 14 with the time expansion and contraction factors
- 9-266 Comparison of Chug Strengths Observed in the JAERI
- 9-267 JAERI Geometry- Actual and the One Used in the Acoustic Model
- 9-268 Comparison of the SSES Chugging Load Definition with the JAERI Test 0002 Data at 1800 mm Elevation
- 9-269 Comparison of the SSES Chugging Load Definition with the JAERI Test 0002 Data at 3600 mm Elevation
- 9-270 Comparison of the Theoretical Frequency Distribution of the Resultant Bracing Forces with the Test Data - Test Nos. 13-18
- 9-271 Schematic of the First Asymmetric Pool Mode
- 9-272 Schematic of ANSYS Model
- 9-273 Comparison of KWU Symmetric and Asymmetric ARS Curves - Direction z - Node 841
- 9-274 Comparison of KWU Symmetric and Asymmetric ARS Curves - Direction z - Node 411
- 9-275 Comparison of KWU Symmetric and Asymmetric ARS Curves - Direction z - Node 771
- 9-276 Comparison of KWU Symmetric and Asymmetric ARC Curves - Direction z - Node 235
- 9-277 Comparison of KWU Symmetric and Asymmetric ARS Curves - Direction x - Node 841
- 9-278 Comparison of KWU Symmetric and Asymmetric ARS Curves - Direction x - Node 411
- 9-279 Comparison of KWU Symmetric and Asymmetric ARS Curves - Direction y - Node 135
- 9-280 Comparison of KWU Symmetric and Asymmetric ARX Curves - Direction x - Node 131

PROPRIETARY

- 9-281 Comparison of Flexible Wall Sonic Speeds in GKM II-M and JAERI Test Facilities
- 9-282 Comparison of the Minimum PSD Envelope of 20 Min. Var. STS Trials with Max. PSD Envelope of JAERI Data at 1.8 M Elevation - 1.3 Amplitude Factor
- 9-283 Comparison of the Minimum PSD Envelope of 20 Min. Var. STS Trials with Max. PSD Envelope of JAERI Data at 1.8 M Elevation - 1.3 Amplitude Factor
- 9-284 Comparison of the Minimum PSD Envelope of 20 Min. Var. STS Trials with Max. PSD Envelope of JAERI Data at 3.6 M Elevation - 1.3 Amplitude Factor
- 9-285 Comparison of the Minimum PSD Envelope of 20 Min. Var. STS Trials with Max. PSD Envelope of JAERI Data at 3.6 M Elevation - 1.3 Amplitude Factor
- 9-286 Comparison of the Minimum PSD Envelope of 20 Min. Var. STS Trials with Max. PSD Envelope of JAERI Data at 1.8 M Elevation - 1.95 Amplitude Factor
- 9-287 Comparison of the Minimum PSD Envelope of 20 Min. Var. STS Trials with Max. PSD Envelope of JAERI Data at 3.6 M Elevation - 1.95 Amplitude Factor
- 9-288 Comparison of the Minimum PRS Envelope for the 20 Min. Var. STS Trials with the Max. PRS Envelope of the JAERI Data - 1.3 Amplitude Factor with 4% Damping
- 9-289 Comparison of the Minimum PRS Envelope for the 20 Min. Var. STS Trials with the Max. PRS Envelope of the JAERI Data - 1.95 Amplitude Factor with 4% Damping
- 9-290 Comparison of the Minimum PRS Envelope for the 20 Min. Var. STS Trials with the Max. PRS Envelope of the JAERI Data - 1.3 Amplitude Factor with 7% Damping
- 9-291 Comparison of the Min. PRS Envelope for the 20 Min. Var. STS Trials with the Max. PRS Envelope of the JAERI Data - 1.95 Amplitude Factor with 7% Damping

PROPRIETARY

SECTIONS 9.4, 9.5 AND 9.6

TABLES

Number

Title

9-1 to 9-5	See Non-Proprietary Section 9.0
9-6	Evaluation Segments
9-7	Dominant Frequencies Measured at Pressure Transducer P6.7
9-8	Mean and Maximum Values of the <u>Positive</u> Pressure Amplitudes - Frequency Range: 0.1...13 Hz
9-9	Mean and Maximum Values of the <u>Negative</u> Pressure Amplitudes - Frequency Range: 0.1...13 Hz
9-10	Mean and Maximum Values of the <u>Positive</u> Dynamic Pressures - Frequency Range: 0.5...13 Hz - Test X1
9-11	Loads On Submerged Structures - Frequency Range: 0.5...13 Hz
9-12	Effect of Steam Mass Flux on the Mean CO Pressure Amplitudes According to Break Size
9-13	CO Time Segments Chosen for PSD Comparison
9-14	Nodal Points Enveloped at Each Elevation

9.4. TEST RESULTS

This section provides a compilation of the test results for the LOCA steam condensation tests conducted in the GKM II-M test facility in Mannheim, West Germany by Kraftwerk Union. Twenty-two test runs were completed during the period from October 1979 to March 1980.

Subsection 9.4.1 presents the time histories of important test parameters (i.e., steam mass flow, steam air content, etc.) measured during selected Main Steam Line (MSL) and Recirculation Line (RCL) break test runs. Subsection 9.4.2 contains a description of the test results for the dynamic pressure loads measured at the pool boundary. Subsection 9.4.3 documents the loads on the vent pipe bracing and submerged structures in the water pool. Finally, Subsection 9.4.4 summarizes the results of the tests. This information is provided in the form of tables, figures and actual Visicorder Traces.

9.4.1. Description of Break Transients.

Once the test facility is prepared per Subsection 9.2.1.1 for the MSL break or Subsection 9.2.1.2 for the RCL break, the rupture disks are broken and the steam flows via the discharge line into the drywell of the test tank S3. The steam mixes with the air initially in the drywell, pressurizes the drywell air and initiates the vent clearing and pool swell phases of the transient.

Subsequently, the condensation phase occurs. This phase can be subdivided into a segment of air-poor condensation (air content of steam sufficiently reduced such that further reduction in air content does not produce higher pressure loads) and later into a segment of air-free condensation.

The processes involved in the condensation of the air-poor and air-free steam in the water pool and the dynamic pressure loads that occur during these processes were the main points of investigation in the GKM II-M Condensation Tests.

9.4.1.1. MSL Break - Steam Mass Flow Transient

Figure 9-15 shows representative plots of the blowdown histories for a full MSL break (Test No. 5), a 1/3 MSL break (Test No. 11) and a 1/6 MSL break (Test No. 15). Each plot represents the steam flow transient into the drywell tank S3. Since quasi-steady-state conditions prevail after the initial drywell pressurization, this can be interpreted as the mean mass flow through the vent pipe.

Upon comparing the "large" and "small" MSL transients, it is evident that the small transient is covered by the end phase (t 55 sec) of the large transient. Of course, a time interval of

approximately 400 sec is then compressed to approximately 20 sec. In addition, the "medium" MSL transient is covered by the end phase of the large transient in which a time interval of approximately 200 sec is compressed into approximately 40 sec.

Figure 9-15a compares the envelope of the full MSL transients run in the test stand (Test Nos. 3-10) to the theoretically calculated full MSL transient for SSES (see Subsection 9.3). This figure indicates that the test transients match the theoretical curve very closely. In the 10 to 30 sec time frame, the full MSL transients exhibit some values below the theoretical curve, reaching at the most about 20%. However, since the theoretical curve represents a conservative upper bound, this slight deviation is not considered significant.

#### 9.4.1.1.1. RCL Break - Steam Mass Flow Transient

Figure 9-16 illustrates the steam mass flux transient for the RCL break Tests No. 1 and 2.

Both transients display an initial monotonic decrease that changes into a quasi-steady-state plateau at about 8 sec after test start and then at about 18 sec after test start resumes the monotonic drop until the termination of the blowdown. The transients in Tests No. 33 and 34, which were run with a higher initial pool temperature of 55°C, are identical to the blowdown history in Test No. 2.

Figure 9-16a shows a comparison of the envelope of the RCL transients with the theoretically calculated transient for SSES (see Subsection 9.3). The test curves conservatively bound the theoretical transient in both duration and mass flow density. The time elongation in the monotonically decreasing steam flow prior to the plateau in the test curves results in the mean temperature of the pool after 10 sec being a few degrees higher than for the design transient and the drywell air being flushed over into the suppression chamber earlier than the design transient. The steeper monotonically decreasing flank after the plateau in the test curves only reduces the duration of this phase from about 23 to 18 sec. Thus, the test runs conservatively represent the RCL break transient.

#### 9.4.1.2. MSL Break - Air Content Transients

Another important test parameter is the air content in the steam. It depends on the air content of the drywell and on the steam supply, and has an influence on the chugging loads in the pool. For that reason, emphasis was placed on adequately simulating the plant parameters when planning the tests.

Figure 9-17 shows the time histories of the air content of the steam flowing through the vent pipe. This figure indicates the

PROPRIETARY

beginning of air-free condensation for each break size as follows:

- Large transient beginning at about 15 sec
- Medium transient beginning at about 50 sec
- Small Transient beginning at about 100 sec

From these times on, the composition of the steam remains essentially constant.

As previously described in Subsection 9.3 tests were also performed with a drywell air content reduced by about 15% (see Table 9-6):

- Test No. 7 and 8, large transient
- Test No. 17 and 18, small transient

As examples, Figure 9-18 shows the air content transients for the full MSL blowdown with 100% (Test No. 5) and approximately 85% air in the drywell at test start (Test No. 7 and 8). A comparison of the duration of air flow reveals no significant difference in the beginning of air-free condensation. The same is also true for the small transients.

9.4.1.2.1. RCL Break - Air Content Transients

Figure 9-19 shows the time variation of the air content in the vent pipe for RCL break Tests No. 1 and 2.

The entire quantity of air has been flushed over after approximately 12 sec, so that only in the initial phase of constant mass flow rate (see Subsection 9.4.1.1.1) is there still a very low percentage of air. Therefore, the largest portion of the steam transient plateau and subsequent decreasing steam mass flow occur in the phase of air-free condensation.

Figure 9-19a correlates the air content in the steam to the steam mass flow densities. This figure clearly shows the differences between the RCL transients and the other transients.

9.4.1.3 MSL Break - Drywell and Suppression Chamber Pressure Transients

The pressure time histories in the drywell and suppression chamber for the full MSL break, 1/3 MSL break and 1/6 MSL break are compared in Figures 9-20, 9-20a and 9-20b (Test No. 5, Test No. 11, and Test No. 15, respectively).

The transient increase of the pressures is terminated when the air from the drywell has been completely purged into the

suppression chamber, (see Subsection 9.4.1.2). The static pressures in the two chambers then remain approximately constant.

In addition, a closer examination of the data shows distinct pressure fluctuations (at about 0.5 to 1 Hz) in both pressure time histories throughout most of the transient. They reach a maximum of  $\pm 0.15$  bar in the drywell and a maximum of  $\pm 0.05$  bar in the suppression chamber and are out of phase with each other.

Two examples of the tests with reduced initial air content in the drywell are shown in Figure 9-21. Here, the pressure-time histories for Tests No. 7 and 8 and for Test No. 5 are compared with each other. There are practically no differences. The same holds true for the corresponding tests with the small transient.

The static pressures in the two chambers at test start and test end are compiled in Table 9.5. The final pressures in the air region of the suppression chamber are 2.7 to 2.9 bar for a 100% air content in the drywell and 2.4 to 2.5 bar for an air content of approximately 85%.

#### 9.4.1.3.1 RCL Break - Drywell and Suppression Chamber Pressure Transients

The pressure-time histories in the drywell and suppression chamber for Tests No. 1 and 2 are plotted in Figures 9-22 and 9-22a, respectively. The data indicates an absence of the pressure fluctuations described in Subsection 9.4.1.3 during the phase of constant mass flow, lasting from approximately 8 sec to 18 sec after test start. The segments before and after that, which correspond to the transient steam-mass-flow variations, exhibit the pressure oscillations described in Subsection 9.4.1.3.

The static pressures in the two chambers at the beginning and at the end of the RCL breaks are indicated in Table 9-5. The final pressures in the air region of the suppression chamber are 2.8 to 3.0 bar.

#### 9.4.1.4. MSL Break - Temperature Variations in the Suppression Pool

For the MSL breaks, three representative measuring points were selected for the presentation of the temperature variations in the water region of the suppression chamber: T 6.1 for the upper region, T 6.3 for the middle region and T 6.8 for the lower region of the pool (see Figure 9-5).

As examples, Figure 9-23 shows the transient heating and mixing of the pool for the different MSL breaks, Tests No. 5, 11 and 15. The initial pool temperature was approximately 33°C.

Examples of temperature variations for the three different initial pool temperatures (24°C, 32°C and 55°C) are illustrated in Figure 9-24 for the full MSL break (Tests No. 3, 5 and 9) and

## PROPRIETARY

in Figure 9-25 for the 1/6 MSL break (Tests No. 14, 15 and 20). All other initial parameters are the same for each test.

### 9.4.1.4.1 RCL Break - Temperature Variations in the Suppression Pool

Figure 9-26 shows the temperature variations in the water region of the suppression chamber for Tests No. 1 and 2. Here again, representative measuring points were selected: T6.1 for the upper region, T 6.3 for the middle region and T 6.8 for the lower region of the pool (see Figure 9-5).

Figure 9-27 is a comparison of the variation of the temperature for the high initial pool temperature of 54°C for Test No. 33 and the low initial pool temperature of 34°C for Test No. 1. Practically no difference exists.

Figure 9-27a shows a comparison of the pool temperature versus steam mass flux for various break sizes. Also marked on the figure are the points at which the air content passes through the values 10%, 1% and 0.1%.

### 9.4.2 Dynamic Pressure Loads at the Pool Boundary

This subsection presents the positive and negative dynamic pressure amplitudes based on statistical evaluations with a differentiated quantification of the parametric influences of break size, initial pool temperature and initial air content in the drywell. As an introduction to that, a characteristic insight into the observed event and oscillation frequencies is given. Finally, a visual impression of the condensation processes is provided by a few excerpts from high-speed film recordings.

#### 9.4.2.1 General Impressions

As a result of the original 4T tests, a LOCA load specification has been defined for the containment boundary loads (see Subsection 4.2.2). This load specification is classified into two distinct regions, consistent with the two types of pressure time histories observed during the 4T tests. The first region occurring during the early portion of the blowdown has been termed "condensation oscillations" and the pressure fluctuations were observed to be sinusoidal in nature. The second region occurring later in the blowdown has been termed "chugging" and was characterized by periodically occurring, higher amplitude pressure fluctuations.

However, the GKM II-M test results indicate an absence of the two distinct condensation regions observed during the 4T tests. A closer examination of the test data showed no clear-cut, consistent method for defining the "condensation oscillation" or "chugging" regions. Thus, in the discussions that follow the

PROPRIETARY

steam condensation phenomenon will not be defined in terms of two distinct regions, but rather the pulsating steam condensations will be arbitrarily termed chugging. This chugging for the purpose of load specification for SSES will cover the entire blowdown history previously broken into two distinct regions.

An insight into the strength of the measured pressure oscillations is provided by the survey diagrams in Figures 9-28 thru 9-36. In pressure-time histories highly compressed in time, these presentations show the variation of the pressure loads in the water pool (measuring points P 6.1... P 6.8, see Figure 9-5) for Tests 3, 5, 9, 11, 14, 15, 20, 1 and 33 throughout the entire test period. The selected examples are representative of the following parameters:

- Break size: Tests No. 5, 11, 15 and 1 (Figures 9-29, 9-31, 9-33 and 9-35); Full, 1/3, 1/6 MS� breaks and RCL breaks.
- Initial water temperature: Tests No. 3, 5 and 9 (Figure 9-28, 9-29, and 9-30; Full MS� break).
- Initial water temperature: Tests No. 14, 15 and 20 (Figures 9-32, 9-33 and 9-34; 1/6 MS� break).
- Initial water temperature: Tests No. 1 and 33 (Figures 9-35 and 9-36; RCL break).

In most instances the pressure fluctuations are recognized as having the character of events. That is suddenly excited pressure amplitudes followed by periods of smaller amplitude damped oscillations. It can be seen that the process of chugging is stochastic during the phase of air-poor and air-free steam flow through the vent pipe into the water pool.

There are large differences in the amplitudes of consecutive events. This fact is also demonstrated by the video and high-speed films: Two consecutive events differ considerably with respect to the shape and maximum size of the steam bubble (see Subsection 9.4.2.1.4).

Essentially independent of the break size and the initial pool temperature, the pressure-time histories in Figure 9-28 thru 9-36 exhibit higher amplitudes in the period around the middle of the test, but lower amplitudes at the beginning and at the end of the test. As examples, Figure 9-37 thru 9-54 show details from these pressure-time histories on a more expanded time scale. These are copies of the original Visicorder No. I traces from two segments each in Tests No. 3, 5, 9, 11, 14, 15, 20 (MS� breaks), 1 and 33 (RCL breaks). Figure 9-36a identifies the sensor and scale used for each trace in Figures 9-37 to 9-54.

9.4.2.1.1 Frequency (of Oscillations) Analysis

To evaluate the dynamic pressure loads in the pool, the frequency spectrum is used in addition to the pressure-time history. It is common to display the frequency spectrum in the form of a so-called power spectral density (PSD). It is calculated by means of a Fourier transformation using the equation indicated in Figure 9-55.

The power spectral density is represented as the square of the root-mean-square value of the relevant physical variable  $x(t)$ , with respect to frequency, and has corresponding dimensional units, e.g.,  $\text{bar}^2/\text{Hz}$ . It is a measure of the intensity of the frequencies occurring in the region under consideration.

For example, the following frequencies can be determined:

- The frequency of the spacing between events (chugging frequency).
- The frequency of the acoustic oscillation of the water in the pool ("pool acoustics").
- The frequency of the acoustic oscillation of the steam column in the vent pipe ("vent acoustics").
- Possibly present tape noise frequencies and/or those frequencies at which the intensity of the process is relatively small and which may be able to serve as fundamental frequencies for a low-pass or high-pass filtering.

9.4.2.1.1.1 Oscillation Frequencies

The analyses were performed with the Fourier System HP 5451 A. This system provided a frequency resolution of  $\pm 0.5$  Hz at the required upper frequency cut-off of 500 Hz and the desired segment length of one second for the analysis of individual events. All PSD's were calculated by the Hanning function.

In principle, the power spectra were determined throughout the "entire" test period for the pressure measuring points P 6.4 and P 6.7 (tank wall, Figure 9-5) and P 6.8 (tank bottom, Figure 9-5) for all tests. The beginning and end of each evaluation segment are indicated in Table 9-6. As shown below, the determined PSD's exhibit frequency-dependent differences between the individual pressure measuring points. The spectra calculated from the three pressure transducers practically coincide in the range from 6 to 10 Hz. The higher the frequency, the smaller is the agreement, i.e., the low-frequency pressure oscillations (air bubble oscillation under water and vent acoustics) act in the pool beneath the vent pipe with the same intensity. In contrast, for the higher-frequency pressure oscillations there are distinct

## PROPRIETARY

differences between measurement locations which are due to local effects.

Representative examples of these PSD's for the MSL breaks can be found in Figures 9-56 to 9-58. The PSD's of the pressure measuring point P 6.7 were selected for presentation. In particular:

- Figure 9-56 with the PSD's of Tests No. 5, 11 and 15 shows the influence of the break size.
- Figure 9-57 with the PSD's of Tests No. 3, 5 and 9 shows the influence of the initial water temperature for the full MSL breaks.
- Figure 9-58 with the PSD's of Tests No. 14, 15 and 20 shows the influence of the initial water temperature for the 1/6 MSL breaks.

Corresponding examples for the RCL breaks are shown in the top part of Figures 9-59 and 9-60, with Test No. 1 having a mean initial water temperature and with Test No. 33 for the high initial water temperature. In addition, the middle and bottom parts of the figures illustrate the PSD's that were determined separately for the phase of steady-state and monotonically decreasing steam flow, respectively.

The frequencies corresponding to the maxima of the determined power densities for the measuring point P 6.7 in the range from 0 to 100 Hz for all tests are compiled in Table 9-7. These values were sorted by their intensity within a test (density class), i.e., the first of the indicated maxima corresponds to the dominant frequency in all instances.

For the evaluation of the illustrated results, the frequency resolution of 0.5 Hz is of special significance in the lower range of frequencies. Furthermore, limits are imposed on the evaluation of low power densities by the noise level of the measurement and evaluation chain. For all three pressure signals (P 6.4, P 6.7 and P 6.8), that limit lies on the average at  $10^{-6}$  bar<sup>2</sup>/Hz in the lower frequency range and at  $10^{-7}$  bar<sup>2</sup>/Hz in the upper frequency range. The latter is the main reason for the restriction to only 100 Hz, since only values below these power densities occurred at higher frequencies.

### 9.4.2.1.1.2. Event Frequencies

Reference was already made in Subsection 9.4.2.1 to the periodically occurring, pulsating pressure fluctuations in the pool. This process, termed "chugging," was the dominant form of condensation observed in the GKM II-M tests. The water penetrates more or less intensely into the vent pipe.

PROPRIETARY

This process can be seen particularly well at the measuring point T 5.6 (temperature at the end of the vent pipe) and at the so-called "level probes" (see Figure 9-5). As an example, Figure 9-61 shows the variation of the measuring points T 5.6, LP 5.1 ... LP 5.5, P 5.4 and P 6.4 throughout the entire test period of Test No. 5.

The periodic wetting of the level probes (especially LP 5.1 - LP 5.3) is clearly recognizable in the second half of the test. At the same time, the measuring point T 5.6 exhibits distinct temperature changes between "warm" and "cold" (the water emerges from the vent pipe and enters into the pipe, respectively). The Figures 9-62 thru 9-79 show detailed examples of this phenomenon. These are copies of the original Visicorder No. III traces for two segments each from Tests No. 3, 5, 9, 11, 14, 15, 20 (MSL breaks), 1 and 33 (RCL breaks). Figure 9-61a identifies the sensor and scale used for each trace in Figures 9-62 thru 9-79. In the first half of each test one can still recognize a comparable pressure fluctuation in the pipe (measuring point P 5.4), but no "pronounced" wetting of the level probes. The steam mass flow rate is obviously large enough here in comparison to the condensation rate that the steam/water interface does not penetrate into the pipe.

Whereas the time intervals between chugs or events depends very strongly on the steam mass flow transients, it varies less conspicuously within a given test for mass fluxes below 40 kg/m<sup>2</sup>s. A statistical evaluation of the pressure-time histories in the pool was performed to determine the mean event interval for the different transients. The results are presented below:

<u>Break Size</u>	<u>Mean Event Interval</u>	<u>Mean Event Frequency</u>
Full MSL break	1 sec	1 Hz
1/3 MSL break	1.5 sec	0.7 Hz
1/6 MSL break	2 sec	0.5 Hz
*RCL break	1 sec	1 Hz

These results fit smoothly into the curve illustrated in Figure 9-80.

\*For the phase of steadily decreasing steam mass flow rates.

9.4.2.1.2 Statistical Evaluation

The influences of individual test parameters can be essentially determined from mean values, since those values are significantly more typical than the magnitude of individual rare maximum values. In general, these trends are supported by the maximum values.

Therefore, to quantify the effects of parameters, the tests were evaluated statistically by means of digital computers. Two main requirements were imposed on that evaluation:

- Correlation of amplitude components and the oscillation frequency, i.e., a "frequency-oriented" evaluation.
- Determination of the maximum values for each event, i.e., an "event-oriented" evaluation.

To meet the first requirement, two frequency bands were specified, taking into consideration the frequency analyses described in Subsection 9.4.2.1.1.1:

- a low-frequency band with a range from 0.5 to 13 Hz,
- a high-frequency band with a range from 10 to 100 Hz.

The low-frequency band was to include all low-frequency amplitude components up to the vent acoustics (approximately 9 Hz) with correct amplitude. The high-frequency band was limited at 100 Hz in order to eliminate the locally occurring so called pressure spikes (see Figures 9-37 to 9-54), which can unrealistically falsify the load assumed around the entire containment.

The second requirement imposed on the statistical evaluation was satisfied by interrogating the pressure-time histories stored on the magnetic tape for the positive and negative maximum value in constant intervals of time. The constant time intervals were selected according to the mean event intervals indicated in Subsection 9.4.2.1.1.2.

The pressure-time histories were evaluated for the measuring points P 6.4 and P 6.7 (wall pressures) and P 6.8 (bottom pressure; see Figure 9-5).

9.4.2.1.2.1 Amplitude Components of the Low-Frequency and High Frequency Bands

The time segment of each test indicated in Table 9-6 was evaluated by computer in the manner described in Subsection 9.4.2.1.2. The beginning of the evaluation segments was selected so that the "static" pressure rise was completed and thus only the dynamic pressure components were considered.

PROPRIETARY

The determined pressure amplitudes (low-frequency, high-frequency) were plotted versus time in graphs for the pressure transducer P 6.7, using the magnitude of the maximum amplitude in each interrogation interval. Tests with identical initial conditions (Test/Repeat Test: 1/2, 3/4, 5/6, etc.; see Table 9-4) were each combined in one graph. This gives an insight into the reproducibility (see Subsection 9.4.2.1.5).

The formation of mean values was accomplished by defining large test segments within which the arithmetic mean of the amplitudes was calculated. These test segments have different lengths for the individual test groups and are indicated below:

<u>Break-Size</u>	<u>Time Interval for the Averaging</u>
Full MSL break	5 sec
1/3 MSL break	15 sec.
1/6 MSL break	30 sec
RCL break	5 sec

Tests that were run with identical initial conditions were combined for the averaging. The calculated mean values were assigned to the middle of the interval and also plotted in the graphs (straight lines).

Examples of the results of the analysis for different break sizes are shown in Figures 9-81 to 9-84. Pairs of tests that were performed with an initial water temperature of 32° C were selected:

<u>Break-Size</u>	<u>Test Pair</u>	<u>Illustrated in</u>
Full MSL break	5/6	Figure 9-81
1/3 MSL break	11/12	Figure 9-82
1/6 MSL break	15/16	Figure 9-83
RCL break	1/2	Figure 9-84

The top half of each figure shows the results for the low-frequency range and the bottom half shows the results for the high-frequency range. The time "0s" corresponds to "Test Start."

To facilitate comparison, the mean value straight lines are illustrated together in Figure 9-85 for Tests 3-10 (Full MSL break), Figure 9-86 for Tests 11-20 (1/3 and 1/6 MSL breaks), and Figure 9-87 for Tests 1, 2, 33 and 34 (RCL break). From the mean-value curves it can be determined that in all the tests,

## PROPRIETARY

both in the low-frequency and also in the high-frequency range, the pressure amplitudes have small values at test start, increase to higher values as the test period progresses and drop back to low values again at the end of the test (see Subsection 9.4.2.1). The mean pressure amplitude reaches a value of up to approximately 1.3 bar in the low-frequency band and up to approximately 1.9 bar in the high-frequency band. Furthermore, the maximum deviations of the pressure amplitudes are larger in the high-frequency band than in the lower band (see Figures 9-81 thru 9-84).

Test No. 13 was used to investigate the correct selection of the lower frequency cut-off of the high frequency band. The lower frequency cut-off was varied by using different high-pass filter settings, so that the following frequency ranges could be compared:

10 - 100 Hz

12 - 100 Hz

15 - 100 Hz

The result is illustrated in Figure 9-88 in the form of mean-value straight-line curves. It can be seen that the curves lie very close to one another and that the curve for the range from 10 to 100 Hz practically envelopes the other two curves. Accordingly, the stipulation of the lower frequency-cut-off at 10 Hz can be considered conservative. Furthermore, the falsification of the results for the high-frequency band by "residues" of the low-frequency band is negligible.

### 9.4.2.1.2.2 Frequency (of occurrence) Distributions

To prepare amplitude histograms for the low-frequency band, the positive and negative pressure amplitudes determined by computer were classified into frequency of occurrence classes with a uniform class-interval of 0.05 bar. The histograms were normalized uniformly to 100 readings so as to permit direct comparisons of the tests with one another. Here too, the tests with identical initial conditions were combined in one histogram. It was found that the parameters "water temperature and air content in the drywell at test start" have no significant influence on the shape of the distribution. Accordingly, all tests that were run with the same break size were also combined.

Figures 9-91 to 9-99 present comparisons of the frequency of occurrences distributions of the positive and negative dynamic pressure amplitudes for measuring points P 6.4, P 6.7 and P 6.8 for the different groups of tests corresponding to the four break

PROPRIETARY

sizes. Table 9A gives an overview of the assignments for the individual plots:

PROPRIETARY

TABLE 9A: Histograms of the dynamic pressure amplitudes in the low frequency band (0.5 to 13 Hz)

Fig.	Break Size	Tests	Transducers	Dynamic pressure amplitudes			
				Histogram	Max. value bar	Mean value bar	
9-91	Full MSL	3...10	P 6.4	x	1.46	0.46	
	1/3 MSL	11/12			1.51	0.36	
	1/6 MSL	13...20			1.12	0.31	
9-92	Full MSL	3...10	P 6.4	x	-1.41	-0.31	
	1/3 MSL	11/12			-0.89	-0.29	
	1/6 MSL	13...20			-0.94	-0.26	
9-93	Full MSL	3...10	P 6.7	x	1.91	0.56	
	1/3 MSL	11/12			1.60	0.38	
	1/6 MSL	13...20			1.38	0.34	
9-94	Full MSL	3...10	P 6.7	x	-1.24	-0.37	
	1/3 MSL	11/12			-0.95	-0.30	
	1/6 MSL	13...20			-0.99	-0.28	
9-95	Full MSL	3...10	P 6.8	x	1.99	0.58	
	1/3 MSL	11/12			1.59	0.39	
	1/6 MSL	13...20			1.44	0.34	
9-96	Full MSL	3...10	P 6.8	x	-1.54	-0.39	
	1/3 MSL	11/12			-0.98	-0.31	
	1/6 MSL	13...20			-1.00	-0.28	
9-97	RCL	1, 2, 33, 34	P 6.4	x	0.60	0.24	
					x	-0.60	-0.20
					x	1.23	0.39
9-98	RCL	1, 2, 33, 34	P 6.7	x	-0.68	-0.28	
					x	1.31	0.42
					x	-0.68	-0.29
9-99	RCL	1, 2, 33, 34	P 6.8	x	-0.68	-0.29	

Indicated in the last two columns of Table 9A is the maximum value and the joint mean value for the individual test groups. The joint mean value was obtained by first averaging all the maximum amplitudes per mean event interval for a given test to obtain the mean value for the transient and then averaging these mean values for the same test group (i.e., 3...10, 11/12, etc.).

9.4.2.1.2.3 Statistical Characteristics

Table 9-8 gives an overview of the mean and maximum values of positive pressure amplitudes measured by transducers P 6.4, P 6.7 and P 6.8 in the low-frequency band for all 22 tests. Likewise, Table 9-9 presents the negative mean and maximum values for all 22 tests.

PROPRIETARY

The mean values were determined by the grouped data procedure, using the following equation:

$$\bar{P} = \frac{\sum_{i=1}^k n_i \cdot \bar{P}_i}{\sum_{i=1}^k n_i}$$

where:  $\bar{P}$  = Mean value  
 $\bar{P}_i$  = Mean value of each class  
 $n_i$  = Frequency of each class

The maximum values at the different measuring points need not have occurred at the same time, although that is generally the case.

The sensitivity of the evaluation with respect to the interrogation interval was investigated by using the shakedown Test No. XI so as to be able to specify the procedure for further evaluation of the GKM II-M tests. For that test, which corresponds to a 1/6 MSI break the statistical analysis was performed for an interrogation "Maximum value every 2.0 sec" (mean event interval) as well as an interrogation "Maximum value every 1.75 sec" (most frequent event-interval). Table 9-10 indicates that the interrogation interval has only a slight effect on the results. The mean values for measuring points P 6.4, P 6.7 and P 6.8 differ from one another by only about 3% in the two interrogations. This investigation has shown that sufficiently exact results are obtained with the interrogation "Maximum value every mean event-interval".

A maximum error of the single value of approximately  $\pm 0.1$  bar can be indicated for the maximum pressure amplitudes listed in Tables 9-8 and 9-9. This indication is based on an error estimate which is composed of the systematic measurement error, recording error and evaluation error (see Subsection 9.2.2.7).

Assuming that the errors of the dynamic components practically cancel out in the formation of mean values, an order of magnitude of approximately  $\pm 0.02$  bar remains for the maximum error of the mean value. This residual error is composed of the possible zero-point shift of the analog measurement signal at the computer input and the error band of the method used for classification and averaging.

9.4.2.1.3. Parameter Influences

The evaluation of possible parameter influences discussed in the next three (3) subsections is based on the mean value of the pressure amplitudes for the entire duration of the test (see Subsection 9.4.2.1.2.3 and Table 9-8 & 9-9).

9.4.2.1.3.1 Influence of the Break Cross-Sectional Area

The most important goal of the GKM II-M tests, namely to determine the dependence of the steam condensation loads on the postulated break size, was achieved.

Figures 9-100 and 9-101 show a plot of the positive and negative mean values vs. the simulated break cross-sectional area for the measuring point P 6.7. The values for all the MSL break tests are included in these plots. The result is an increase of the pressure values with increasing break size. The positive mean values increase from approximately 0.35 bar for the 1/6 MSL break to approximately 0.55 bar from the full MSL break. In contrast, the negative mean values increase only from approximately 0.25 bar to approximately 0.35 bar.

9.4.2.1.3.2 Influence of the Initial Pool Temperature

The positive and negative mean values of the measuring point P 6.7 as a function of the initial pool temperature are illustrated in Figure 9-102 and 9-103 for the full MSL breaks, in Figures 9-104 and 9-105 for the 1/6 MSL breaks and in Figures 9-106 and 9-107 for RCL breaks. With the exception of the positive pressures for the RCL breaks in Figure 9-106, the figures show no influence or only a slight influence of the initial pool temperature on the magnitude of the pressure amplitudes. The slightly more distinct increase of the positive values for the RCL breaks is attributed primarily to the higher level of amplitudes measured during the phase of steady-state steam mass flow in Tests No. 33 and 34 with the higher initial pool temperature at test start.

9.4.2.1.3.3 Influence of the Initial Air Content in the Drywell

Subsection 9.4.1.2 indicates that a 15% reduction in the initial drywell air content has no significant influence on the beginning of air-free condensation. In addition, Figures 9-102 to 9-105 reveal that the resulting 0.4 bar lower back-pressure in the suppression chamber associated with the reduction in initial air content has no significant influence on the dynamic pressure loads. Tests No. 7 and 8 (Full MSL break, Figures 9-102 and 9-103) and Tests No. 17 and 18 (1/6 MSL break, Figures 9-104 and 9-105), performed with a reduced air content at a mean initial pool temperature of 32°C, fit readily into the scatter zone of the comparison tests.

PROPRIETARY

Therefore, no significant dependence of the pressure amplitudes can be found in the range of suppression-chamber pressure having relevance for SSES.

9.4.2.1.4. Correlation of Film and Pressure Recordings

As previously mentioned, Stanford Research Institute International (SRI) provided two LOCAM, Model 51-0003, high-speed cameras for filming the process in the pool.

These two cameras were mounted in front of the bull's-eyes of the large manhole, approximately 0.6 m below the end of the vent pipe (see Figure 9-3).

The correlation of the film recordings with the data recordings on Visicorders and magnetic tape was accomplished by recording the same time signal on these recording devices.

Test No. 15 was used for the following assessment. The parameters at test start are listed in Table 9-5.

Figures 9-108 to 9-112 show a sequence of 10 instantaneous photographs (called "Pictures" in the following) during the chugging phase. The pressure-time histories recorded for this event at the pressure measuring points P 6.4 and P 6.7 (Figure 9.5) are illustrated below each picture. The time "0 ms" corresponds to 269 sec after test start. The steam mass flow rate at that instant is 11 kg/m<sup>2</sup>s and the pool temperature is 60 - 65°C.

The frame rate was 200 pictures/sec. A reference line in Figures 9-108 to 9-112 provides the connection between picture and pressure trace.

The process of chugging can be followed well in Figure 9-108 to 9-112. At the beginning of the chugging phase, a "hemispherical" steam bubble develops at the end of the pipe. It does not remain constant, but rather it alternately expands and then collapses again. The actual origin of the pressure events is the rather violent condensation of the steam when it contacts the subcooled water (steam bubble collapse) at the outlet of the vent pipe. Due to the resulting underpressure, there is a more or less intense movement of the water into the pipe and back out again ("chugging"). As described in Subsection 9.4.2.1.1.2 this process is repeated at almost identical intervals.

Now to the film recordings:

The reference is Picture a in Figure 9-108 at the relative time 0 ms. A striated front at the end of the vent pipe indicates the beginning of a steam bubble formation.

PROPRIETARY

In Picture b in Figure 9-108 at the relative time 200 ms, the development of a steam bubble is already clearly discernible. Only extremely small pressure fluctuations are indicated in the pressure traces P 6.4 and P 6.7.

In Picture c in Figure 9-109 at the relative time 300 ms, the steam bubble has enlarged and begins to enclose the end of the pipe.

In Picture d in Figure 9-109 at the relative time 400 ms, the steam bubble has enlarged further and has completely enclosed the end of the pipe. The boundary surface between water and steam can be recognized.

In Picture e in Figure 9-110 at the relative time 500 ms, the steam bubble begins to collapse and to pulsate. This pulsation and the incipient underpressure phase is clearly recognizable in the pressure traces P 6.4 and P 6.7.

In Picture f in Figure 9-110 at the relative time 550 ms, the steam bubble has diminished further. The end of the pipe is again visible.

At the relative time 600 ms in Picture g in Figure 9-111, the steam bubble has shrunk further and is visible only in a shadowy manner. The underpressure phase is clearly recognizable in the pressure traces.

In Picture h in Figure 9-111 at the relative time 650 ms, a small part has pinched off from the almost completely condensed steam bubble and has begun to pulsate. This pulsation is visible in the pressure traces P 6.4 and P 6.7.

In Picture i in Figure 9-112 at the relative time 700 ms, the steam bubble has completely condensed except for the pinched-off part.

In Picture j in Figure 9-112 at the relative time 800 ms, the steam bubble has completely condensed and the water has entered into the pipe.

In addition, Figure 9-113 shows two instantaneous photographs of the vent-clearing process for different break sizes. The top picture represents the process at 0.37 sec after test start for a full MSL break (Test No. 3). The bottom picture shows the vent clearing at 1.08 sec after tests start for a 1/6 MSL break (Test No. 18). These two pictures illustrate the expulsion of water and water-air mixture, respectively.

9.4.2.1.5 Repeat Tests and Reproducibility of the Results

To verify the reproducibility of the measurement results, the Test Matrix (Table 9-4) stipulated a repetition of each test resulting in 11 pairs of tests.

A comparison of the associated repeat tests with respect to the mean values of the positive dynamic pressure amplitudes at the measuring point P 6.7 (Table 9-8) gives an insight into the quality of the reproducibility.

The maximum deviations from the joint mean value of the pair of tests in each instance are as follows:

- for the full MSL breaks                     $\pm 0.04$  bar or  $\pm 7\%$
- for the 1/3 MSL breaks                     $\pm 0.02$  bar or  $\pm 6\%$
- for the 1/6 MSL breaks                     $\pm 0.02$  bar or  $\pm 6\%$
- for the RCL breaks                         $\pm 0.05$  bar or  $\pm 15\%$

Figures 9-81 to 9-84 provide an idea of the scatter of the individual values (see Subsection 9.4.2.1.2). The test results follow identical trends within the range of the scatter.

Accordingly, we can state:

If the initial conditions of the tests are adjusted in a controlled manner within the prescribed tolerances, then the test results are reproducible.

9.4.3 Loads in the Vent-Pipe Bracing, Dummy Quencher and I-Beam

In this subsection, a discussion of the results of the measured loads on the vent-pipe bracing, dummy quencher and I-beam are presented. In addition, an evaluation of the influence of the test parameters on the load is made.

The measuring points provided for them are (see Figures 9-7 to 9-9):

- SG 6.1 and 6.2: Longitudinal forces in the bracing
- SG 6.7 and 6.8: Bending moments at the dummy quencher
- LC 6.1: Bearing forces on the I-beam

Strains were measured at all the measuring points. From the measured strains, the loads that produced those strains were calculated. Thus, in all cases we are dealing with pure

PROPRIETARY

measurement values that are not directly transposable to plant conditions but rather still require an evaluation.

9.4.3.1. Statistical Evaluation

Analogous to the statistical evaluation of the dynamic pressure loads in the pool, the loads on the internals are illustrated by exemplary plots of the forces and bending moments calculated from the measured strains vs. time and the resulting frequency distributions. In addition, the distribution of directions of the resultant bracing forces and bending moments at the dummy quencher is presented by means of "point correlations."

9.4.3.1.1 Frequency Distributions of the Resultant Bracing Forces

To measure the longitudinal forces in the bracing, the strain gauges SG 6.1 and SG 6.2 were mounted on the bracing pipes (see Figures 9-6 and 9-7). For symmetry reasons and in order to eliminate bending strains, two strain gauges displaced by 180° were mounted along the bracing pipe and connected to form a complete bridge to measure the normal forces.

The strut forces F were calculated from the measured strains by using the following equation:

$$F = A \cdot \sigma$$

where: A = Cross-sectional area of strut pipe

$\sigma$  = Normal stress

Hooke's law is valid for the elastic range and gives:

$$\sigma = E \cdot \epsilon$$

where: E = Modulus of elasticity

$\epsilon$  =  $\mu\text{m}/\text{m}$  measured strain

Combining the above equations yields:

$$F = A \cdot E \cdot \epsilon$$

The vent pipe bracing constants are:

$$A = 2478.7 \text{ mm}^2$$

$$E = 2.06 \times 10^2 \text{ kN/mm}^2$$

Inserting these factors gives:

$$F = 0.511 \cdot \epsilon \text{ kN}$$

PROPRIETARY

To determine the resultant bracing forces, the signals of measuring points SG 6.1 and SG 6.2 were digitized for identical times. Taking into consideration the direction of action (90°, see Figure 9-6), the associated measurement values were added vectorially and the resulting resultant forces were sorted by magnitude. As in the evaluation of the pressure loads, only the maximum values for each event were determined. The event interval for the different break sizes was not changed from the values indicated in Subsection 9.4.2.1.1.2. The evaluation was carried out throughout the entire test period in a frequency range from 0.5 to 200 Hz (see Subsection 9.4.3.3).

The calculated resultant bracing forces were plotted in graphs vs. time, using the magnitude of the maximum resultant in each interrogation interval. Here too, the tests with identical initial conditions (see Table 9-4) were combined into one graph.

As examples, Figures 9-114 to 9-117 show these graphs for the different break sizes. In each instance pairs of tests that were run with an initial water temperature of 32°C were selected:

<u>Break Size</u>	<u>Test Pair</u>	<u>Illustrated in</u>
Full MS1 break	5/6	Figure 9-114
1/3 MS1 break	11/12	Figure 9-115
1/6 MS1 break	15/16	Figure 9-116
RCL break	1/2	Figure 9-117

In addition, Figures 9-118 to 9-121 classifies the maximum resultant bracing force for each event interval into histograms. The class interval is uniformly 5 kN. For the reasons mentioned in Subsection 9.4.3, no normalization was made, i.e., the examples in Figures 9-118 to 9-121 are absolute-value histograms. Therefore, each of those histograms contains only the results for one test (No. 5, 11, 15 and 1).

9.4.3.1.2 Distribution of Direction of the Resultant Bracing Forces

A point correlation method was used to determine the direction distribution of the resultant bracing forces. At identical instants of time, instantaneous values were taken from the load-time functions and recorded in a manner correlated with one another. The instants of time were determined by the reversal points of the guide trace. In two computation runs, the guide trace and correlation trace were interchanged. The results of the two computation runs are combined in one graph for each test. The resulting maximum values can be distinguished from the maximum values by the method described in Subsection 9.4.3.1.1 within the evaluation accuracy of  $\pm 3$  kN.

PROPRIETARY

Examples of these correlations for Tests No. 5, 11, 15 and 1 are shown in Figures 9-122 to 9-125. These depictions provide no information about the frequency (of occurrence) distributions of the resultant forces. A point can also include frequencies of occurrences > 1.

When analyzing Figure 9-122 to 9-125, no significant preferred directions are discernible, but rather the "point accumulations" hint at an isotropic distribution. In addition, the summary of all MSL breaks (Tests No. 3 to 20) in Figure 9-126, show no apparent preferred direction for the higher values of the resultant bracing forces. The positions of the braces are at 0° (bracing 1) and 90° (bracing 2). In this illustration values < 25 kN were omitted.

9.4.3.1.3 Frequency Distributions of the Resultant Bending  
-----Moments at the Dummy Quencher-----

In the GKM II-M condensation tests, the bending moments at the dummy quencher were measured in the horizontal plane (parallel to the bottom of the test tank) and also in the vertical plane. For that purpose, two strain gauges were connected such that they only recorded the nonsymmetrical component of the normal stresses. The following strain gauges were mounted for that purpose (see Figure 9-8):

- SG 6.7: Moment in the vertical direction
- SG 6.8: Moment in the horizontal direction.

Using the equation indicated in Subsection 8.5.2.3.3.1

$$M_B = 0.38 \cdot \epsilon \quad \text{kNm}$$

with  $\epsilon$  in  $\mu\text{m}/\text{m}$ , the measured bending strains were converted into bending moments.

The evaluation of the bending moments relates to the resultant bending moment, i.e., the bending moment which actually loads the quencher arm. The maximum resultant bending moment for each event was determined by the same method as was used for the bracing forces (see Subsection 9.4.3.1.1). Here too, the evaluation was performed throughout the entire test period in the frequency range from 0.5 to 200 Hz (see Subsection 9.4.3.3)

Figures 9-127 to 9-130 present the results as plots vs. time for the different break sizes. Once again, the tests with identical initial conditions are combined into one graph.

PROPRIETARY

The selected examples are as follows:

<u>Break Size</u>	<u>Test Pair</u>	<u>Illustrated in</u>
Full MSL break	5/6	Figure 9-127
1/3 MSL break	11/12	Figure 9-128
1/6 MSL break	15/16	Figure 9-129
RCL break	1/2	Figure 9-130

Figures 9-131 to 9-134 show the histograms of the resultant bending moments with the uniform class interval of 5 kNm. These are absolute-value histograms for Tests No. 5, 11, 15 and 1.

9.4.3.1.4 Direction Distribution of the Resulting Bending Moments at the Dummy Quencher

When applied to the measured bending strains, the point correlation method described in Subsection 9.4.3.1.2 indicates that the maximum bending strains and bending moments occur preferentially in the vertical direction. The contribution of the horizontal component SG 6.8 to the resultant can almost be neglected, so that the bending moments measured at the measuring point SG 6.7 can practically be equated to the resultant moment.

As examples, Figures 9-135 to 9-138 show the point correlations of the resultant bending moments for Tests No. 5, 11, 15 and 1, respectively. Here too, the maximum values can deviate from the results described in Subsection 9.4.3.1.3 within the evaluation accuracy of  $\pm 6$  kNm.

9.4.3.1.5 Frequency Distributions of the Forces on the I-Beam

For symmetry reasons and in order to eliminate bending moments at the measurement bolt, two strain gauges displaced by  $180^\circ$  were mounted longitudinally in the middle of the bolt and connected to form a complete bridge for the measurement of normal forces (measuring points LC 6.1 in Figure 9-9).

The statistical evaluation of the measurement signals was again accomplished using the method described in Subsection 9.4.3.1.1, but was performed separately for the positive vertical forces (directed upward) and the negative vertical forces (directed downward).

The positive and negative maximum values vs. time for each event interval are plotted in Figure 9-139 to 9-141 for the test pairs no. 5/6, 11/12 and 15/16 (MSL breaks). In addition, Figure 9-142 shows the corresponding results for the Test No. 1 (RCL break).

Figures 9-143 to 9-146 illustrate the absolute-value histograms of the positive and negative vertical forces on the I-beam for the frequency range from 0.5 to 200 Hz. The class interval is uniformly 5 kN. As for the bracing forces and the bending moments at the dummy quencher, the histograms for Tests No. 5, 11, 15 and 1 were selected as examples. The results of this evaluation are static equivalent loads and again are not directly transposable to plant conditions.

9.4.3.1.6. Statistical Characteristics

Table 9-11 provides an idea of the most important statistical characteristics of the loads on the internals in the water region of the test tank for all 22 tests. They include:

- maximum and mean values for the resultant bracing forces,
- maximum and mean values of the resultant bending moments at the dummy quencher,
- maximum and mean values of the vertical forces on the I-beam, for the frequency range from 0.5 to 200 Hz.

The mean values were determined by the single data procedure, using the equation indicated below:

$$\bar{P} = \frac{\sum_{i=1}^k P_i}{n}$$

- where:
- $\bar{P}$  = Mean value
  - $P_i$  = Single value
  - n = Total number of values

The absolute maximum measurement values of the resultant bracing forces, resultant bending moments and vertical forces at the I-beam and the maximum mean values for these loads are shown below:

<u>Absolute Maximum Value of the Load</u>	<u>Measured in Test</u>	
Resultant bracing force	88.7 kN	No. 17
Resultant bending moment at the dummy quencher	79.6 kNm	No. 11
Vertical force at the I-beam	32.0 kN	No. 4

PROPRIETARY

<u>Maximum Mean Value of the Load</u>		<u>Measured in Test</u>
Resultant bracing force	22.5 kN	No. 18
Resultant bending moment at the dummy quencher	16.1 kNm	No. 12
Vertical force at the I-beam	4.4 kN	No. 12

9.4.3.2. Parameter Influences

The influence of the test parameters "Break size and water temperature at test start" is illustrated in graphs in which the mean values of the load on the internals in the pool are plotted versus the above-cited parameters. A separate illustration is not necessary for the parameter "Air content in the drywell at test start", since, as expected, this parameter has no significant influence.

9.4.3.2.1. Influence of the Break Cross-Sectional Area

In the top half of each of Figures 9-147 to 9-149, the mean values of the resultant bracing forces and bending moments at the dummy quencher and of the vertical forces on the I-beam are plotted vs. break size. For the vertical forces, the mean value which was larger in absolute magnitude was used for each test.

Figure 9-147 indicates a decreasing trend in the magnitude of the bracing forces with increasing break size. In contrast, Figures 9-148 and 9-149 indicate the loads on the dummy quencher and I-beam exhibit a maximum for the medium break size (1/3 MSL break).

9.4.3.2.2. Influence of the Initial Pool Temperature

The bottom half's of Figures 9-147 to 9-149 illustrate the mean values of the resultant bracing forces, bending moments at the dummy quencher and of the vertical forces on the I-beam as a function of the initial pool temperature. There is uniformly indicated here a more or less significant decreasing trend for the loads with increasing initial pool temperature.

9.4.3.2.3. Influence of the Initial Air Content in the Drywell

This parameter has no significant influence on the magnitude of the loads on the internals in the pool. This can clearly be seen from the bottom half of each of the Figures 9-147 to 9-149. The mean values of Tests No. 7 and 8 (Full MSL breaks) and Test No. 17 and 18 (1/6 MSL breaks) with approximately 85% initial air content in the drywell vary (as for the dynamic pressure loads; see Subsection 9.4.2.1.3.3) within the same scatter range as the comparable Tests No. 5, 6 and No. 15, 16, respectively, with 100% air content at test start.

### 9.4.3.3 Frequency (of Oscillation) Analysis

Typical examples for the oscillation frequencies recorded in the bracing of the vent pipe and at the dummy quencher during the GKM II-M tests are shown in Figures 9-150 and 9-151 for Test No. 13 (1/6 MSL break).

In addition to the power spectral densities (PSD's) of the strains recorded in the individual braces (top graph in Figure 9-150), the cross power spectral densities (CPSD's) for measuring points SG 6.1/SG 6.2 were determined in magnitude and phase (middle graphs in Figure 9-150). For two measurement signals to be correlated, the CPSD is calculated according to the equation indicated in Figure 9-55 (see Subsection 9.4.2.1.1). Besides the phase position, the magnitudes obtained are each a measure for the degree of correlation in comparison with the two individual power densities. That comparison is represented in the form of the coherence function (bottom graph in Figure 9-150). Here, coherences  $> 0.5$  are to be designated as significant.

Both the PSD's of the strains at the individual braces and also the CPSD exhibit power-density maxima at the same frequencies: 11, 17, 31, 36, 56 and 63 Hz with clear emphasis of the frequency components at 17, 31 and (36) Hz.

The dominance of the loading on the dummy quencher in the vertical direction, as described in Subsection 9.4.3.1.4, becomes especially clear in the power spectra. As an example, Figure 9-151 shows the PSD's and the CPSD of the measuring points SG 6.7 (bending strain in the vertical direction) and SG 6.8 (bending strain in the horizontal direction). For the strain in the vertical direction there is one significant power-density maximum at 105 Hz. The frequency components of the horizontal bending strain are negligible.

### 9.4.4 Summary

The following conclusions can be drawn from the experimental investigations of the pressure suppression system in a conservatively simulated single cell of the Susquehanna SES, the observed phenomena and the quantitative determination of the structural loads produced by them. The first four conclusions follow from the mean value for the entire transient calculated for each of the tests (see Subsection 9.4.2.1.2.3) and plotted in Figures 9-100 to 9-107.

- The pressure amplitudes during chugging are slightly dependent on the break size which determines the steam mass flow transient.
- The initial pool temperature has no influence or only a slight influence on the magnitude of the pressure amplitudes.

PROPRIETARY

- In the range of suppression chamber back-pressures of relevance to the plant, there is also no significant influence on the pressure amplitudes.
- The maximum mean values of the dynamic pressures in the pool, measured in the dominant frequency range from 0.5 to 13 Hz, are +0.62 bar and -0.41 bar (wall pressures). These maximum values are compared with absolute maximum values of +1.91 bar and -1.24 bar.
- The measured loads on the pool boundaries and pool internals (vent-pipe bracing, dummy quencher and I-beam) are not directly applicable to the plant and still require further evaluation.

In conclusion, the measurement results provide an adequate data base in which to evaluate the conservatism of the DFFR C.O. and chugging load specification (see Subsection 4.2.2).

9.5 DATA ANALYSIS AND LOAD SPECIFICATION

9.5.1 Introduction

As described in Subsection 9.1, the GKM II-M test program was initiated to resolve the NRC's concerns with the DFFR LOCA load specification developed from the original 4T tests. The GKM II-M test facility, instrumentation, test parameters and matrix are described in Subsection 9.1, 9.2 and 9.3. The test results presented in Subsection 9.4 indicate that the tests covered the range of expected plant parameters and provides an adequate data base for verifying the conservatism of the DFFR specification.

This section provides an analysis of the GKM-II-M data and the specification of a new LOCA steam condensation load for comparison with our existing DFFR condensation oscillation and chugging load specification. Subsection 9.5.2 gives a detailed description of the various mechanisms involved that determine the character of the pressure time histories at the pool boundary, as well as a frequency evaluation of the pressure loads measured in the pool.

Subsection 9.5.3 gives an explanation of the SSES LOCA load specification that will be used to verify the conservatism of the original DFFR load. The load specification consists of the following key elements:

- Similar to the generic Mark II program, the load is specified by the methodology contained in Reference 65. This consists of generation of volume sources and application of these sources to an acoustic model representing the SSES suppression pool. The sources are developed from selected GKM II-M data.
- For the impulsive type chugging, the sources represent mean value chugs. Four (4) time segments are selected as representative of the mean value chugs. (see Subsection 9.5.3.1)
- For the condensation oscillation (CO) like pressure oscillations, one (1) time segment is selected as representative of the bound of the GKM II-M CO data base. (see Subsection 9.5.3.1).
- The above time segments are sourced using the IWEGS model of the GKM II-M test tank (see Subsection 9.5.3.3).
- As the selected impulsive type chugging represent mean value events, they cannot be transposed unaltered to the SSES acoustic model. Such a direct transposition would lead to a high probability of exceedance. To account for this, each chug source is increased by an

PROPRIETARY

amplitude factor whose magnitude is based on a statistical analysis and a required exceedance criteria. (see Subsection 9.5.3.2)

- Since the selected CO time segment bounds the CO observed in the plateau region of the RCL break tests, and beginning of the MSL tests, no amplitude factor is required.
- Application of the SSES LOCA load specification and the sources to the SSES multivalent geometry to calculate pressure time histories for both the symmetric and asymmetric load case. In addition, the time scales for the pressure time histories are contracted and expanded to compensate for the variation in the pressure oscillation frequencies observed during the GKM II-M Tests. (see Subsection 9.5.3.4)
- Verification of the SSES LOCA load specification through comparison with the available multivalent test data from JAERI. This involves using an acoustic model of the JAERI facility and the SSES LOCA load specification to calculate JAERI wall loads for comparison with the available JAERI data. (see Subsection 9.5.3.5)

## 9.5.2 Data Analysis

### 9.5.2.1 Dynamic Pressures in the Pool and Their Physical Interpretation

In this subsection, a more detailed explanation of the physical processes that occur when steam is introduced into the water is given. The origin of the pressure events or pulsations is the rather violent condensation of the steam whenever it comes into contact with subcooled water. As a result of the underpressure that is produced, a number of mechanical degrees of freedom of the system are excited. They are classified as follows:

- Motion of the water into and back out of the vent pipe.
- Acoustic oscillation of the steam column in the vent pipe (vent acoustics).
- Acoustic oscillation of the water in the pool (pool acoustics).
- Oscillation of the tank (structural vibration).

In addition, there are also other steam condensation phenomena which can only be explained by additional events.

PROPRIETARY

- Pinch-off and collapse of a bubble underneath the vent pipe, outside against the vent pipe or inside the vent pipe.
- Pulsation of a bubble connected to the vent pipe.

Each of these events contributes to the pressure time histories at the containment boundary in a more or less pronounced manner, depending on the system conditions at the time (i.e., steam flow, pool and steam air content, pool temperature, etc.). For the majority of the data recorded at GKM II-M, the vent and pool acoustic models are the principle mechanisms contributing to the observed pressure time histories. This is especially true for the steam condensation or chugs associated with a low pool and steam air content. These chugs produce an acoustic wave which travels up the vent pipe and through the pool causing the vent and pool to ring at their natural frequencies. The pressure oscillations measured at the pool boundaries are then a composite of the vent and pool ringouts and other related oscillations associated with the steam bubbles.

The vent acoustic frequency of approximately 9 Hz observed at GKM II-M can be calculated by using an effective vent pipe length of 13.5 m and a speed of sound of 483 m/sec in the steam. Figures 9-152 to 9-154 are typical examples of pressure time histories from Test X1 (shakedown tests for the 1/6 MSL break), which display this frequency in the vent whenever water is situated inside of it. The first harmonic of this vent acoustic frequency can be seen in Figure 9-154.

Figures 9-152 to 9-154 also exhibit the pool acoustic frequencies. These frequencies can be derived from the traces for time intervals in which the water is situated in the vent. The oscillation frequencies increase with time (16.4 and 32.2 Hz) due to the increasing sonic velocity associated with the decreasing pool air content.

Figure 9-155 gives an overview of a typical blowdown. This figure plots all the frequencies for Test X1 vs. time. The frequencies were determined by reading off the oscillation periods from pressure gage P6.4. The good agreement observed between the evaluation results and the calculated frequencies in the model ("bubble oscillations", "pool acoustics", "vent acoustics") supports the physical description of the events presented above. The frequencies of the pool acoustics in the model (solid line in Figure 9-155) is calculated according to Figure 9-156, assuming the air content illustrated in Figure 9-157.

For condensation oscillation, the pressure traces exhibit regular pressure oscillations without a clear association to the vent and pool acoustics. This phenomena is observed primarily at high mass flow densities and for pool air contents of more than 1%.

PROPRIETARY

Figure 9-158 shows typical condensation oscillations during the plateau region of Test No. 33.

9.5.2.2 Evaluation of the Chugging Frequency at GKM II-M

Figures 9-159, 9-160 and 9-161 summarize the typical chugging frequencies (i.e., the frequency which corresponds to the time interval between two chugging events) for the full, 1/3 and 1/6 MS� breaks, respectively.

For the full MS� breaks (see Figure 9-159) the chug frequency is approximately  $1.7 \pm 0.2$  Hz (Test No. 4) or  $1.4 \pm 0.2$  Hz (Test No. 10) at test start, drops monotonically to about 0.6 Hz at 50 sec and then remains constant until test end. The lower chugging frequency in Test No. 10 (warm pool) compared to Test No. 4 (cold pool) is explained by the poorer heat transfer at the end of the vent pipe in Test No. 10 than in Test No. 4, due to the lower pool subcooling. The bubble at the end of the vent pipe must then be larger and therefore has a longer period due to the larger hydrodynamic coupled mass of water.

For the 1/3 MS� breaks (see Figure 9-160), the chugging frequency follows a similar pattern as the full MS� breaks, except that the monotonically decreasing chugging frequency begins at 50 sec with 0.8 Hz, reaches 0.6 Hz at 80 sec and from thereafter remains constant for 100 sec until the end of the test.

The 1/6 MS� breaks exhibit the same chugging frequency of 0.6 Hz for almost the entire duration of the test, except for a slight rise at test end (see Figure 9-161).

These three figures indicate that a chugging frequency of 0.6 Hz prevails for mass flow densities below approximately  $40 \text{ kg/m}^2 \text{ sec}$  (see Figure 9-15). Conversely, above  $40 \text{ Kg/m}^2 \text{ sec}$ , the chugging frequency is approximately proportional to the mass flow density.

9.5.2.3 Evaluation of the Pressure Oscillation Frequencies  
-----in the Pool-----

Figures 9-162, 9-163, 9-164 and 9-165 contain the dominant pressure oscillation frequencies for the RCL, full, 1/3 and 1/6 MS� break tests, respectively. Figure 9-166 shows how these frequencies were determined from the period between oscillations for the high and low bandpass filtered traces (see Subsection 9.4.2.1.2). Frequencies were read-off for both large amplitude oscillations as well as small amplitude oscillations extending over several oscillations.

An evaluation of these figures indicates that the trends found previously in Test X1 (see Figure 9-155) are quantitatively reproduced, in principle, for all the tests. The vent acoustic frequency of about 9 Hz is readily seen in all the MS� tests,

starting at 60 sec for the full and 1/3 MSL breaks and 100 sec for the 1/6 MSL breaks.

### 9.5.3. SSES LOCA Load Specification

The previous subsections give a thorough review of the GKM II-M test results and evaluation of these results. This data originates from the GKM II-M single vent facility, but can be applied to the SSES multi-vent suppression pool, if the following conditions are met:

- The single vent system represents the so-called single cell of the SSES plant, and
- the same initial conditions exist at the single vent system as at each vent of the multi-vent facility.

As described in Subsections 9.1, 9.2 and 9.3, the test facility, parameters and matrix were designed to ensure that the above conditions were met. In addition, Subsection 9.4 showed that the measured GKM II-M steam fluxes for the RCL and full MSL transients very closely simulated the FSAR calculated blowdowns, thus guaranteeing prototypical test conditions and results throughout the transients. The 1/3 and 1/6 MSL breaks also provided transients of sufficient duration to quantify the high amplitude chugs associated with high mass fluxes and low steam and pool air contents. These tests resulted in a total data base of approximately 3000 chugs of which over 800 chugs exceeded 0.5 bars. Thus, the GKM II-M data provides a very prototypical and conservative basis for specifying a SSES load definition.

With this in mind, the problem now is how to develop and specify a sufficiently conservative yet realistic LOCA load definition from the GKM II-M data base. To do this we make use of the fact that multi-vent pressures will be distinctly smaller than the pressures measured at GKM II-M. This conclusion follows from the highly random nature of the condensation events. This effect has been observed and verified numerous times in a number of multi-vent test programs (see Reference 66). This randomness of events was also observed at GKM II-M, where the measured pressure amplitudes of events occurring at close time intervals can be very different, even though the overall test conditions at those times, such as drywell pressure, steam flux, air content in the pool and steam, and mean pool temperature are practically identical (see Figure 9-81 to 9-84).

The stochastic nature of chugging stems from the fact that the actual initiating event is the spontaneous condensation of steam at the steam/water interface. The violence of the condensation and, related to it, the thermodynamic and mechanical occurrences in the time sequence are sensitively influenced by the instantaneous size and shape of the bubble surface, the temperature distribution and turbulence in the pool. All

PROPRIETARY

experience indicates that such conditions cannot be the same at every vent pipe of the SSES suppression pool during a postulated LOCA.

The second assumption is that the loads are further reduced by the desynchronized nature of chugging. Again, numerous multi-vent tests indicate that chugs do not occur simultaneously or in-phase at each vent pipe, but rather the chugs at different vents occur within a prescribed time window.

In view of these factors, the load specification assumes that the chugs occurring simultaneously at different vent pipes of SSES have different intensities and follow the same distribution of chug amplitudes in time as in the GKM II-M single-vent facility. This means that the total pool bottom load at SSES would be an average of the different chugs at each vent and the deviation from this mean value follows a probabilistic distribution. Thus, the random amplitude chugs at different vents can be replaced with the same mean value chug at each vent.

Therefore, as briefly described in Subsection 9.5.1, the SSES LOCA load specification for chugging is oriented toward mean value chugs. The random chugs at different vents are replaced with the same chug at each vent whose maximum pressures correspond to the mean values at GKM II-M. Four (4) GKM II-M time segments have been selected as representative mean value chugs in both amplitude and frequency. These time segments are sourced and applied with a 50 msec time window to the IWEGS/MARS acoustic model (see Subsection 9.5.3.4) to calculate pressure time histories at the containment boundary. In addition, since the deviation from the mean value at SSES follows a probabilistic distribution, the mean value sources are increased by an amplitude factor to obtain the desired exceedance probability prior to transposition to SSES. The time scales for each set of pressure time histories are also contracted and expanded in time to cover the range of frequencies observed at GKM II-M. Both a symmetric and asymmetric load case are considered.

As explained in Subsection 9.4.2.1, the SSES LOCA load specification does not distinguish between chugging and CO as have the Mark II Owners. However, CO-like pressure time histories (low frequency and constant amplitude) were observed in the plateau region of the RCL break test and in the beginning of the MSL break tests. Thus, in order to cover this type of pressure oscillation, one (1) time segment has been selected for the SSES LOCA load definition as representative of the CO-like pressure time histories. However, separate load combination acceleration response spectrum (ARS) curves for CO and chugging are not generated for design assessment. Instead, the ARS curves calculated from the four (4) chugging time segments and one (1) CO like time segment are combined to form one (1) envelopeing LOCA ARS curve at each containment node for combining with the remaining loads for design assessment (see Subsection 9.6).

## PROPRIETARY

Thus, the SSES LOCA load specification does not treat CO and chugging separately when used for load combination ARS curves, but only selects a separate CO time segment to depict the second category of time histories seen at GKM II-M.

As with the four (4) chugging time segments, the one (1) CO time segment is sourced and applied to IWECS/MARS. However, application to the suppression pool acoustic model is made without dephasing to calculate containment loads. This source is not multiplied by an amplitude factor, since the magnitude of the CO is relatively constant compared to the highly random chugging amplitudes, and the selected trace bounds the CO at GKM II-M. Again, the CO time segment will be contracted and expanded in time to compensate for any uncertainty in the frequency content of the selected trace. Only a symmetric load case is considered.

The following subsections give a detailed description of the SSES LOCA load specification. Specifically Subsections 9.5.3.1 and 9.5.3.2 explain the methodology for selecting the five (5) time segments for sourcing and the procedure for determining the amplitude factors, respectively. Subsections 9.5.3.3 and 9.5.3.4 delineate the procedure for sourcing the selected time segments and the application procedure for calculating the SSES containment loads, respectively. Finally, Subsection 9.5.3.5 provides justification for the SSES LOCA load definition and the 50 msec time window.

### 9.5.3.1. Selection of the GKM II-M Time Segments to be Sourced

As previously described, the SSES LOCA load specification selects five (5) pressure time histories for sourcing in IWECS/MARS to calculate the SSES wall loads. For chugging, four (4) time histories have been chosen as representative of the maximum mean value chugs at GKM II-M. For CO, one (1) time segment has been selected as bounding of the CO at GKM II-M. This subsection describes the selection procedure, presents the finally selected time segments and provides verification of the specified traces by comparing the PSD's of the selected traces with the PSD's of the GKM II-M data.

#### 9.5.3.1.1. Description of the Evaluation Procedure

The evaluation of the GKM II-M data for selecting the time segments to be used in the SSES LOCA load definition consists of the following steps:

- Selection of a representative pressure transducer.
- Preparation of two bandpass filtered pressure traces: one from 0.5 to 13 Hz (low-frequency band) and one from 10 to 100 Hz (high-frequency band).

## PROPRIETARY

- Determination of events, maximum amplitudes and oscillation frequencies of the events.
- For the chugging time segments, form mean values and select chug time segments near the maximum mean value curves.
- For the CO time segment, select a CO trace which bounds the CO data at GKM II-M.
- Verification of the selected traces.

Pressure transducer P6.7 (see Figure 9-5) was chosen as the representative transducer because it generally recorded pressures which bounded the remaining transducers (see Figures 9-36a to 9-54).

The bandpass filtering is intended to facilitate the reading of the pressure amplitudes and to sharpen the criteria for the selection of events. Subsection 9.4.2.1.2 gives the criteria for stipulating the above high and low frequency bands.

Subsections 9.4.2.1.2 and 9.3.2.3 provide explanation for reading the maximum amplitude per mean event interval and the pressure oscillation frequencies from the bandpassed traces, respectively. Figures 9-81 to 9-84 are examples of the maximum amplitude per mean event interval determined from typical full, 1/3, 1/6 MSL and RCL break tests. In addition, typical oscillatory frequencies of pressure events for the RCL, Full, 1/3 and 1/6 MSL break tests are shown in Figures 9-162 to 9-165.

The mean values were determined from the arithmetic averages of the maximum amplitudes within the time intervals defined in Subsection 9.4.2.1.2.1. The averaging is always based on those tests that were run with identical initial conditions (i.e., Tests 5/6, 11/12, etc.). Figures 9-85 to 9-87 present the results for the full, 1/3, 1/6 MSL and RCL break tests. Section 9.4 gives detailed results of the above statistical analysis.

### 9.5.3.1.2. Selection of the Chugging Pressure Time Histories

Based on the results of the statistical analysis of the pressure time histories (see Figures 9-85 and 9-86), representative chugs can be evaluated which are oriented toward the mean value curves of the pressure amplitudes. For determining the chug time segments for sourcing, all MSL break tests (Tests 3-20) were evaluated. When selecting events, an attempt was made to select chugs lying very close to the mean value curves in both the low-frequency and high-frequency ranges. In addition, it was made certain that most of the test duration was covered by the chugs.

Under this assumption a pre-selection of 46 time segments was made. These chugs adequately represent the results from MSL Test Nos. 3-20. However, for practical application to the SSES

PROPRIETARY

load specification, the number of pre-selected pressure time histories was too extensive and would require too much computation time. Therefore, the pre-selected chugs required further reduction.

To make this final selection, the pre-selected chugs from the same break size were grouped together (i.e., full, 1/3 and 1/6 MSL) and ordered according to increasing initial start times. Then one chug was picked out arbitrarily from every 10 sec interval and compared consecutively with its neighbors for shape of the signal, amplitude, damping and frequency. For each pair subject to comparison, the one that appeared to be covered by the other was eliminated. In doing this, it was taken into consideration that the SSES LOCA load specification also assigns an amplitude factor and a time factor to the source determined from the finally selected pressure time histories.

The result is a selection of four (4) time segments which represent the mean value chugs at GKM II-M. Figures 9-167 to 9-170 present the four (4) selected time histories and the time multipliers for each trace. As shown in these figures, two (2) traces originate from the full MSL tests, one (1) trace is from the 1/3 MSL tests and the remaining trace is from the 1/6 MSL tests. Figure 9-170a presents the PSD's of the specified chug time segments. Figures 9-171, 9-172 and 9-173 compare the pressure amplitudes of the specified time segments with the mean values from the various MSL tests. These figures show that the selected traces compare very favorably with the maximum mean value curves from the MSL tests. A time segment from the maximum pressure amplitude region of the 1/6 MSL tests (approximately 100 sec after test start, see Figure 9-173) was not chosen, since the selected time segments from the 1/3 and Full MSL tests (see Figures 9-171 and 9-172) are bounding. Thus, the finally selected chug time histories form a conservative and representative data base for sourcing in the SSES LOCA load specification.

Additional insight into the adequacy of the selected time segments is given by Figures 9-174 to 9-176. These figures show the frequency range of the contracted and expanded specified time histories in relation to the pressure oscillation frequencies determined from the GKM II-M data (see Subsection 9.5.2.3). They indicate that the selected traces cover the dominant frequencies at GKM II-M. However, since the oscillation frequencies were not determined from a PSD analysis, these figures do not provide information about the power at these dominant frequencies. Thus, to further verify the conservatism of the selected chug traces, a comparison of the PSD's of the selected traces with the PSD's of the GKM II-M data has been performed. This comparison is presented in Subsection 9.5.3.1.3.

9.5.3.1.2.1 Selection of the CO Pressure Time History

The CO observed during the plateau region of the RCL tests and the beginning of the MSL tests exhibit clear differences from the event like, high amplitude, damped chugs in the previous subsection. The CO time histories are characterized by constant amplitude, low frequency (6 to 8 Hz) sinusoidal-like pressure oscillations. Since CO does not display random amplitude, event like pressure oscillations, the concept of a mean value event multiplied by an amplitude factor to achieve the desired exceedance criteria cannot be utilized.

Thus, the evaluation procedure used in the previous subsection is not applicable for specifying the CO time segment. Instead, the CO time segment was chosen to bound all the CO data measured at GKM II-M.

Figures 9-177 a & b present the finally selected CO trace from Test No. 2 and the time expansion and contraction factors. The time factors were selected to cover the range of frequencies at GKM II-M. In addition, Figure 9-177c shows the PSD for the specified CO time segment. Figure 9-178 shows the oscillation frequencies of the contracted and expanded specified CO time segment compared with the oscillation frequencies determined from the RCL Test Nos. 1, 2 and 33. Again, this figure is not based on a PSD analysis and provides no information on the power at these dominant frequencies. Thus, to further verify the conservatism of the specified CO trace, a comparison of the PSD from the selected CO trace with the envelopeing PSD from the GKM II-M CO data has been performed. This comparison is presented in Subsection 9.5.3.1.3.

9.5.3.1.3 Verification of the Selected Time Segments

9.5.3.1.3.1 Chugging Time Segments

Subsection 9.5.3.1.2 showed that the selected chug time segments are representative of the maximum mean value curves at GKM II-M based on amplitude only (see Figures 9-171 to 9-173). However, in order to further verify the conservatism of the selected traces, it must be shown that the selected traces represent the mean value chugs at GKM II-M in both frequency and amplitude. To do this, a PSD analysis has been performed, which compares the envelope of the PSD's of the selected traces (including the time multipliers) with the envelope of the PSD's representing the chugs at GKM II-M. This comparison is shown in Figure 9-178a and indicates that the selected chugging traces bound the frequency content of the chugging events observed in the tests.

The envelopeing PSD of the selected chugging traces was obtained by first generating three PSD's for each selected time segment corresponding to the time multipliers  $\alpha = \alpha_{\min}$ ,  $\alpha = 1$  and  $\alpha_{\max}$ . The numbers inserted for  $\alpha_{\min}$  and  $\alpha_{\max}$  are the limits of the

PROPRIETARY

intervals given in Figures 9-167 through 9-170. Figures 9-178b to 9-178e illustrates these PSD's. The resulting twelve (12) PSD's were then combined to form the envelopeing curve shown in Figure 9-178f.

The PSD representing the GKM II-M tests was generated from the PSD's of selected time intervals (10-20 sec) from Test/Repeat Test Nos. 3/4, 9/10 and 11/12. The selected time intervals were chosen to bound the maximum values of the mean pressure amplitude curves. Figures 9-178 g and h show the time intervals from which PSD's were produced. The PSD's for each pair of Test/Repeat Test for each time interval were then averaged to obtain a PSD which represents the average spectral density of the events occurring in the time interval under consideration. Figures 9-178i to 9-178q present these average PSD's for the seven (7) time intervals. These PSD's were then envelopeed to form the representative PSD for the tests as shown in Figure 9-178r.

The above PSD's were normalized such that a chug is represented as having a unique time duration of  $t_{ref} = 1$  sec. This means that the original PSD's for the time segments were multiplied by a factor:

$$k = \frac{t_A}{n \cdot t_{ref}}$$

where:  $t_A$  = analyzed time segment  
 $n$  = number of chugs within the time interval.

This adjustment compensates for the "dead time" between chugs and thus ensures a valid PSD comparison.

9.5.3.1.3.2 CO Time Segment

For sourcing and application to IWECS/MARS, Subsection 9.5.3.1.2.1 selected PTH No. 14 from Test No. 2 (see Figure 9-177a&b) as representative of the CO data at GKM II-M. The criteria for the selection of PTH No. 14 was that it must be bounding in both amplitude and frequency of the CO data observed in the beginning of the MSL tests and the plateau region of the RCL tests. However, Subsection 9.5.3.1.2.1 documented the selection of PTH No. 14 based only on a comparison of the CO from the RCL tests and failed to compare the CO from the MSL tests. As a result, the following subsections present additional verification of the conservatism of PTH No. 14. This is based on a comparison of the CO amplitudes from all tests, as well as a comparison of the envelopeing PSD of PTH No. 14 with the envelopeing PSD of the CO at GKM II-M.

In addition, the CO data from Test Nos. 33 and 34 were not considered in the selection and verification of PTH No. 14 since the high initial pool temperature (130°F) for these tests is outside the bound of a realistic or credible LOCA initial suppression pool temperature at SSES. Thus, the data represents highly conservative CO and has not been included.

9.5.3.1.3.2.1 CO Evaluation

9.5.3.1.3.2.1.1 Comparison of the CO Amplitudes at GKM II-M

As previously stated, Subsection 9.5.3.1.2.1 only considered the RCL Test Nos. 1&2 in the selection of PTH No. 14, since the CO P6.7 amplitudes from the MSL tests are small compared to the CO amplitudes from the RCL tests. This is clearly shown in Figures 9-262a & b. These two figures compare typical CO traces from pressure transducer P6.7 for the Full MSL, 1/3 MSL and RCL tests. No CO were observed for the 1/6 MSL tests (mass flow density less than 30 kg/s). These figures indicate that the CO pressure amplitudes from the MSL tests are small in comparison to the CO amplitudes from the RCL tests.

Table 9-12 and Figure 9-263 provide additional proof that the CO amplitudes from the RCL tests are bounding. Figure 9-263 plots the mean pressure amplitudes for each break size vs. average steam mass flux from Table 9-12. Figure 9-263 implies a monotonic increase in the CO pressure amplitudes with steam mass flux and that the RCL break tests bound the MSL tests.

Thus, further verification of PTH No. 14 can be restricted to the RCL tests.

PROPRIETARY

Table 9-12 shows the time span in which CO was observed for each test, the average steam mass flux during CO and the mean CO pressure amplitude for each test break size.

The time spans classified as CO (see Table 9-12) were selected from the traces based on the criteria:

- o Sinusoidal pressure amplitudes, which do not vary much on the average, with amplitudes higher than 0.05 bar (peak-to-peak reading divided by two (2); pressure transducer P6.7)
- o Duration longer than two (2) sec.
- o Cleared vent pipe (level probes LP1 to LP5 and temperature transducer T5.6 not wetted).

The average steam mass flux for each break size was obtained as follows: 1.) For each test in Table 9-12, the steam mass flux at the beginning of the CO time span and the steam flux at the end of the CO time space were averaged. 2.) The average steam mass flux from step 1 for the same break size were then averaged.

The mean CO pressure amplitude for each break size was obtained as follows: 1.) For each test in Table 9-12, the sliding mean value was obtained by averaging the amplitudes of seventeen (17) successive pressure oscillations (peak-to-peak amplitudes divided by 2). This gives a mean value curve as a function time into the blowdown analogous to the mean value curves for chugging (see Figures 9-81 to 9-83). 2.) The maximum sliding mean value from step 1 for the same break size were then averaged. The mean CO amplitude for the RCL tests includes Tests 33 and 34, but the amplitude would not be much lower if only Tests 1 & 2 were considered.

Figure 9-16a provides further verification of the conservatism of PTH No. 14. This figure shows that the test transients at the end of the plateau region bound the theoretical RCL transient, thus causing the test steam mass flow density to be higher than in the plant for the same steam air content. This results in larger pressure amplitudes at GKM II-M relative to the plant since the amplitudes increase with decreasing steam air contents.

9.5.3.1.3.2.1.2 PSD Comparison

To provide further verification of PTH No. 14 a PSD analysis has been performed comparing the envelopeing PSD of PTH No. 14 with the envelopeing PSD of the CO from RCL Test Nos. 1 & 2. RCL tests 33 & 34 were not analyzed for the reason stated in Subsection 9.5.3.1.3.2.

PROPRIETARY

Figure 9-264 shows this comparison and indicates that PTH No. 14 bounds the frequency content of the CO from the RCL Tests 1 & 2 except for a small portion in the low frequency region. However, the envelopeing PSD of the four (4) selected chug time segments envelopes the CO data at this low frequency (see Figure 9-178a).

The envelopeing PSD of PTH No. 14 was obtained by first generating three (3) PSD's corresponding to the time multipliers  $\alpha = \alpha_{\min}$ ,  $\alpha = 1$  and  $\alpha = \alpha_{\max}$  (see Figure 9-265). The numbers inserted for  $\alpha_{\min}$  and  $\alpha_{\max}$  are the limits of the intervals given in Figures 9-177a & b. The resulting three (3) PSD's were then envelopeed to form the curve shown in Figure 9-264.

The envelopeing PSD of the CO from RCL Tests 1 & 2 (see Figure 9-264) were obtained as follows:

- o RCL Tests 1 & 2 were broken into two (2) sec CO time intervals using the criteria in Subsection 9.5.3.1.3.2.1.1. These time intervals are shown in Table 9-13.
- o PSD's were then generated for each of these two (2) sec CO time intervals from pressure transducer P6.7.
- o The PSD's of the first four (4) time intervals of Test 1 (8-16 sec) were then eliminated because a visual inspection indicated that they were covered by the PSD's of the last two (2) time intervals (16-20 sec). Similarly, the PSD's from the first five (5) time intervals of Test 2 (6-16 sec) were eliminated leaving only PSD's from the last three (3) time intervals (16-22 sec).
- o The remaining PSD's from each test were then envelopeed to form a PSD representing the time interval 16-20 sec for Test 1 and a PSD representing the time interval 16-22 sec for Test 2.
- o These two (2) PSD's (one from each test) were then averaged to form the mean of the PSD envelope of Test 1 and PSD envelope of Test 2.

9.5.3.2 Determination of the Amplitude Factors

As previously stated, a key assumption for the SSES LOCA load definition is that the chugs occurring simultaneously at different vents of the SSES plant have stochastically varying amplitudes which follow the same distribution as the chug amplitudes varying in time at GKM II-M. This means that the total vertical force on the basemat of the SSES containment is an average of the chugs occurring at each vent, which according to the above assumption is equivalent to the mean pressure of successive GKM II-M chugs. Thus, the random amplitude chugs at each vent can be replaced with the same mean value chug from GKM II-M at each vent. In addition, deviations from the mean pressure follow the laws of statistics.

Based on this, Subsection 9.5.3.1.2 selected four (4) chug time segments for sourcing in IWECS/MARS, that are representative of the maximum mean value curves at GKM II-M. However, since the deviations from the mean pressure at SSES follow a probabilistic distribution, using the unaltered design mean value sources in IWECS/MARS will give loads which have too high a probability of being exceeded. Thus, prior to applying the specified mean value sources to IWECS/MARS, they will be multiplied by an amplitude factor whose magnitude depends on the desired exceedance criteria. The lower the exceedance probability the higher the required amplitude factor.

The SSES LOCA load definition applies a separate amplitude factor for the symmetric and asymmetric load case. Conversely, the CO time segment requires no amplitude factor.

With this in mind, this subsection documents the methodology for calculating the symmetrical and asymmetric amplitude factors. Specifically, Subsection 9.5.3.2.1 explains the statistical analysis used to develop a qualified GKM II-M probability density distribution that forms the basis for determining the amplitude factors. Subsection 9.5.3.2.2 then applies this probability density distribution in a simple analytical model of the SSES containment with a Monte Carlo procedure to calculate the amplitude factors. Subsection 9.5.3.2.2 also quantifies the exceedance criteria chosen for the SSES LOCA load definition and the corresponding amplitude factors.

9.5.3.2.1 Generation of the GKM II-M Probability Distribution

In the next subsection, the SSES amplitude factors will be determined probabilistically based on a qualified probability density distribution of the GKM II-M pressure amplitudes. However, the comparatively small number of tests with identical initial conditions, as well as the steady change of the overall parameters during the duration of one and the same tests makes it difficult to generate a sufficiently large statistical population for a GKM II-M probability density distribution. If the time

PROPRIETARY

intervals of 5, 15 and 30 sec are used for averaging (see Figures 9-81 to 9-83), then there would be too small a number of pressure amplitudes to be able to make a credible statistical assertion about the loads.

In order to expand the statistical base, the pressure amplitudes for each test were first normalized to the sliding mean value. This was accomplished by dividing the maximum amplitude per mean event interval (see Subsection 9.4.2.1.2) by the mean value for the time interval within which the maximum amplitude occurred. Examples of this are shown in Figures 9-179 and 9-180. For each of the MSL Breaks (Test Nos. 3-20), a range was then defined around the maximum of the mean curve in which the mean values exceed 0.5 bars. The normalized pressure amplitudes with mean values greater than 0.5 bars were then grouped according to break size (i.e., full MSL, 1/3 MSL and 1/6 MSL) to form the basis for a frequency (of occurrence) distribution.

The results are illustrated in Figures 9-181 to 9-183. For the lower frequency band (0.5-13 Hz), the normalized amplitudes are nearly symmetrical around the normalized value 1. The distributions for the full MSL and 1/3 MSL breaks differ only slightly from one another, whereas the amplitudes of the 1/6 MSL breaks are visibly less scattered. The normalized amplitudes of the upper frequency range (10-100 Hz) are clearly more scattered in comparison to the lower bandpass.

Thus, a data base has been created from the test results which allows performing a probabilistic analysis for SSES to determine the required amplitude factors. The next subsection documents this analysis.

9.5.3.2.2 Calculation of a Symmetric and Asymmetric  
Amplitude Factors

To calculate the symmetric and asymmetric amplitude factors, a global symmetric load and a global asymmetric load are first defined as follows:

- (I) Symmetric Load: That spatially constant bottom pressure which yields the same total vertical force as the actual local bottom pressure distribution.

$$P_{\text{sym}}(t) = \frac{1}{\pi(r_a^2 - r_i^2)} \cdot \iint_{\text{BOTTOM}} P_{\text{SSES}}(\vec{r}, t) d^2\vec{r} \quad (1)$$

where:  $\iint_{\text{BOTTOM}} P_{\text{SSES}}(\vec{r}, t) d^2\vec{r}$  = total vertical force

$r_i$  = outside radius of pedestal

$r_a$  = inside radius of containment wall

$d^2\vec{r}$  = surface element

- (II) Asymmetric Load: That sinusoidally distributed circumferential bottom pressure, superimposed with the symmetric load, which yields the same maximum overturning moment as the actual bottom pressure distribution.

$$P_{\text{asym}}(t) = P_{\text{sym}}(t) + \frac{\cos\phi}{\pi/3(r_a^3 - r_i^3)} \left| \iint_{\text{BOTTOM}} P_{\text{SSES}}(\vec{r}, t) \vec{r} \times \vec{n}_a d^2\vec{r} \right| \quad (2)$$

where:  $\iint_{\text{BOTTOM}} P_{\text{SSES}}(\vec{r}, t) \vec{r} \times \vec{n}_a d^2\vec{r}$  = maximum overturning moment of actual pressure distribution.

- $r_i$  = outside radius of pedestal
- $r_a$  = inside radius of containment wall
- $d^2\vec{r}$  = surface element
- $\vec{n}_a$  = normal vector of pool boundary
- $\phi$  = azimuth angle

Figure 9-184 illustrates the derivation of the maximum overturning moment.

The next step is to transform the above symmetric and asymmetric definitions into analytical equations that can be used in a probabilistic analysis. To do this, the SSES suppression pool is subdivided into 87 single cells as shown in Figure 9-185. Then a sinusoidally varying bottom pressure of amplitude  $A_v$  is assumed in the  $v^{\text{th}}$  cell:

$$P_v(t) = A_v \sin \omega(t - t_v) \quad (3)$$

- where:  $A_v$  = pressure amplitude in  $v^{\text{th}}$  single cell
- $v$  = subscript of the single cell in the SSES pool
- $\omega$  = angular frequency
- $t_v$  = dephasing between single cells

Thus, for the symmetric load, the definition (I) is used to obtain:

$$P_{\text{sym}}(t) = \sum_{v=1}^{87} \lambda_v \sin \omega(t-t_v) \quad (4)$$

$$\text{with } \lambda_v = \frac{A_v \frac{1}{2} (r_{va}^2 - r_{vi}^2) (\phi_{v1} - \phi_{v2})}{\pi (r_a^2 - r_i^2)} \quad (5)$$

where:  $r_{vi}$  = inside radius of the vth cell  
 $r_{va}$  = outside radius of the vth cell  
 $\phi_{v1}, \phi_{v2}$  = angles which enclose the vth cell  
 $A_v$  = pressure amplitude for the v<sup>th</sup> cell

The asymmetric load is obtained according to definition (II):

$$P_{\text{asym}}(\phi, t) = P_{\text{sym}}(t) + \cos \phi \sqrt{[P_{\text{asym}}^{(1)}(t)]^2 + [P_{\text{asym}}^{(2)}(t)]^2} \quad (6)$$

$$\text{with } P_{\text{asym}}^{(1)}(t) = \sum_{v=1}^{87} \lambda_v^{(1)} \sin \omega(t-t_v) \quad (7)$$

$$\lambda_v^{(1)} = \frac{-A_v (r_{av}^3 - r_{iv}^3) (\cos \phi_{v2} - \cos \phi_{v1})}{\pi (r_a^3 - r_i^3)} \quad (8)$$

$$P_{\text{asym}}^{(2)}(t) = \sum_{v=1}^{87} \lambda_v^{(2)} \sin \omega(t-t_v) \quad (9)$$

$$\lambda_v^{(2)} = \frac{-A_v (r_{av}^3 - r_{iv}^3) (\sin \phi_{v2} - \sin \phi_{v1})}{\pi (r_a^3 - r_i^3)} \quad (10)$$

A further simplification can be made by setting the phases

$$t_v = 0 \text{ for all vents } v$$

and assigning the same pressure time history at each vent,  $\bar{P}(t)$ , (selected mean chugs). Thus, equation (3) becomes:

$$P_v(t) = A_v \bar{P}(t) \quad (3a)$$

Then, the symmetric load (phase = 0, identical pressure time histories) is:

$$P_{\text{sym}}(w,t) = A_{\text{sym}}(w) \bar{P}(t) \quad (11)$$

$$A_{\text{sym}} = \sum_{v=1}^{87} \lambda_v \quad (12)$$

where:  $A_{\text{sym}}$  = symmetric amplitude factor.

And the asymmetric load (phase = 0, identical pressure time histories) is:

$$P_{\text{asym}}(\phi,t) = P_{\text{sym}}(t) + A_{\text{asym}} \cos \phi \bar{P}(t) \quad (13)$$

$$A_{\text{asym}} = \sqrt{\left[ \sum_{v=1}^{87} \lambda_v^{(1)} \right]^2 + \left[ \sum_{v=1}^{87} \lambda_v^{(2)} \right]^2} \quad (14)$$

Where:  $A_{\text{asym}}$  = asymmetric amplitude factor.

The spacial profile of the loads from equations (11) and (13) are shown in Figure 9-186.

The individual amplitudes,  $\lambda_v$ , in equations (12) and (14) are then random variables and are prescribed in the form of a probability density distribution. For the SSES load definition, the key assumption in Subsection 9.5.3.2 requires this distribution to be the same as the distribution calculated in Subsection 9.5.3.2.1 (see Figures 9-181 to 9-183).

The probabilistic formulation now consists of

- viewing the factors  $A_{\text{asym}}$  and  $A_{\text{sym}}$  as functions of the exceedance probability  $w$  and
- inserting the expectation value  $E$  of  $P_{\text{sym}}$  into equation (6).

For the present analysis, it is assumed that the chug amplitudes in each single cell are synchronized (phase = 0). Thus, equation (11) becomes:

$$P_{\text{sym}}(w, t) = A_{\text{sym}}(w) \bar{P}(t) \quad (15)$$

and equation (13) becomes:

$$P_{\text{asym}}(w, t) = E(P_{\text{sym}}) + A_{\text{asym}}(w) \cos\phi \bar{P}(t) \quad (16)$$

The probability calculation will now be used to determine the amplitude factors  $A_{\text{sym}}$  and  $A_{\text{asym}}$ .

PROPRIETARY

The amplitudes  $A_v$  (amplitude associated with each single cell) represent a set of  $N=87$  random variables. Each of these random variables satisfies one and the same probability density distributions. As previously stated, this is identical to the GKM II-M distributions in Figures 9-181 to 9-183. The amplitude factors  $A_{sym}$  and  $A_{asym}$  are also random variables. They, in turn, also have probability density distributions from which the exceedance probabilities cited above are then obtained.

To calculate the  $A_{sym}$  and  $A_{asym}$  probability density distributions the Monte Carlo statistical method is used as follows:

- (1) Using the random principle (Monte Carlo procedure), pick out one cell from the SSES pool, perhaps the cell  $v$  (see Figure 9-185).
- (2) Using the random principle (Monte Carlo procedure), assign a normalized pressure amplitude  $A_v$  to that cell (i.e., from the distribution in Figure 9-181).
- (3) Repeat steps (1) and (2) for the remaining cells (87 single cells).
- (4) Using equations (12) and (14), respectively, calculate a numerical value for the quantity  $A_{sym}$  and  $A_{asym}$  and plot in a histogram.
- (5) Repeat steps (1) to (5) sufficiently often (i.e.,  $4 \times 10^6$  times for SSES).
- (6) Normalize the histogram and calculate the exceedance probability.

The results are illustrated in Figures 9-187 to 9-189. The top part of Figure 9-187 shows the frequency (of occurrence) distributions. The bottom part of Figure 9-187 shows the associated exceedance probabilities for the amplitude factor  $A_{sym}$  calculated for 1, 6 and 87 vent pipes and low bandpass data (0.5-13 Hz).

Figures 9-188 and 9-189 represent the numerical basis for the probabilistic load assessment for SSES. For a given exceedance probability, the associated amplitude factors can be read from the curves. Figures 9-188 to 9-189 were calculated using only the probability density distribution from the full MSB breaks (see Figure 9-181), since this data forms a more conservative basis for a probabilistic analysis than the 1/3 and 1/6 MSB breaks (see Figures 9-181 to 9-183).

To determine the factors,  $A_{sym}$  and  $A_{asym}$ , the SSES LOCA load specification assumes a load which is exceeded with a probability of  $10^{-5}$  per chugging event. This corresponds to an exceedance probability of  $10^{-3}$  per LOCA, based on 100 chugging events with a

PROPRIETARY

mean value larger than 0.5 bar. Thus, from Figure 9-188 and 9-189 the high frequency range gives the most conservative factors, and at  $10^{-5}$  exceedance probability the factor  $A_{sym}$  and  $A_{asym}$  are:

$$\begin{aligned} A_{sym} &= 1.3 \\ A_{asym} &= 0.4 \end{aligned}$$

The above analysis assumes that the chugs occur synchronized at each vent. However, the SSES load definition assumes desynchronized events and it must be shown that the above calculated factors for synchronized events are conservative when applied to a desynchronized load. For the desynchronized case the analysis is more complicated, since the form of the pressure time histories varies. Therefore, to simplify the analysis for calculating the desynchronized amplitude factors, it is assumed that identical events are uniformly distributed in a time window  $\Delta t = \tau$  with a probability density distribution:

$$f(t) = \begin{cases} 0 & t < -\tau/2 \\ 1/\tau & -\tau/2 \leq t \leq \tau/2 \\ 0 & t > \tau/2 \end{cases} \quad (17)$$

The probabilistic analysis for the desynchronized events remains the same as for the synchronized events, except that it holds only for the Fourier component  $\sin \omega t$ . Thus, equation (15) and (16) become:

symmetric load (phase  $\geq 0$ )

$$P_{sym}(\omega, \tau, t) = A_{sym}(\omega, t) \frac{\omega}{P} (t) \quad (18)$$

asymmetric load (phase  $\geq 0$ )

$$P_{asym}(\omega, \tau, t) = E(P_{sym}(\omega, \tau, t)) + A_{asym}(\omega, \tau) \cos \phi \frac{\omega}{P} (t) \quad (19)$$

where  $\omega$  signifies the Fourier component. Thus, when calculating the amplitude factors with desynchronized events, the Fourier components are considered by themselves. In other words, the substitution

$$A_v \longrightarrow A_v^\omega = A_v \cos \omega t_v \quad (20)$$

is made in equations (12) and (14). Thus, when using these two equations to calculate the factors with desynchronized events, the GKM II-M amplitudes are Monte Carloed for each single cell, as well as the time window,  $t_v$ , in equation (20). The factors  $A_{sym}^\omega$  and  $A_{asym}^\omega$  are then determined as a function of exceedance probability, time window and frequency.

In addition, the expectation value  $E$  (mean value) of the pressure in equation (19) can be calculated by means of a frequency dependent factor  $A_{phase}^\omega$ . This factor quantifies the reduced mean value at SSES with desynchronized events relative to the mean value at SSES with synchronized events. It can be shown that the factor  $A_{phase}^\omega$  is:

$$A_{phase}^\omega = \frac{\sin \omega \tau / 2}{\omega \tau / 2} \quad (21)$$

if one assumes the probability density of equation (17) and an infinite number of vents. The quantity  $A_{phase}^\omega$  as a function of frequency and time window is illustrated in Figure 9-190. The amplitude factors  $A_{sym}^\omega$  and  $A_{asym}^\omega$ , as obtained from the Monte Carlo calculations are found in Figures 9-191 and 9-192, respectively. Note that the time window reduces the symmetric loads, but increases the asymmetric loads.

To conclude, the above results can be used to determine whether factors calculated with synchronized events are conservative for the vent acoustics between 8 and 10 Hz. The vent acoustic is chosen, because these frequencies are most significant in terms of containment structural loading. Thus, a time window of 50 msec and 10 Hz is selected. From Figures 9-190 and 9-192

(  $\omega\tau=1$  ) :

$$\begin{aligned} \omega A_{\text{phase}} &= 0.63 \\ \omega A_{\text{sym}} &= 0.82 \\ \omega A_{\text{asym}} &= 0.23 \end{aligned}$$

The factors  $A_{\text{sym}}$  and  $A_{\text{asym}}$  relate to the synchronized events, which assumes that the mean value for successive chugs at GKM II-M are the same as the mean value for spacially varying chugs at SSES. However, the mean amplitudes at SSES for desynchronized events are distinctively lower than for synchronized events. The factor  $A_{\text{phase}}$  quantifies this reduction. Thus, for desynchronized events, the factors  $A_{\text{sym}}$  and  $A_{\text{asym}}$  must be renormalized by the factor  $A_{\text{phase}}$ . Therefore, for desynchronized events the amplitude factors are:

$$\begin{aligned} \omega A_{\text{sym}} / \omega A_{\text{phase}} &= 1.3 \\ \omega A_{\text{asym}} / \omega A_{\text{phase}} &= 0.37 \end{aligned}$$

These are bounded by the factors  $A_{\text{sym}} = 1.3$  and  $A_{\text{asym}} = 0.4$

Subsection 9.5.3.4 explains how these factors are applied to the sources in IWEGS/MARS to calculate containment boundary loads.

### 9.5.3.3 Determination of the SSES - Unique Chugging/CO Sources

Subsections 9.5.3.1.2 and 9.5.3.1.2.1 selected four (4) chug time segments and one (1) CO time segment, respectively, for the SSES LOCA load definition. This subsection describes the methodology for converting the selected traces into sources for use in the IWEGS/MARS acoustic model of the SSES suppression pool for calculating the containment boundary loads (see Subsection 9.5.3.4).

To do this, the GKM II-M pool was modeled based on the assumption that the pressure field due to the steam condensation event can be obtained from a solution to the linear acoustic wave equation for a specified source function. This acoustic model is presented in Section 4 of Reference 65. The IWEGS (Inhomogeneous Wave Equation Green Function Solution) computer code was developed to obtain the numerical results of the analytical solution.

The fundamental equation evaluated by IWEGS in right circular geometry is

$$p(\vec{x}, t) = 4\pi \rho c^2 \sum_N \frac{\Omega_N(\vec{r}_0) \Omega_N(\vec{r})}{V A_N} \int_0^{t^+} s(t_0) \frac{e^{-\lambda_N(t-t_0)}}{W_N} \sin(W_N(t-t_0)) dt \quad (1)$$

PROPRIETARY

for the flexible-wall case. This equation reduces to equation (4.17) of Reference 65 for rigid walls. The symbols for equation (1) are also defined in Reference 65.

In order to determine the source for each selected trace, the sonic speed, damping factor and fluid-structure interaction at GKM II-M must be known.

The sonic speed selection for each of the selected pressure traces is synonymous with identification of the GKM II-M acoustic ringout frequency:

$$f_o = c/4L$$

where:  $c$  = sonic speed in pool

$L$  = water depth

The acoustic frequency is estimated for each selected pressure trace (see Figures 9-167, 9-168, 9-169, 9-170 and 9-177 a&b) from the associated power spectral density (see Figures 9-170a and 9-177c). Figure 9-155 indicates that for the GKM II-M tests, the pool acoustic frequency lies roughly in the range 15-30 Hz. The variation of the pool acoustic frequency is due to variation of air content in the water which greatly affects the sonic speed as shown by Figure 9-156. Thus, that frequency which has the greatest pressure response between 15 Hz and 30 Hz was assumed to be the pool acoustic  $c/4L$ .

Care must be exercised so not to confuse the vent acoustic fundamental frequency (-9 Hz) or the first harmonic of the vent fundamental (-27 Hz) with the pool acoustic frequency. The selected sonic speeds correspond to pool acoustic frequencies in the range 15.0 to 23.6 Hz as shown below. Thus, this problem did not arise.

The sonic speeds selected are listed below

KWU PTH No.	Source No.	Sonic Speed
3	KWU 303	661 m/s
5	KWU 305	448.6 m/s
6	KWU 306	512 m/s
9	KWU 309	456.0 m/s
14	KWU 314	420.0 m/s

These speeds reflect the GKM II-M fluid-structure interaction (FSI) and SSES prototypical air content.

Damping of the GKM II-M pressure response is the result of FSI and the presence of air in the water. The ratio of the air damping contribution to the FSI contribution is greater than about 3 as shown in the Mark II Load Definition Report. Since

PROPRIETARY

the pool air content in GKM II-M was not measured, a nominal value of  $\zeta = 0.12$  was used for all traces which is consistent with Mark II values.

The treatment of fluid-structure interaction (FSI) at GKM II - M is described in Section 5 of Reference 65.

The above information may now be used to determine the sources using the method described below.

The Fourier Transform of the pressure field at a location specified by the vector  $\vec{r}$  resulting from the action of a single source at a location specified by the vector  $\vec{r}_0$  is given by (Eq. (5.43) of Reference 65)

$$p_W(\vec{r}) = H_W(\vec{r}/\vec{r}_0) S_W(\vec{r}_0) \quad (2)$$

where  $H_W(\vec{r}/\vec{r}_0) = \rho G_\omega(\vec{r}/\vec{r}_0)$  is the acoustic transfer function:

$$H_\omega(\vec{r}/\vec{r}_0) = 4\pi c^2 \rho \sum_N \psi_N(\omega, \vec{r}) \psi_N(\omega, \vec{r}_0) [(\omega_N^2 + \lambda_N^2 - \omega^2)^2 - 4\omega^2 \lambda_N^2]^{-1/2} e^{i\phi_N}$$

with

$$\phi_N = \tan^{-1} [2\omega \lambda_N (\omega_N^2 + \lambda_N^2 - \omega^2)^{-1}]$$

and  $\psi_N(\omega, r)$  are the flexible wall eigenfunctions (for a complete description of the acoustic transfer function see Section 5 of Reference 65). The above symbols are also defined in Reference 65.  $S_W(\vec{r}_0)$  in equation (2) is the Fourier Transform of the source function  $S(t/\vec{r}_0)$ . Once the tank radius, water depth, sonic speed and damping have been specified, the transfer function is completely known

If  $p_W(\vec{r})$  is known  $S_W(\vec{r}_0)$  and thus  $S(t/\vec{r}_0)$  can be determined via a complex division. Hence a source time history for each specified trace is determined by first taking the Fourier Transform of the specified pressure  $p(\vec{r}, t)$  to obtain  $p_W(\vec{r})$ . Next the GKM II-M geometry along with the proper sonic speed corresponding to the particular trace and the damping factor are specified and the  $H_W(\vec{r}/\vec{r}_0)$  is known.  $S_W(\vec{r}_0)$  is then obtained via division and the inverse Fourier Transformer effected to obtain the source function  $S(t/\vec{r}_0)$ .

Pressure transducer P6.8 was evaluated by the above methodology for each time segment to yield a set of five (5) source time histories. Figures 9-193 to 9-197 present the five (5) sources.

An indication of the accuracy of the above sourcing procedure is given by Figures 9-198 to 9-207. These figures compare the selected time segments (P6.8) with the pressure time histories calculated with the above sources in IWEGS. They also show a

PROPRIETARY

comparison of the PSD's of the selected traces (P6.8) with the PSD's of the pressure time histories determined with the sources and IWECS. As shown in these figures, the finally determined sources faithfully reproduce the selected traces and are acceptable for use in the SSES acoustic model.

The next subsection describes the procedure for calculating the containment boundary loads.

9.5.3.4 Application Procedure for Calculating the Susquehanna  
SSES Boundary Loads

The previous subsections described the selection of the GKM II-M time segments for sourcing, the methodology for calculating the amplitude factors and the procedure for determining the sources from the five (5) selected traces. Subsection 9.5.3.4.1 and 9.5.3.4.2 explain how this information is combined to calculate the SSES wall loads for the symmetric and a symmetric load cases, respectively.

9.5.3.4.1 Symmetric Load Case

Using acoustic theory, the SSES suppression pool is modeled by IWECS/MARS for flexible pool boundaries to calculate the pressure as a function of containment boundary location and time using the following equation:

$$p(\vec{r}, t) = 4\pi pc^2 \sum_N \frac{\Omega_N(\vec{r})}{W_N V_N} \sum_j \Omega_N(\vec{r}_j) \int_0^t S_j(t_0) e^{-\lambda_N(t-t_0)} \sin(W_N(t-t_0)) dt$$
 where  $\Omega_N(\vec{r})$  and  $\Omega_N(\vec{r}_j)$  are given by Eq. (4.33) and Eq. (4.34) of Reference 65. For rigid boundaries, this equation reduces to Eq. (4.32) of Reference 65. The symbols are defined in Reference 65.

A cylindrical coordinate system is used for the SSES geometry as shown in Figure 9-208.

The GKM II-M damping factors and sonic speeds (see Subsection 9.5.3.3) for each source (i.e., Source 303, 305, 306, 309 and 314) were used to calculate the pool boundary pressures, since by design the GKM II-M tank has the approximate FSI as the SSES containment.

As previously stated, the SSES LOCA load definition employs a 50 msec desynchronization time window for the four (4) chug time segments, but does not use desynchronization for the C3 Source 314.

For the desynchronized sources (Sources 303, 305, 306 and 309) the start time are determined in the same manner as the generic Mark II Program. This involves obtaining a set of source start times from an equal probability distribution over a 50 msec time window by repeated Monte Carlo selections. This is repeated for 1000 Monte Carlo trials - one trial being defined as a selection of a start time set (87 start times). The sum of the deviations

PROPRIETARY

of the start times within a given set is a measure of how coincident the start times are because, for N sources,

$$D = \sum_{i=1}^N [t_s^{(i)} - \bar{t}_s]^2$$

where D is the sum of the deviations,  $t_s^{(i)}$  the start time for the ith source, and  $\bar{t}_s$  the mean start time. For  $D = 0$  all vents are chugging synchronously. Thus, for the SSES LOCA load definition the set of chug start times with the minimum variance based on the set of 1000 Monte Carlo selections is used for calculating the containment boundary loads, since they yield the highest global pressure response.

The above information is used to calculate the containment boundary loads for the symmetric case as follows:

- (1) One of the sources is selected and its magnitude multiplied by the symmetric amplitude factor (see Subsection 9.5.3.2). This same source is then assigned to each vent exit location (87 vents) in the IWECS/MARS suppression pool model. No amplitude factor is used with the CO Source 314.
- (2) For the chug sources, the chug start times at each vent are determined as described above. For the CO source, all vents are assumed inphase.
- (3) IWECS/MARS is then used to calculate a set of pressure time histories at the containment boundary locations required by the ANSYS structural model.

This procedure is repeated for each of the five (5) sources. In addition, the time scales for each set of pressure time histories are expanded and contracted by the factors  $\alpha_{max}$  and  $\alpha_{min}$ . The values of  $\alpha_{min}$  and  $\alpha_{max}$  are the limits of the intervals in Figures 9-167, 9-168, 9-169, 9-170 and 9-177 a&b. This gives fifteen (15) sets of pressure time histories for containment analysis.

9.5.3.4.2. Asymmetric Load Case.

The procedure for calculating the asymmetric wall loads is identical as the procedure for the symmetric load case (i.e. same sonic speed, damping, governing equations, etc.), except that the asymmetric amplitude factor is applied to the sources in a different manner. In addition, the CO Source 314 is not considered for the asymmetric load case.

The asymmetric load is calculated as follows:

PROPRIETARY

- (1) One of the sources is selected and its magnitude multiplied by the asymmetric factor (see Subsection 9.5.3.2)

$$A_{\text{sym}} \cdot \cos \phi$$

depending on the azimuth location,  $\phi$  of the vent pipe at which the source will be located. These sources with varying amplitudes (cosine distribution) are then assigned to their respective vent exit in the IWEGS/MARS suppression pool model.

- (2) For the chug sources, the start times at each vent are determined as in Subsection 9.5.3.4.1.
- (3) IWEGS/MARS is then used to calculate a set of pressure time histories at the containment locations required by the ANSYS structural model.

This procedure is repeated for each of the four (4) chug sources. Again, the time scales for each set of pressure time histories are expanded and contracted by the factors  $\alpha_{\text{max}}$  and  $\alpha_{\text{min}}$ . The values of  $\alpha_{\text{min}}$  and  $\alpha_{\text{max}}$  are the limits of the intervals in Figures 9-167 to 9-170. This yields twelve (12) sets of pressure time histories for containment analysis.

9.5.3.5. Verification of the SSES LOCA Load Definition

9.5.3.5.1 JAERI Comparison

9.5.3.5.1.1 Introduction

To demonstrate the conservatism of the SSES chugging load definition and application methodology, a comparison between the SSES chugging load definition methodology and the JAERI data was performed. This involves applying the sources developed from the selected chug time segments in an acoustic model of the JAERI facility to calculate wall loads for comparison with the eight large chugs observed in JAERI Tests 0002. The procedure used for this comparison as well as the results of the comparison, are described in the following subsections.

9.5.3.5.1.2 Description of Comparison Method

This section describes the comparison methodology used for comparing the predicted pressure response using the SSES chugging load definition against the JAERI chugging data. The JAERI data used for the comparison are discussed in Subsection

9.5.3.5.1.2.1. The single vent sources used are described in Subsection 9.5.3.5.1.2.2, and the JAERI acoustic model in which these sources were applied is discussed in Subsection 9.5.3.5.1.2.3. Finally, the comparison basis is described in Subsection 9.5.3.5.1.2.4.

9.5.3.5.1.2.1 The JAERI Test Data

The data used for the data comparison are the eight largest chugs from JAERI Test 0002. These eight chugs include the four strongest chugs from the six tests selected by JAERI for spectral analysis. All eight are among the 13 largest chugs from the tests analyzed by JAERI. Figure 9-266 shows the average pool bottom RMS pressure for the various high amplitude chugs observed in the JAERI tests to date. Although the pool bottom readings are believed to be somewhat distorted by the sensor mounting arrangements, it is reasonable to assume that they provide an adequate ranking of chug strength. Based on Figure 9-266 it is seen that the eight chugs selected from Test 0002 are indeed among the largest chugs seen in the JAERI tests to date.

Due to the problem with the bottom sensor as mentioned above, the actual comparisons are made against pressure measurements at the 1800mm and 3600mm elevations in JAERI. The 3600mm elevation corresponds to that at the vent exit and the 1800mm corresponds to the elevation at mid-clearance. Pressure readings from three sensors on the wall at 1800mm (WWPF-201, 401, 501) and from six wall sensors at 3600mm (WWPF-202 to 207) were made available by JAERI. The pressure time history from the sensors at a given elevation (3600mm or 1800mm) were first spatially averaged. That is, the pressure time histories were averaged time step by time

PROPRIETARY

step at each elevation. This is appropriate for this data since the spatially averaged pressure represents the global effects of the time varying wall pressure on the containment structure. This averaging tends to preserve frequency components which are spatially in phase and reduce those which are out of phase. The components that are spatially in phase are from the pool normal mode response whereas those which are spatially out of phase are the signals that are transducer specific.

For each of the eight chugs, the spatially averaged pressure history was computed at two elevations. PSDs of the average pressure histories were computed and the maximum envelope over the eight chugs was constructed. The resulting envelope PSDs at 1800mm and 3600mm elevations were compared with the predicted pressure responses in the manner described in Subsections 9.5.3.5.1.2.4.

9.5.3.5.1.2.2. Chug Sources

The four (4) pressure time histories (see Figures 9-167 to 9-170) selected for the SSES chugging load definition were converted by Bechtel into source time histories as described in Subsection 9.5.3.3.

The sources developed for the SSES load definition are different from those developed for the Mark II Generic Program in that SSES sources are actual source time histories as opposed to a combination of triangular impulse and sinusoids used by the Mark II Generic Program. The source time history description provides a much more detailed description of the source and duplicates all the frequency content observed in the single vent pool wall pressure traces.

To verify the integration procedure used with these source time histories, each individual source was applied to the GKM II-M single vent geometry, and the resulting pressure time history and PSDs were compared against those provided by Bechtel. The Creare model was able to reproduce the Bechtel results to within 5% for the peak overpressure, within 7% for the peak underpressure, and within 11% for the total mean square power.

Since the JAERI data represents only chugging, the CO source from PTH No. 14 (see Subsection 9.5.3.1.2.1) was excluded from the comparison.

9.5.3.5.1.2.3. The JAERI Acoustic Model

The JAERI test facility is a circular tank with concrete fillers to simulate a 20° annular wedge of the Mark II pool. The acoustic model developed at Creare represents the JAERI geometry as a 20° annular wedge. A comparison between the actual JAERI geometry and the geometry used in the acoustic model is shown in Figure 9-267. The acoustic model of the JAERI facility closely

follows the acoustic model developed in the Task A.16 Generic Mark II Acoustic Methodology (see Reference 65). Briefly, the inhomogeneous wave equation is solved for the annular 20° wedge by means of the Green's function method.

A JAERI acoustic run involves applying the selected source at each of the 7 vents one at a time. The pressure histories due to the sources applied at each individual vents at each of the sensor locations are then computed. A set of start times of a particular time trial is selected from a 50msec uniform probability desynchronization window. Having obtained the start times for individual vents, the pressure time history at each sensor location is then synthesized with the appropriate start times. As described in the next subsection, a total of 160 time trials were run for each of the four chug sources which constitute the chugging load definition.

#### 9.5.3.5.1.2.4 Comparison Basis

As described in Subsection 9.5.3.5.1.2.1, the comparison is made with eight chugs from JAERI Tests 0002. To make the comparison on a statistically meaningful basis, a simulation was made in the same manner as that used for obtaining the envelope of the actual eight JAERI chugs. That is, eight time trials or "chugs" were run in the JAERI acoustic model and a PSD\* envelope of the eight trials was constructed. To make the envelope of the computed pressure time histories insensitive to the random statistics of the eight time trials selected, this procedure was repeated 20 times (i.e.,  $8 \times 20 = 160$  time trials). This results in 20 PSD envelopes (one PSD envelope for a set of eight time trials). These PSD envelopes were then averaged to obtain an average PSD envelope for a particular source. Such an average envelope was then constructed for each of the four sources.

For the four sources, the average envelopes for each source were envelopeed and this envelope is then compared against the envelope of the eight chugs in the JAERI tests. In addition, the symmetric amplitude factor (see Subsection 9.5.3.2) was not applied to the wall loads calculated by the SSES load definition for comparison with JAERI. Thus, the comparison represents mean value chugs at GKM II-M.

However, the PSD's generated by the SSES chugging load definition reflect the use of the time expansion and contraction factors (see Figures 9-167 to 9-170).

The comparison basis described above is identical to that used by the Mark II Generic Program.

---

\*The PSD's generated by the SSES sources were normalized to account for their difference in time duration when compared to the time duration of the JAERI chugs.

9.5.3.5.1.3 Results and Discussion

The results of the comparison are shown in Figures 9-268 and 9-269 at the two elevations in JAERI. As described earlier in Subsection 9.5.3.5.2.4, the envelope for the sources excludes the source for the CO period in the GKM II tests as well as the symmetric amplitude factor.

Figures 9-268 and 9-269 show the comparisons at the 1800mm and the 3600mm elevations, respectively. From these figures it is seen that the SSES load definition bounds the JAERI data by a substantial margin over the entire range from 0-100 Hz.

In conclusion, a comparison between our chugging load definition and the eight large chugs observed in JAERI Test 0002 has been presented. The comparison has been made on a basis which is statistically meaningful and shows that the current SSES chugging load definition developed from GKM II-M is very conservative.

9.5.3.5.2 Verification of the 50 msec Time Window

Verification of the 50 msec desynchronization time window will be documented in the Generic Mark II Load Definition Report scheduled for submittal in April of 1981.

9.5.3.5.3 Response to NRC Concerns Regarding the SSES Chugging Load Specification

This Subsection responds to a request from the NRC staff (Reference 81) to document arguments demonstrating the adequacy of the SSES chugging load specification. Essentially all of the information contained in this subsection was presented at a meeting held in San Jose, California on April 8, 1982 between representatives of the Mark II Owners Group, SSES personnel and members of the NRC staff.

Reference 81 specifies two elements required to address the staff's concerns:

- "1. Formally document the material which was used to conclude that the asymmetric chugging load specification is not a major contributor to the structural response. Although not specifically discussed during the meeting, the response should address the validity of the rationale over the entire frequency range of interest (0 to 50 Hz).
2. Extend the JAERI comparisons to 20 different sets of start times to be generated in the same manner as outlined in the generic methodology. For each set of start times evaluate the response of applying the chugging sources to the JAERI facility and develop an

PROPRIETARY

envelope of the minimum of the twenty trials. Comparison of that envelope to experimental data obtained from JAERI would then be provided. If frequency "poke through" exists, justification would be provided as to why the current specification is adequate."

9.5.3.5.3.1 Contribution of the Asymmetric Chugging Load Specification to Plant Structural Response

9.5.3.5.3.1.1 Comments on the Asymmetric Chugging Load Case

This section provides comments on the effect of vent start times on the asymmetric pool wall loads generated during chugging. As with symmetric loads, a unique vent start time set (STS) will produce a unique asymmetric pool response. However, analysis of the complete pool transfer function shows that the primary asymmetric pool response in terms of a net "overturning" moment is generated only by the first asymmetric mode in the frequency range between 15-100 Hz. No other asymmetric modes produce a net overturning moment.

Figure 9-271 shows a schematic of the first asymmetric mode in the SSES pool geometry. The mode shape for the pressure generated by a single vent is a cosine function, therefore, the "area of influence" for that vent is quite large. Due to the "large area of influence", considerable overlapping occurs between adjacent vents.

Further, for the first asymmetric mode, the pressure variation in the radial direction is small. This means that vents located on a given radial ray but at different radii have roughly the same effective "moment arm".

Finally, in a multivent geometry where events are randomly desynchronized (such as in the SSES case), the asymmetric mode is not stationary in space. It rotates; hence there is no fixed axis in time about which the asymmetric mode produces a full amplitude "overturning moment".

Due to these considerations, the effect of a selected STS on the "overturning moment" is much less than that predicted by simple analyses where the "area of influence" is taken to be a small area under each vent and the moment arm as the orthogonal distance between the vent and a fixed axis in time. It is expected, therefore, that in reality, the effect of vent start times on the asymmetric pool responses will be no more severe than those for the symmetric response.

9.5.3.5.3.1.2 Generic Position on WNP-2 Submittal

The Mark II utilities and their respective A/Es have reviewed Part A of the WNP-2 report (Reference 82) and compared it with

PROPRIETARY

their own containment analyses. All utilities have concluded that Mark II plants exhibit overall characteristics and trends similar to those identified in the report:

- o There is no evidence that the Mark II containments "rock" due to hydrodynamic loads.
- o In a concrete containment, the plant response to chugging loads decreases as one moves away from the wetwell in the primary containment. Once outside the primary containment, the response is significantly reduced.

When reviewing separate responses for the symmetric and asymmetric chugging load, very little difference is observed. This result has been confirmed on the WNP-2 plant with a subsequent submittal to the NRC. (Reference 83).

As an additional example of the structural response, this time for the SSES concrete containment, selected acceleration response spectra (ARS) curves generated with our chugging load definition are presented in Figure 9-273 through 9-280. Each figure compares the ARS curves for the symmetric and asymmetric load cases at the node points in the ANSYS model identified in Figure 9-272. For most containment locations, the symmetric and asymmetric ARS curves are quite similar in both frequency content and amplitude. Also, observe the decrease in amplitude of the responses at increasing elevation above the containment basemat. The curves represent the envelope of all design sources.

However, in some containment locations, at certain frequencies, the symmetric ARS curves exceed the asymmetric ARS curves, and vice versa, by more than 10%. Our explanation is as follows:

- o Figures 9-273 to 9-276: These figures show the responses in the vertical direction at elevations above the diaphragm slab. These figures indicate that the symmetric response always exceeds the asymmetric, and at some frequencies by more than 10%. This is expected, since the symmetric source distribution was specified to maximize the vertical pressures on the containment basemat. These pressures would excite the vertical modes of the containment in a more significant manner, than the asymmetric case. This is especially true in the low frequencies, where desynchronization does not significantly effect the pressure response, and the symmetric source distribution leads to a greater source strength than the asymmetric load case. This greater source strength in low frequencies, also excites the higher frequencies as explained in the JAERI PRS comparison (Subsection 9.5.3.5.3.2.3.2).

PROPRIETARY

- o Figure 9-277: Please note that the ARS curves for Node 841, direction X, presented at the April 8, 1982 NRC/SSSES meeting and documented in PLA-1063 were labeled incorrectly. The curves should be reversed, such that the asymmetric ARS curve now exceeds the symmetric curve in the low frequencies. Figure 9-277 shows the correct labeling of the curves.

At all frequencies, except between 4 and 8 Hz, the two load cases compare quite well. As a result, we requested that Bechtel examine the natural frequencies and participation factors for Node 841. They indicated that in these low frequencies, there are significant modes in the horizontal direction. Thus, one would expect the asymmetric response to exceed the symmetric response for Node 841 at these frequencies, since desynchronization does not significantly effect the pressure distribution at these low frequencies and the asymmetric source distribution was specified to maximize the asymmetry in the containment.

- o Figure 9-278: This figure exhibits a similar comparison as Figure 9-277. Again, at these low frequencies, Node 411 contains significant lateral modes. Thus, as for Figure 9-277, one would expect the asymmetric response to exceed the symmetric response.
- o Figure 9-279: This figure indicates that above 30 Hz the symmetric response exceeds the asymmetric response by a large margin. At this containment azimuth location, we determined that the Mean Square Power (MSP) for the pressure at the intersection of the containment wall and basemat, varies for the symmetric and asymmetric load case. Our analysis indicated that the symmetric MSP exceeds the asymmetric MSP at this azimuth location; probably due to the effects of the chug start times for downcomers in close proximity to this azimuth angle. Because of this, one would expect the symmetric case to exceed the asymmetric case.
- o Figure 9-280: For all frequencies, the symmetric and asymmetric load cases exhibit a similar response.

Thus, even with the source strength unbalance imposed by the asymmetric chugging load definition, the structural response is not noticeably different from that of the symmetric load case.

It can be concluded from the preceding discussion that the overturning moment associated with asymmetric chugging need not be used as a criterion in assessing the adequacy of the load definition. This is true for the reasons outlined in Subsection 9.5.3.5.3.1.1 and because the asymmetric pressure distribution can also be found in the symmetric load specification due to

PROPRIETARY

source desynchronization. Thus, the adequacy of the SSES chugging load definition can be demonstrated through a comparison of the symmetric load specification with the multivent JAERI data.

9.5.3.5.3.2 Comparison of Minimum Variance Trials Using the  
-----SSES/GKM II-M Sources with the JAERI Data-----

9.5.3.5.3.2.1 Introduction

The SSES Chugging Loads Methodology specifies the use of the start time set (STS) that has the minimum variance in 1000 STSs drawn randomly from a 50 msec desynchronization time window. This minimum variance STS is then used for the application of all the SSES/GKM II-M Chugging Sources.

A given set of start times produces a unique pressure time history at the pool wall boundary, with a signal attenuation (referred to as frequency holes) occurring at some frequencies and amplification at others, due to the vent-to-vent phasing implied by the selected set of start times. A concern was therefore raised that the use of a single STS in evaluating the SSES chugging loads might result in non-conservatism in frequencies where signal attenuation or "frequency holes" occurred.

Although it is true that "frequency holes" will be produced with any one set of start times, the overall conservatism in the strengths of the SSES/GKM II-M Sources will still produce a conservative response of the SSES containment over the entire frequency range used in the plant structural evaluation. To demonstrate this, the SSES Chugging Loads calculation procedure was applied in the JAERI geometry and the results were compared against the bounding JAERI data. The following describes the comparison and presents the results obtained. The results confirm the conservatism in the SSES Chugging Load Definition.

9.5.3.5.3.2.2 Comparison Procedure

First, one thousand STSs were drawn randomly from the 50 msec desynchronization time window. Note that each STS consists of seven start times--one for each of the seven vents in the JAERI geometry. The STS having the minimum variance was then identified. This procedure was repeated 20 times and 20 such minimum variances STSs were obtained.

Using each minimum variance STS, the SSES/GKM II-M chug sources were applied one at a time in an acoustic model of the JAERI test facility. Spatially averaged pressure time histories (one for each source) were then generated at the 1.8 meter and 3.6 meter elevations. The power spectral densities (PSD) were then obtained for these pressure time histories. From these, PSD envelopes over the SSES/GKM II-M sources were constructed at the

PROPRIETARY

1.8 meter and 3.6 meter elevations. Similarly, PRS envelopes were obtained at the 1.8 meter elevation. This procedure was performed using each of the 20 minimum variance STSs. Thus, at each of the two elevations, 20 PSD envelopes resulted--one for each of the 20 minimum variance STSs, and 20 PRS envelopes were obtained at the 1.8 meter elevation.

Finally, minimum PSD envelopes for the 20 minimum variance STS were constructed at the 1.8 meter and 3.6 meter elevations; a minimum PRS envelope was constructed at the 1.8 meter elevation. These minimum PSD and PRS envelopes were then compared with the corresponding maximum envelopes of the eight largest chugs for JAERI test 0002. Note that the PRSs for the JAERI data were obtained by digitizing the JAERI pressure time histories to produce the respective PRSs. The comparison and conclusions are presented in the next section.

Before proceeding to discuss results, several important points require further clarification. First, the SSES/GKM II-M Sources used in the JAERI acoustic model to calculate the JAERI pool wall pressure time histories used the same sonic speed as that given in the SSES Chugging load definition report. That is, the sonic speeds derived for the GKM II-M test facility were used with each of the SSES/GKM II-M sources. The sonic speeds for the SSES/GKM II-M ranges between 661m/sec and 449 m/sec.

The sonic speeds in flexible wall facilities are related to the equivalent rigid wall sonic speeds by the following relation:

$$C = C_0 (1 + \rho C_0^2 \delta)^{-\frac{1}{2}}$$

where  $\rho$  is the water density,  $C$  is the flexible wall sonic speed,  $C_0$  is the rigid wall sonic speed and  $\delta$  is volume distensibility\*. Figure 9-281 shows the relationships between the rigid wall sonic speeds and flexible wall sonic speeds for GKM II-M and JAERI facilities.

Ideally, the GKM II-M "rigid wall" sonic speeds would be obtained first by using the above relation. The rigid wall sonic speeds would then be corrected to obtain the equivalent flexible wall sonic speeds for JAERI. These corrected sonic speeds would then be used with the corresponding sources in the JAERI acoustic model for predicting the JAERI wall pressures. However, this procedure was not used because the differences between the GKM II-M flexible wall sonic speeds and the corresponding JAERI flexible wall sonic speeds is less than 7% over the range of

$$* \delta = 139.90 \times 10^{-12} \text{ m/n}^2 \text{ for GKM II-M facility.}$$

$$\delta = 497.38 \times 10^{-12} \text{ m/n}^2 \text{ for JAERI facility.}$$

sonic speeds (661 m/sec to 449 m/sec) for the SSES/GKM II-M sources.\*\* This small difference did not warrant the added computational complexity and hence the GKM II-M sonic speeds were used in the JAERI wall pressure computations.

The second point that needs to be clarified is with respect to the damping values used in the calculation of the PRSS. The PRSS were calculated using 4% and 7% damping. These are the damping values described in USAEC Reg. Guide 1.61 for reinforced concrete containments.

The final point is regarding the amplitude factors used with the sources. The SSES chugging loads methodology calls for multiplying the SSES/GKM II-M sources by an amplitude factor to achieve an exceedance probability of  $10^{-5}$ . For the 87 vent SSES containment geometry, an amplitude factor of 1.3 is derived.

Since the objective of the comparisons presented here is to compare the results of applying the SSES chugging loads methodology in JAERI with the actual JAERI data, one must compute the amplitude factor appropriate for the seven vent JAERI geometry. The amplitude factor for the JAERI seven vent geometry is 1.95 to obtain an exceedance probability of  $10^{-5}$  used for the SSES plant evaluations. The comparisons presented in the next subsection are made using the amplitude factor of 1.3 corresponding to that used for the SSES chugging loads evaluations, as well as the amplitude factor of 1.95 which is the correct one for application of the SSES chugging loads methodology in the JAERI facility.

#### 9.5.3.5.3.2.3 - Results and Discussion

As described in the previous subsection, two types of comparisons were performed--one on a PSD basis and one on a PRS basis. The PSD comparisons are presented in Subsection 9.5.3.5.3.2.3.1 followed by the PRS comparisons in Subsection 9.5.3.5.3.2.3.2.

##### 9.5.3.5.3.2.3.1. PSD Comparisons

Figure 9-282 shows the comparison of the minimum envelope of 20 minimum variance STSS with the JAERI data at the 1.8 meter elevation. The amplitude factor used here was that for the SSES containment and equal to 1.3. From this figure it is seen that the minimum envelope of the 20 minimum variance STSS bounds the JAERI data by a substantial margin at frequencies below about 40 Hz. Above 40 Hz, the signal levels are quite small and so from this linear plot it is difficult to make many comparisons.

---

\*\*This is because most of the "flexibility" comes from the air in the pool rather than from the structural flexibility.

PROPRIETARY

Therefore, the same data plotted on log scale are shown in Figure 9-283. From this figure it is seen that the minimum envelope drops below the maximum JAERI data envelope by a small amount in the frequency range between 40 and 80 Hz.

Figure 9-284 shows the comparison of the minimum envelope of 20 minimum variance STSS with the maximum JAERI data envelope at the 3.6 meter elevation. From this linear plot, it is again seen that the minimum envelope of the 20 minimum variance STSS bounds the JAERI data envelope by substantial margins, and both the JAERI data envelope as well as the 20 minimum variance STSS envelope drop to very low levels beyond 30 Hz. Figure 9-285 shows the same data plotted on a log scale, and it is seen that in the frequency range between 40 and 60 Hz, the JAERI data envelope "pokes through" the minimum envelope by small amounts.

As mentioned earlier in Subsection 9.5.3.5.3.2.2, the appropriate amplitude factor for the seven vent JAERI geometry is 1.95. Comparisons are now made using the 1.95 amplitude factor. Figure 9-286 shows the comparison of the minimum envelope of 20 minimum variance STSS with the maximum JAERI data envelope at the 1.8 meter elevation. It is seen that with this amplitude factor of 1.95, the minimum variance envelope bounds the JAERI data by substantial margins everywhere except for some small "poke throughs" in the frequency range between 45 and 80 Hz. Figure 9-287 shows a similar comparison at the 3.6 meter elevation and at this elevation, the minimum envelope of the 20 minimum variance STSS bounds the JAERI data at all frequencies.

From the comparisons presented above, the following conclusions can be drawn:

1. Using an amplitude factor of 1.3 (the SSES value), the minimum envelope of 20 minimum variance trials bounds the maximum envelope of JAERI data except for small "poke throughs" between approximately 40 and 80 Hz.
2. Using an amplitude factor of 1.95, which is the correct factor for the seven vent JAERI geometry, the minimum envelope of the 20 minimum variance trials bounds the maximum envelope of JAERI data everywhere at the 3.6 meter elevation and there are very small "poke throughs" between 40 and 80 Hz at the 1.8 meter elevation.

9.5.3.5.3.2.3.2 Pressure Response Spectra Comparisons

Comparisons on PRS basis are more appropriate than PSD comparisons in evaluating the effect of a given pressure time history on a multi-modal structure such as the SSES containment. This is because the response of the multi-modal structure at a given modal frequency is the sum of the resonant response to forcing function amplitude at the modal resonant frequency plus

PROPRIETARY

the static or forced response due to forcing function amplitudes at other frequencies. A PSD only shows the component of the forcing function at a given frequency and therefore, does not provide insight into the static or forced response of the structure. A PRS on the other hand takes into account both the resonant and the static or forced response and hence provides a more accurate picture of the response of a multi-modal system.

The comparison of the minimum PRS envelope for the 20 minimum variance STSS with the maximum PRS envelope of the JAERI data at the 1.8 meter elevation is shown in Figure 9-288. For the PRSS shown in this figure, the SSES amplitude factor of 1.3 was used with a damping value 4%. It is clear from this figure that the minimum envelope of the 20 minimum variance STSS bounds the maximum PRS envelope of the JAERI data throughout the frequency range between 0-100 Hz. Figure 9-289 shows the PRS comparisons for an amplitude of 1.95, and a 4% damping. Again this figure shows that the minimum envelope of the 20 minimum variance trials bounds the maximum JAERI data envelope by significant margins across the entire frequency range.

Finally, Figures 9-290 and 9-291 show the PRS envelope comparisons for the 7% damping case with amplitude factors of 1.3 and 1.95, respectively. From these figures, it is again seen that the minimum PRS envelope of the 20 minimum variance STSS bounds the maximum JAERI data PRS envelope by a substantial margin throughout the frequency range.

From the comparisons presented above, it can be concluded that due to the large conservatisms in the strength of the SSES/GKM II-M Sources, the response produced by the minimum variance STSS will produce conservative plant responses in spite of the "frequency holes" created by a particular STS selection. Therefore, the SSES/GKM II-M chugging loads methodology is adequate

9.6 VERIFICATION OF THE DESIGN SPECIFICATION

This section provides information verifying the conservatism of the DFFR steam condensation load definition (see Subsection 4.2.2) and the MK II single vent lateral load definition (see Reference 47).

9.6.1 Evaluation of the DFFR CO and Chugging Load Specification

Currently, all SSES plant design assessment for LOCA steam condensation loads employ the DFFR CO and chugging load specification developed from the original 4T test program (see Appendix A of Reference 21 and Reference 16).

However, the NRC in NUREG 0487 expressed concern about the conservatism of the DFFR specification because of the non-prototypical vent length used in the 4T test facility. As a result, PP&L initiated the GKM II-M test program to resolve the NRC's concerns. Subsection 9.4 documents the results of the GKM II-M tests and Subsection 9.5 presents the SSES LOCA load definition resulting from the GKM II-M data base.

In this subsection, a comparison of the DFFR LOCA load and the SSES LOCA load definition is provided. This evaluation is accomplished by comparing the DFFR containment acceleration response spectra (ARS) curves with the containment ARS curves generated by the SSES specification. This comparison study is made for LOCA (DFFR) vs. LOCA (KWU), as well as the combination LOCA (DFFR) + SSE + SRV vs. LOCA (KWU) + SSE + SRV. Subsection 9.6.1.1 presents the results of the two comparison cases. Subsection 9.6.1.2 provides an evaluation the ARS comparison. Finally, Subsection 9.6.1.3 summarizes the LOCA loads comparison.

9.6.1.1 Containment Acceleration Response Spectra Comparison

9.6.1.1.1 LOCA (DFFR) vs. LOCA (KWU) Acceleration Response Spectra Comparison

Figures 9-209 through 9-218 compare the containment horizontal ARS curves due to the DFFR LOCA load definition (LOCA (DFFR)) with the containment horizontal ARS curves generated by the SSES LOCA load definition (LOCA (KWU)) for 2% spectral damping. Figures 9-219 through 9-227 compare the vertical LOCA (DFFR) ARS curves with the vertical LOCA (KWU) ARS curves for 2% spectral damping.

The LOCA (DFFR) curves represent envelopeing spectra and were generated as follows:

- o The DFFR LOCA load consisting of chugging and CO (see Appendix A of Reference 21 and Reference 16), each of which contain three (3) frequencies, were inputed to the 3-D ANSYS structural model (see Figure B-1) to calculate ARS curves at the required node points. Both an asymmetric and symmetric

PROPRIETARY

load case were considered for chugging, while only a symmetric load case was considered for CO.

- o These individual LOCA (DFFR) ARS curves were then envelopeed into one (1) ARS curve at each nodal point. This was done for both horizontal and vertical responses.
- o The ARS curves for nodal points at approximately the same elevation were then further envelopeed to give one (1) ARS curve for each required elevation. Table 9-14 gives the nodal points envelopeed at each elevation for the LOCA (DFFR) spectra and 3-D ANSYS model. Additionally, the peak frequencies of the spectra were broadened by 15% to account for any uncertainties in the modeling techniques and material properties.

Similarly, the LOCA (KWU) curves represent envelopeing spectra and were obtained as follows:

- o The SSES LOCA load definition was used to calculate fifteen (15) sets of symmetric wall loads and twelve (12) sets of asymmetric wall loads (see Subsections 9.5.3.4.1 and 9.5.3.4.2, respectively) for input to the ANSYS model. The ANSYS model then generated ARS curves at the required nodes for each set of pressure time histories.
- o These individual LOCA (KWU) ARS curves were then envelopeed into one (1) ARS curve at each nodal point. This was done for both horizontal and vertical responses.
- o The ARS curves for nodal points at approximately the same elevation were then envelopeed to form a representative curve for each elevation. Table 9-14 gives the nodal points envelopeed at each elevation for the LOCA (KWU) curves and 3-D ANSYS model. The LOCA (KWU) curves were then broadened by 15% at the peak frequencies.

9.6.1.1.2 SSE + SRV (ADS) + LOCA (DFFR) vs. SSE + SRV (ADS) + LOCA (KWU)  
----- Acceleration Response Spectra Comparison -----

Figure 9-228 through 9-237 compare the containment horizontal ARS curves for the combination SSE + SRV (ADS) + LOCA (DFFR) with the containment horizontal ARS curves for the combination SSE + SRV (ADS) + LOCA (KWU) for 2% spectral damping. Figures 9-238 through 9-246 compare the vertical containment ARS curves for the same combination with 2% spectral damping. These combination curves were obtained by combining the individual spectra by the absolute sum method (SSE + SRV + LOCA).

The LOCA (DFFR) and LOCA (KWU) spectra combined with the remaining spectra were generated as described in Subsection 9.6.1.1.1.

PROPRIETARY

The SRV ARS curves combined with the other spectra were obtained as follows:

- o The three original KWU traces (see Subsection 4.1.3.5) were contracted and expanded in time to give five different traces between 55% and 110% of the frequency of the original trace. This gives fifteen sets of pressure time histories for input to the 3-D ANSYS model.
- o The ADS load case is considered for combination with LOCA and SSE. However, the azimuth distribution on the containment boundary as discussed in Subsection 4.1.3 indicates that the all valve case governs the ADS case for symmetric loading. Therefore, for the combination SSE + SRV + LOCA, the all valve load case (see Subsection 4.1.3.1) was used to calculate the SRV spectra.
- o The 3-D ANSYS model then produced fifteen sets of spectra at the required nodal points. This was done for the horizontal and vertical spectra.
- o The fifteen spectra were then envelopeed to give one spectra for each node and then further envelopeed with the spectra for nodes at approximately the same elevation. This yielded one ARS curve for each elevation. Table 9-14 indicates the node points envelopeed at each elevation for the 3-D ANSYS model and SRV loading. The envelopeed spectra were then broadened by 15% at the peak frequencies.
- o The SRV spectra combined with the SSE and LOCA (DFFR) spectra reflect the use of a 1.5 peak pressure multiplier (see 4.1.3.5) applied to the SRV pressure time histories. However, for this comparison, the SRV spectra combined with the LOCA (KWU) and SSE spectra reflect the use of a 1.1 peak pressure multiplier. This is consistent with the NRC's acceptance of a peak pressure multiplier of 1.1 for all actuations documented in NUREG 0487-Supplement No. 1. Again it must be emphasized that the 1.1 multiplier is for comparison only and that all SSES design assessment for SRV loads use the 1.5 peak pressure multiplier.

The SSE ARS curves combined with the other spectra were obtained using the 2-D seismic stick model (see SSES FSAR Figures 3.7b-7 and 3.7b-8). The modal properties of the stick models are found in SSES FSAR Table 3.7b-5 and Figures 3.7b-14 through 3.7b-19. SSES FSAR Section 3.7b gives a detailed description of the methodology for determining the ARS curves due to SSE. Again, for the present comparison, the spectra for different nodes at approximately the same elevation were envelopeed to obtain one spectra for each elevation. Table 9-14 gives the node points envelopeed at each elevation for the SSE and 2-D stick model.

9.6.1.2 Containment Response Spectra Evaluation

A comparison of the containment acceleration response spectra (ARS) generated by the SSES LOCA load specification and the DFFR chugging and condensation oscillation load specifications shows the following:

- (1) The SSES LOCA load specification generally result in responses greater than the DFFR LOCA load specification in two frequency ranges
  - o 10 to 20 Hz
  - o above 40 Hz
- (2) From 20 Hz to 40 Hz the DFFR generally bounds the SSES LOCA load specification response.

To provide a more meaningful evaluation, we have also produced containment ARS curves for the load combination which is generally design controlling:

SSE + SRV (ADS) + LOCA

As described in Subsections 9.6.1.1.1 and 9.6.1.1.2 these response spectra curves utilize either the DFFR LOCA loads or the SSES LOCA load specification as the input LOCA load for generation of these combined response spectra curves. As also indicated in Subsection 9.6.1.1.2, the SRV load specification used for combination with the new SSES LOCA response spectra utilizes a 1.1 amplitude multiplier. The SRV loads used in combination with the DFFR LOCA response spectra utilize a 1.5 amplitude multiplier.

An evaluation of these response spectra curves shows the following:

- (1) The combined response spectra which includes the SSES LOCA loads generally result in responses greater than the DFFR combined response spectra for frequencies greater than 40 Hz.
- (2) For horizontal responses below 40 Hz the DFFR combined response spectra generally bounds the SSES combined response spectra.
- (3) For vertical responses below 40 Hz, the SSES combined response spectra generally exceed the DFFR combined response spectra.

These evaluations indicate that in order to verify our design basis additional work will be required. Two general approaches can be utilized:

- (1) Reduce the input load
- (2) Re-assess the affected components to determine whether sufficient design margin exists.

We will discuss our plans for pursuing both options.

9.6.1.2.1 Load Reduction Assessment

The degree of conservatism that exists in the SSES LOCA load definition can be easily seen in the comparison of this load specification and the available JAERI multivalent test data given in Subsection 9.5.3.5.1. As indicated in Subsection 9.5.3.5.1, the SSES LOCA load definition without load amplitude factors (mean value load) bounds the available JAERI data by factors of 2 to 10. This indicates that substantial room for load reduction exists. The following subsections give the areas of load reduction we will be pursuing.

9.6.1.2.1.1 Reduction of Load Amplitude Factors

As described in Subsection 9.5.3.2.2, symmetric and asymmetric amplitude factors were generated for application to the selected chugging pressure time histories in our LOCA load specification. The selection of these amplitude factors was based on a probability calculation. An exceedance probability of  $10^{-5}$  per chugging event was selected. If one assumed the probability of a LOCA occurring as  $10^{-6}$ , then the combined probability of having a LOCA and exceeding the specified load definition is  $10^{-11}$ . We believe a high degree of conservatism will still be retained in the load definition if a reasonable reduction in the specified exceedance probability is taken. As can be seen in Figures 9-190 & 9-191, the following amplitude factors result with the indicated change in exceedance probability:

Exceedance Probability ( $w \tau = \bar{w}$ )	Symmetric Amplitude Factor	Asymmetric Amplitude Factor
$10^{-5}$	1.3	.37
$10^{-4}$	1.27	.35
$10^{-3}$	1.23	.31
$10^{-2}$	1.17	.25

9.6.1.2.1.2 Re-Selection of Pressure Time Histories

As described in Subsection 9.5.3.1.2, the selected chugging pressure time histories were to be selected as representative of the mean value events. The selection basis was an evaluation of peak over pressure and observed oscillation frequency. As a check of the selected pressure time histories, a Power Spectral Density (PSD) evaluation was performed. This evaluation is described in Subsection 9.5.3.1.3.1. Figure 9-178a shows the

PROPRIETARY

final PSD comparison. As can be seen the selected mean value events substantially bound the mean value PSD for Tests 3/4, 9/10, 11/12, 13/14 and 19/20. This indicates that the selected chugging events are actually representative of events substantially above the mean. If this proves to be true, the application of amplitude factors would not be appropriate for these selected pressure time histories. A re-selection of new mean value events based on power will be performed.

9.6.1.2.1.3. Adoption of Mark II Owners Group Load Methodology

Another option for potential load reduction would be use of the load methodology developed by GE for the Mk II Owners Group. This methodology uses a different selection bases for design chugs. These design chugs are the average of the seven largest chugs observed in the 4TCO data with their largest neighbor chug. This methodology could be used with the GKM IIM data base to develop an alternate load definition.

9.6.1.2.1.4. Development of a New Chugging Load Methodology

As a further option, the basis for a new chugging load methodology exists. This new methodology would consist of the development of a series of design sources from GKM IIM tests which represent bounding blowdown conditions. These sources would be developed from the actual chugs which occur during the selected time segments for each test. These sources would then be applied randomly to an acoustic model of the Susquehanna suppression pool. In addition random source start times would be employed. This load definition would give the most realistic overall load input for plant assessment.

9.6.1.2.2. Plant Re-Assessment

As a result of the comparison documented in Subsection 9.6.1 and Bechtel's opinion that a re-assessment of SSES based on the GKM II-M load definition would not significantly impact our projected fuel load date, PP&L on April 1, 1981 decided to terminate the assessment of SSES based on the DFFR chugging and CO specification and re-evaluate SSES based on the GKM II-M load specification.

Section 7.0 provides the results of this re-assessment.

9.6.1.3. Summary

The new SSES LOCA load definition results in containment responses which exceed, in many frequencies, the responses obtained from the DFFR chugging and condensation oscillation load.

PROPRIETARY

We are presently reviewing the degree of conservatism which exists in the SSES LOCA load. There are several areas where load reduction could be obtained. In addition, several other options exist for general load reduction.

On April 1, 1981, PP&L apted to terminate the re-evaluation of SSES with the DFFR load definition, and instead performed a re-evaluation of the plant based on the GKM II-M load specification.

9.6.2 Verification of the Mk II Single Vent Dynamic  
Lateral Load Specification

The SSES downcomer bracing system has been analyzed using the dynamic multi-vent lateral load specification transmitted under Task A.13. This specification applies the Mark II single vent dynamic lateral load specification (see Reference 47) in conjunction with a multi-vent multiplier whose magnitude depends on the number of vents analyzed and the desired exceedance probability. The single vent load specification was developed by Pretech Inc. using the original 4T data base. However, the NRC has expressed concern about the conservatism of the single vent load definition. We therefore measured lateral loads during the GKM IIM test and committed to compare those measurements with the load specification.

As a result, the following subsections compare the maximum resultant bracing force measured at GKM II-M with the maximum resultant bracing force at GKM II-M predicted by the Mk II load definition. Specifically, Subsection 9.6.2.1 describes the methodology for applying the Mk II load to theoretically determine the maximum resultant bracing force. Subsection 9.6.2.2 presents the measured bracing force data and the maximum resultant bracing force for each break size measured at GKM II-M. Finally, Subsection 9.6.2.3 compares the theoretically determined bracing force with the measured bracing force at GKM II-M.

9.6.2.1 Theoretical Determination of the Bracing Force at  
GKM II-M

9.6.2.1.1 Finite Element Model

Figure 9-247 is a schematic view of the finite element model. The downcomer, inner tank, and outer tank were modeled using beam type elements. The individual views of these components are shown in Figure 9-248.

The fluid elements are shown in Figure 9-249. There were 13 layers of fluid elements in the model. The solid elements used to represent the fluid had mid-side nodes which also matched up in elevation with the beam nodes of the structural model. A 90° degree sector of the fluid was used, instead of the complete 360 degree volume, in order to reduce the cost of the runs. Appropriate structural properties were used to represent the 90 degree sector model.

The brace, which is the component of primary interest in the structure, was modeled as a scalar spring element. The stiff bracing connections between the downcomer and outer tank, and

PROPRIETARY

between the inner and outer tank were modeled as "RBAR" rigid type elements within NASTRAN.

9.6.2.1.2- Model Assumptions

There were a number of important considerations that went into the development of the finite element model that was used in this analysis. They are:

- (a) The downcomer is a long cylinder and at some distance beyond the bracing level, the local effects of the bracing support die out. This allows for a variable spacing of nodal points along the downcomer, with a larger spacing away from the brace level.
- (b) The outer tank is a tall cantilevered beam. The downcomer is attached by very stiff bracing to the outer tank at its top. The inner tank is supported at two levels on the outer tank. It was deemed essential to include the outer tank in the model, as the interaction between the downcomer and the outer tank could dramatically affect the system response.
- (c) Beam type elements were used to model the tanks and downcomer. This was deemed to be a conservative assumption in regard to magnitude of the bracing force. The local shell effects at the bracing connection points are essentially precluded by stiffening rings.

The General Electric Report (Reference 47), which developed the load function used herein, used similar assumptions in developing a beam type element model of the 4T test facility.

- (d) The brace can be represented as a scalar spring type element. This spring is attached between the downcomer and outer tank. The stiffer the spring the higher the expected reaction developed in the spring. The bracing stiffness used was 1400 K/in which represents the actual stiffness in the GKM II-M facility.
- (e) The load under consideration is applied directly to the downcomer at its tip. The exact location and distribution of the load on the downcomer is not known and therefore using a beam type element for the downcomer, instead of shell type elements is further justified.
- (f) The fact that the load is applied directly to the downcomer, and is not directly applied to the fluid means that the fluid effect can be handled with explicit fluid finite elements that condense into an added mass.

PROPRIETARY

The formulation used here corresponds to the equations shown in Appendix A of Reference 69. This theory is explained in more detail later.

9.6.2.1.3 Fluid Representation

The fluid is accounted for as defined in References 68 and 69. The fluid is defined as an acoustic medium which satisfies the equation:

$$\nabla^2 P = \ddot{P}/C^2$$

The combined structure plus fluid equations have the form:

$$\begin{bmatrix} M & O \\ -\int \hat{A}^T & Q \end{bmatrix} \begin{Bmatrix} \ddot{U} \\ \ddot{P} \end{Bmatrix} + \begin{bmatrix} K & \hat{A} \\ O & \bar{H} \end{bmatrix} \begin{Bmatrix} U \\ P \end{Bmatrix} = \begin{Bmatrix} f \\ o \end{Bmatrix}$$

This set of simultaneous equations can be solved by NASTRAN when some special procedures are invoked. For the incompressible fluid formulation, which was used in this model, the equations simplify to:

$$(M + \int \hat{A} \bar{H}^{-1} \hat{A}^T) \ddot{U} + KU = f$$

In this new equation the fluid effect has been reduced to an added mass term. Although the procedure is similar to an added lumped mass for the fluid, the theory and numerical values for the mass differ considerably from the simple lumped mass procedure.

9.6.2.1.4 Structural Model

In defining the beam type elements that make up the structural model, care was taken to ensure a refined subdivision for the structure. Thus the downcomer was divided into 34 elements along its length. This permits accurate determination of the higher modes of the system. Due to the nature of the loading to be investigated, namely the very short period of the load, the higher modes could possibly have a significant effect on the

PROPRIETARY

response. A refined subdivision was also maintained on the inner and outer tanks. Shear effects were included in the analysis by specifying shear coefficients for the beam type elements used to model the downcomer, and inner and outer tanks.

9.6.2.1.5 Loading

The loading applied to the model was the Mk II Load. This load is defined as 2 possible cases.

1. A maximum amplitude of 30,000 pounds with a duration of 3 msec.
2. A maximum amplitude of 10,000 pounds with a duration of 6 msec.

The loading is in the shape of a half-sine wave. Plots of the two loadings are shown in Figures 4-62G&H. These loadings were derived in Reference 47 as producing an upper bound on measured response of the downcomer.

Because of the fact that a 90 degree sector or one fourth of the structure was used in the model, one fourth of the total load was applied.

9.6.2.1.6 Analysis Results

The maximum resultant bracing force developed in the bracing of the GKM II-M test facility, under application of the Mk II single vent lateral load definition (see Reference 47), is 22776 pounds. The impulse with a maximum amplitude of 30,000 pounds and a duration of 3 msec gave the largest bracing force.

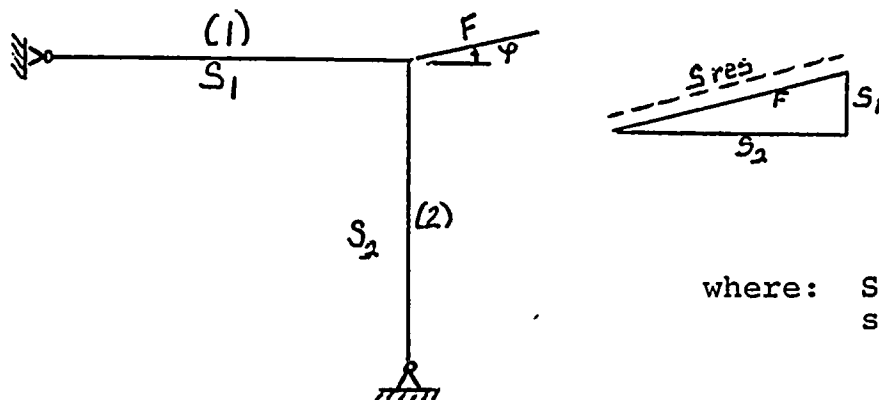
9.6.2.2 Bracing Force Data at GKM II-M

9.6.2.2.1 Measurement of the Bracing Forces

Subsection 9.4.3.1.1 describes the instrumentation installed on the vent pipe bracing (see Figure 9-5 and 9-6), the equation for converting the measured strains into bracing forces and the procedure for determining the resultant bracing forces.

9.6.2.2.2 Resultant Bracing Forces

The resultant bracing force was determined as described in Subsection 9.4.3.1.1 and is the equilibrium maintaining force which acts on the vent pipe horizontally at the height of the bracing assemblage.



where:  $S_1$  and  $S_2$  are the strut forces.

The resultant bracing forces as a function of steam mass flux and time into the blowdown for each MSL test are shown in Figures 9-250 to 9-258.

The resultant bracing forces for each test break size were then classified into the frequency distributions illustrated in Figures 9-259 to 9-261. This data is characterized by the following table:

	Maximum value kN	Mean Value kN
Full MSL Breaks	70.8	17
1/3 MSL Breaks	86.1	21
1/6 MSL Breaks	88.7	21.5

Thus, the maximum resultant bracing force measured at GKM II-M is 88.7 KN.

9.6.2.3 Comparison of the Theoretical and Measured Maximum Resultant Bracing Force

According to Subsection 9.6.2.1.6 the maximum resultant bracing force using the Mk II load definition is 22776 pounds or 101.3

PROPRIETARY

kN. The maximum resultant bracing force measured at GKM II-M is 88.7 kN.

Therefore, the Mk II load definition (see Reference 47) conservatively predicts the maximum measured resultant bracing force at GKM II-M.

9.6.3 Statistical Evaluation of the GKM II-M Resultant Bracing  
Force Data

9.6.3.1 Introduction

DAR Subsection 9.6.2 compares the maximum calculated resultant bracing force at GKM II-M, using the Mark II single vent lateral load, with the maximum measured resultant bracing force at GKM II-M. This comparison reveals that the theoretical value bounds the measured value and indicates the conservatism of the Mark II single vent lateral load. However, the NRC performed a re-evaluation of the Mark II lateral tip load based on a statistical analysis of the original 4T bracing force data. They now conclude that the Mark II impulse should be extrapolated to 65 Kips while preserving the 3 msec impulse duration. This corresponds to a lateral load which will be exceeded once in  $10^5$  bracing force events or once in ten LOCAs, if one assumes 100 chuqs at 100 vents per LOCA.

To provide additional confirmation of the conservatism of using an extrapolated Mark II lateral load at  $10^{-5}$  exceedance probability, a statistical analysis of the GKM II-M bracing force data has been performed. This gave a relation for determining the resultant bracing force as a function of the exceedance probability. From this relation, the GKM II-M resultant bracing force required for a  $10^{-5}$  exceedance probability was then determined. The lateral load impulse which predicts this bracing force at GKM II-M was then determined and compared to the revised Mark II tip impulse. The following subsections document this effort.

9.6.3.2 Derivation of a Probability Density Function from the  
Measured Resultant Bracing Forces from the 1/6 MSL Tests

The mean and maximum resultant bracing force values for the 1/6 MSL tests envelope the mean and maximum values for the full and 1/3 MSL tests. Thus, to maximize the statistically determined resultant bracing force, the present statistical analysis is restricted to only the 1/6 MSL bracing force data.

9.6.3.2.1 General Consideration

To derive an expression for the probability density function, we assume the function follows an exponential decay. Thus, the

PROPRIETARY

following probability density function is selected for the 1/6 MSL resultant bracing force data:

$$f(u) = u \cdot e^{-u} \quad (1)$$

where:  $u = C \cdot x$   
 $C =$  constant to be determined  
 $x =$  resultant bracing force, kN.

Integrating Eq. (1) and evaluating the interval yields:

$$\int_0^{\infty} f(u) du = \int_0^{\infty} u \cdot e^{-u} du = e^{-u} du = e^{-u} (-u-1) \Big|_0^{\infty} = 1$$

Thus, this function satisfies the basic condition imposed on the probability density function; namely, that the total probability = 1.

To determine the constant, C, the mean value of the distribution,  $u$ , is defined as the first-order moment of the probability density function described by Eq. (1). Thus

$$\bar{u} = \int_0^{\infty} u^2 \cdot e^{-u} \cdot du = e^{-u} (-u^2 - 2u - 2) \Big|_0^{\infty} = 2$$

This is used to determine the constant, C, as:

$$C = \frac{2}{\bar{x}}$$

and  $u$  from Eq. (1) as:

$$u = \frac{2}{\bar{x}} \cdot x \quad (2)$$

where:  $\bar{x}$  is the mean value of the 1/6 MSL resultant bracing force data.

PROPRIETARY

The exceedance probability based on the probability density function of Eq. (1) is:

$$F'(u) = \int_0^{\infty} f(u) du = (1+u)e^{-u} \quad (3)$$

The probability that the resultant lies in the interval  $a \leq x \leq b$  is:

$$F(a \leq u \leq b) = (a+1)e^{-a} - (b+1)e^{-b} \quad (4)$$

9.6.3.2.2. Application to the 1/6 MSL Tests

The range of mass fluxes to be used in evaluating the resulting bracing forces from Tests 13 to 18 is:

$$11 \leq \frac{\dot{m}}{A} \leq 33 \quad (\text{kg/m}^2\text{s})$$

Tests 19 and 20 were omitted since they are bounded by the remaining 1/6 MSL tests.

Table 9B shows the frequency distribution for Tests 13 to 18. The numbers in parenthesis designate the number of occurrences per test.

TABLE 9B

Bracing Forces kN	Number of Events
0 - 10	36 (6)
10 - 20	212 (35.3)
20 - 30	237 (39.5)
30 - 40	110 (18.3)
40 - 50	52 (8.6)
50 - 60	25 (4.16)
60 - 70	6 (1)
70 - 80	1 (1/6)
80 - 90	1 (1/6)

Listed in Table 9B are a total of 680 events, or 111.3 events per test.

PROPRIETARY

The mean value of the frequency distribution is:

$$\bar{x} = 25.6 \text{ kN}$$

Thus, Eq. (2) becomes

$$u = \frac{2 \cdot x}{25.6} = 0.078 \cdot x \quad (5)$$

Now Eq. (4) and (5) can be used to determine the interval probability. A comparison of the theoretically determined interval probability (Eq. 4 and Eq. 5) with the relative frequencies obtained from Table 9B (test data) is shown in Table 9C.

TABLE 9C

Bracing Forces kN	Relative Frequency (Test Data)	Interval Probability
0 - 10	0.053	0.184
10 - 20	0.31	0.2784
20 - 30	0.35	0.216
30 - 40	0.16	0.14
40 - 50	0.026	0.0826
50 - 60	0.037	0.0465
60 - 70	$8.8 \times 10^{-3}$	0.025
70 - 80	$1.5 \times 10^{-3}$	0.013
80 - 90	$1.5 \times 10^{-3}$	$6.8 \times 10^{-3}$

Figure 9-270 compares the theoretical with the measured relative frequencies. Thus, the function  $f(u) = ue^{-u}$  predicts a conservative distribution.

From Eq. (3) the exceedance probability is:

$$F'(u) = (1 + u) e^{-u} \quad (6)$$

with  $u = 0.078 \cdot x$

Thus, the bracing force  $x$  which is exceeded with a probability  $F'$  can be determined.

From Eq. (6) with an exceedance probability of  $10^{-5}$  the resultant bracing force  $x$  is:

$$182 \text{ kN} = 40.9 \text{ Kips}$$

9.6.3.3. Determination of the Extrapolated Mark II Impulse

To determine the Mark II impulse required to produce a bracing force of 182 kN at GKM II-M, we assume that the bracing force is

PROPRIETARY

linearly proportional to the impulse. This yields the following relation:

$$\frac{I_m}{F_m} = \frac{I_1}{F_1} \quad (7)$$

where:  $I_m$  = impulse of present Mark II single vent lateral load definition

$F_m$  = bracing force at GKM II-M produced by  $I_m$

$I_1$  = impulse required to produce bracing force at GKM II-M corresponding to a  $10^{-5}$  exceedance probability

$F_1$  = statistical determined bracing force at GKM II-M for a  $10^{-5}$  exceedance probability.

Subsection 9.6.2.1.6 calculates a maximum bracing force of 22.8 Kips with lateral load of 30,000 lbs and 3 msec impulse duration. Thus,  $F_m = 22.8$  Kips and the Mark II impulse,  $I_m$ , is the area under the half sine wave impulse curve calculated with the following relation:

$$I_m = 2 F t_D / \pi \quad (8)$$

where:  $F$  = amplitude of Mark II impulse  
 $t_D$  = time duration of Mark II impulse

Substituting  $F = 30,000$  lbs. and  $t_D = 3$  msec gives:

$$\begin{aligned} I_m &= (2) (30,000) (.003) / \\ I_m &= 57.3 \text{ #-sec} \end{aligned}$$

Substituting  $F_1 = 182 \text{ kN} = 40.9$  Kips,  $I_m = 57.3$  #-sec and  $F_m = 22.8$  Kips into Eq. (7) gives:

$$\frac{57.3}{22.8} = \frac{I_1}{40.9}$$

$$I_1 = 102.8 \text{ #-sec}$$

To determine the extrapolated Mark II force required to give an impulse of 102.8 #-sec, we assume the impulse duration of 3 msec remains the same and solve for  $F$  in Eq. (8). Thus, for  $I_1 = 102.8$  #-sec

$$F = \frac{(102.8) (\pi)}{(2) (.003)}$$

PROPRIETARY

$$F = 54.8 \text{ Kips}$$

Thus, an extrapolated half-sine wave impulse of 54 Kips with a 3 msec time duration produces a bracing force in GKM II-M corresponding to an exceedance probability of  $10^{-5}$ . This compares to the Mark II impulse magnitude of 65 Kips.

For SSES, the Mark II impulse of 65 Kips with a 3 msec time duration, as required by the NRC, will be used for a single vent lateral load definition (see Subsection 4.2.2.3).